Analysis and Design of Visco-Elastic Cushions for Delicate Objects

by

Marie Claire Rice Sasmal

A dissertation submitted in partial fulfillment
of the requirements for the degree of
Doctor of Philosophy
(Mechanical Engineering)
in The University of Michigan
2020

Doctoral Committee:

Professor Ellen Arruda, Co-Chair
Professor Michael Thouless, Co-Chair
Professor Steven Broglio
Professor Gregory Hulbert

Marie C. Rice Sasmal

mcrice@umich.edu

ORCID iD: 0000-0002-6157-8004

ACKNOWLEDGEMENTS

This research was generously supported by the University of Michigan Department of Mechanical Engineering, the Head Health Challenge III, the Army Research Laboratory, Ford Motor Company, and Axalta Coating Systems.

I would like to express my deepest appreciation to my advisors, Prof. Ellen Arruda and Prof. Michael Thouless, for their guidance and expertise throughout these recent years. I wish to thank them for taking me on as a student, and for their support and patience though the process of writing this thesis. I would like to acknowledge my committee members, Prof. Gregory Hulbert and Prof. Steven Broglio for providing valuable advice and feedback. The support I have received from Andrea Poli has been instrumental to all my efforts in the laboratory, and I would also like to thank Prof. Philip Bayly, Dr. James Gorman, Levon Cimonian, and Dr. Lena Mohr for providing me with computational codes related to this work.

I wish to convey my thanks to all my colleagues, especially Dr. Callan Luetkemeyer, Dr. James Gorman, Isha Gupta, Dr. Dandan Wang, Prof. Jonathan Estrada, Ryan Rosario, Isabel Newton, Dr. Benjamin Marchi, and Dr. Lena Mohr. Further, I would like to thank Dr. Audrey Sedal, Alison Hake, Dr. Rachel Vitali, Dr. Ashley Bielinski, Dr. William LePage, and Dr. Michael Quann for their friendship and support.

I am lucky to have such a wonderful family, and I'd like to thank my parents, Steve and Leslie, and my brother, John, for believing in me and encouraging me. Finally, I would like to express my sincere gratitude to my husband, Ari, for his unwavering love and support.

TABLE OF CONTENTS

CHAPTER

LIST OF FIGURES

Figure

LIST OF TABLES

Table

ABSTRACT

Efficient protective structures are needed to ensure safe transport of fragile devices, cushioning of delicate objects in mechanically hazardous environments, like spacecraft launch, and protection of humans during collisions in athletics and automotive accidents. Compliant delicate objects, that are enclosed in rigid shells, are protected from indentation, but are vulnerable to impacts that involve large accelerations and high coefficients of restitution. The human brain is an example of such a delicate object. Early theories of traumatic brain injury identified two kinematic injury regimes, which are separated by a characteristic time. Depending on the duration of the impact, either a maximum tolerable acceleration or velocity governs risk, and common cushioning strategies that rely solely on reducing force may be inadequate for impacts that are shorter than the object's natural period.

First, we introduce a dissipative cushioning strategy that uses the fractional derivative visco-elastic model known as the fractional Standard Linear Solid (FSLS). The FSLS is capable of describing the complex modulus of a variety of materials accurately with a smaller number of parameters than a multi-term Prony series. Material selection criteria and a framework for optimizing cushions for minimum size are also presented. The cushions that dissipate most efficiently have relaxation times which are slightly shorter than the impact, and have high loss factors. The acceleration of the impact can be reduced more efficiently with a visco-elastic cushion than a purely elastic collision. The successful implementation of this cushioning strategy requires knowledge of the characteristic time of the object and threshold values for its maximum tolerable velocity and acceleration.

Therefore, the calculation of the characteristic time and approximate kinematic tolerances for the brain, obtained by analyzing an idealized two-dimensional cylindrical model,

are sought in the second part of this thesis. Both rotation and linear translation of the cylinder's shell are evaluated, and the resulting pressure and shear strain are calculated. This approach is based on the theory that dangerous strain arises from rotational motion, and that dangerous levels of pressure come from linear motion. The rotation of the skull primarily produces shear stress and strain. Linear motion would produce both shear stress and strain, but the high bulk modulus of the brain suppresses volumetric strain and the low shear modulus suppresses high shear stress. The strain from linear motion is found to be relatively small.

The final chapters, which consider the strain due to rotation, provide scaling laws for estimating shear strain from rotational loads. In particular, shear strain is either dependent on angular velocity or the angular velocity times a fractional power of the impact duration, when the impact is short. The points of transition between different types of response are identified as the characteristic times of the brain, and their dependence on material properties and dimensions of the brain are discussed. Knowing which types of motion bring about more or less deformation is important for knowing which aspects of the impact should be mitigated. This can be paired with the analysis of the cushion response, addressed initially, to design cushions that meet design criteria based on the kinematic damage criteria. Therefore, the correlations between strain and kinematics can be coupled with the cushion design framework to optimize the design of helmets and evaluate their performance with simple experiments that measure easily-observable kinematic quantities rather than internal strain.

CHAPTER I

Introduction

Delicate objects may require protective packaging to mitigate the risk of damage from accidental impacts that occur during transportation of the object, or its use. Impact mitigation can be achieved using more than one strategy, and the design of effective cushions for specific scenarios depends on the accurate characterization of the response of the delicate objects involved to the types of impact they experience. Increasing awareness of concussion and other mild brain injuries has made concussion prevention an especially high-priority packaging application. In this scenario, visco-elastic packaging may offer an alternative to the existing designs that are currently available to athletes in contact sports, which are primarily elastic in their behavior. In this chapter, the foundations of impact protection for dynamic delicate structures will be introduced, with special attention paid to efforts to describe and mitigate mild injuries to the human brain caused by low-energy collisions. Subsequent chapters will offer a novel impact mitigation strategy suitable for delicate objects involved in collisions, and discussions of the extent of deformation that occurs in impacts of various kinds.

1.1 Differentiating between short and long impacts using a lumped parameter model

Essential early work on impact-induced damage, by Kornhauser and Lawton [23], used a simple linear lumped parameter system as a model for more complicated delicate objects that are subjected to external dynamic loads. The system they used is shown in Figure 1.1, and is composed of an excitation point and a mass, which are connected to each other by a linear spring. The excitation point represent the exterior container surrounding the delicate object. In the context of head injury, the excitation point is an analog for the skull, and its motion represents skull motion. The deformation within the spring functions as an analog for strain within the delicate object. When the excitation point is accelerated, deformation builds up within the spring in proportion with the force in the spring, and the spring applies this force to the mass. Then the mass accelerates, which in turn changes the deformation in the spring. The internal dynamics of the delicate object have a characteristic time, T_c, which is associated with a period of natural vibration. The object's stiffness and mass govern the characteristic time of the delicate object, through its frequency of natural vibration.

The response of this system has two limits: the short-pulse limit and the long-pulse limit. Examples of these types of response are shown in Figure 1.2a. "Short" and "long" refer to the relative duration of the impact, t_0, compared to the characteristic time of the delicate object, T_c. Depending on the ratio of these two times, the response of the system will tend to approach either the short-pulse limit or the long-pulse limit. That is, whenever the acceleration pulse that results from an impact is much longer than the characteristic time of the delicate object, the response of the delicate object will share some important features. When the features of the long-pulse limit are exhibited by the system after being loaded with an acceleration pulse of finite duration, it can be said to be displaying the "long-pulse response." Similarly, if the duration of the impact is much shorter than the

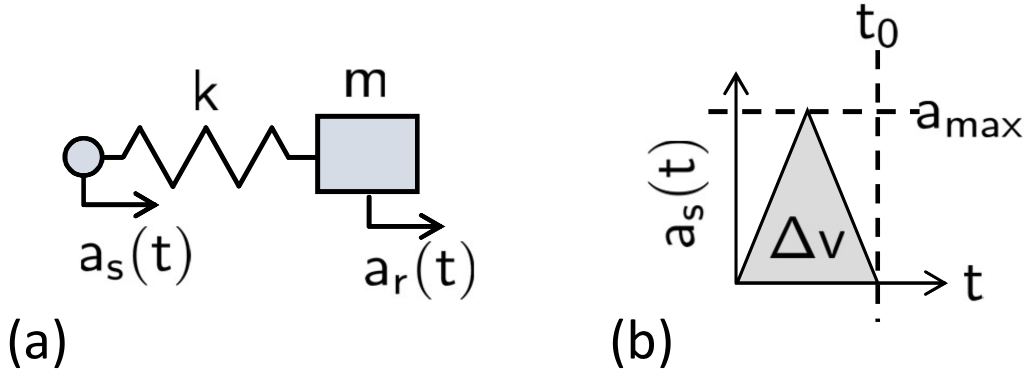

Figure 1.1: A simple lumped parameter model of a delicate object surrounded by a rigid shell, composed of a spring, mass, and excitation point, experiences internal loads when the excitation point is accelerated a prescribed amount, $a_s(t)$. (a) Diagram of the spring-mass representation of a delicate object that is adhered to a rigid shell. The rigid shell is forced to follow the acceleration history $a_s(t)$, which causes the mass to accelerate by the amount $a_r(t)$. The excursion of the spring, which is proportional with $a_r(t)$, represents the stress or strain within the delicate. (b) Two important parameters that describe the acceleration pulse, $a_s(t)$, are the maximum of the magnitude of the acceleration, a_{max}, and the magnitude of the velocity change, Δv.[23]

characteristic time of the object, then the system can be categorized as exhibiting the "short-pulse response," since the various responses to a range of short pulses all share some of the same features.

In the long-pulse response, both the mass and excitation point accelerate approximately the same amount at all times, and the spring deforms in proportion to the spring force needed to drive the mass at the same acceleration level as the excitation point. During the entire impact, the time-dependence of the spring's deformation approximately mirrors the acceleration of both the excitation point and the mass. Therefore, the extent of deformation is correlated with the maximum of acceleration of the excitation point, for long impacts. When the impact is shorter than the critical impact duration of the delicate object, T_c, the deformation within the spring is proportional with the velocity change, Δv, of the excitation point. The precise meaning of the "velocity change" in this scenario is defines as the difference between the final velocity coordinate and the initial velocity coordinate,

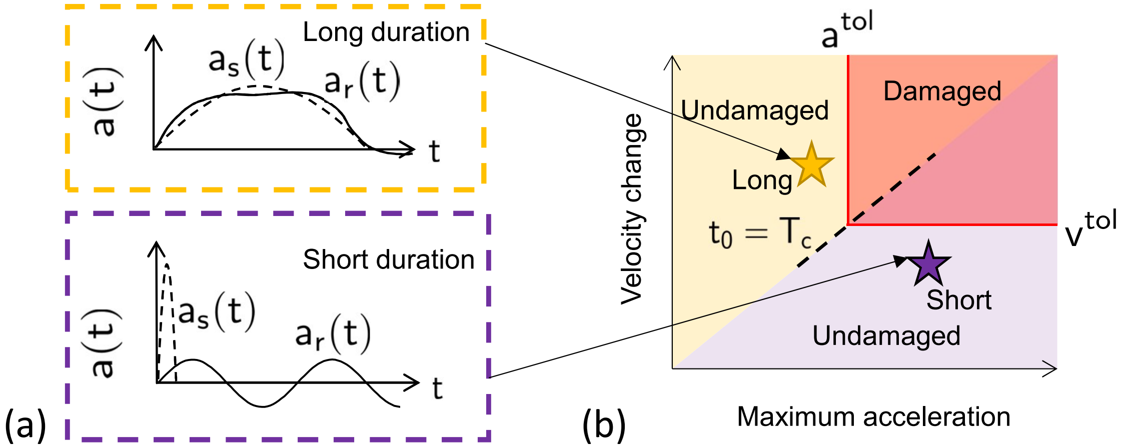

Figure 1.2: Kinematic injury criteria regimes for a simple lumped parameter model are differentiated by impact duration. (a) Short impacts have short-duration acceleration pulses and responses that are delayed with respect to the completion of the acceleration pulse. Long-duration impacts have responses that match the time-dependence of the acceleration pulse. (b) If exceeding a maximum tolerable level of stress or strain leads to damage, then damage may also be detected with an acceleration and velocity tolerance, a^{tol} and v^{tol}, respectively, which are related by the critical impact duration, T_c. If a short acceleration pulse results in a change in speed that exceeds to the tolerance of the delicate object, damage occurs. If the acceleration pulse duration is longer than the critical time T_c, then an acceleration tolerance is more appropriate. [23]

$\Delta v = v_f - v_0$.

For many objects, exceeding a fixed critical deformation threshold is believed to cause damage, even if the exact critical value is unknown. For delicate objects of this kind, it can be seen that the impulse, which can be calculated from the velocity change of the excitation point of the system, is the cause of deformation during short impacts. For long impacts, exceeding the deformation threshold will be due to exceeding an acceleration threshold. Consequently, successfully protecting a delicate object from impact requires that either the force applied to the delicate object be reduced so that the acceleration is below the critical acceleration of the delicate object, or the impulse be reduced so that the velocity change during an impact is lower than its corresponding critical value. These two paths to transforming a harmful impact into a safe impact, using a cushion, are shown in Figure 1.3.

Translation in multiple dimensions is beyond the scope of this thesis, but it should be noted that the vector characteristics of velocity must be taken into account when considering such cases. Even with limiting this discussion to one-dimensional translation only, some ambiguity in the meaning of "velocity change" emerges if negative velocities are considered. Since the velocity change introduced by Kornhauser and Lawton operates in a one-dimensional context, where velocity has but one component, and the acceleration always points in the positive direction, the velocity of the excitation point is always oriented in the same direction, and has a positive coordinate. For simplicity, the change in the coordinate for the single positive component of the velocity vector is referred to as the "velocity change" in that work. However, the concept of the velocity change can be generalized by introducing the concept of the magnitude of the velocity change, $|\Delta\vec{v}| = |\vec{v}_f - \vec{v}_0|$. The magnitude of the velocity change, $|\Delta\vec{v}|$, is the magnitude of the vector difference between the initial velocity and the final velocity. If the system is initially at rest, and the one-dimensional acceleration vector is never negative, as in the work of Kornhauser and Lawton, then the velocity change, the magnitude of the velocity change, and the change in speed, $\Delta|v|$, of the system are all equivalent. However, the magnitude of the velocity

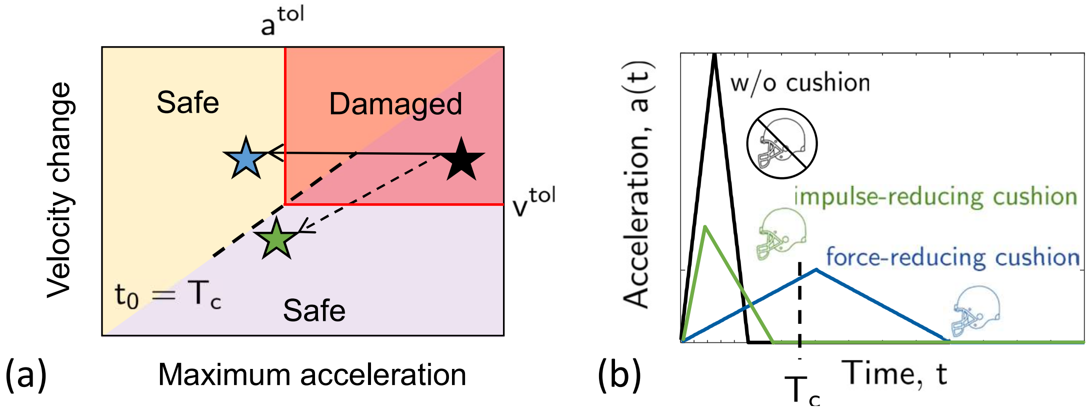

Figure 1.3: Two approaches to mitigating impact severity. (a) There are two paths to converting a damaging impact (black star, in the red region) to a safe impact (outside the red region). One approach uses energy dissipation to reduce the impulse and velocity change (green star). The other approach extends the duration of the impact to reduce the peak force and acceleration (blue star). (b) Example sketch of the acceleration of the skull during impacts with no head protection (black), an impulse-reducing cushion (green), and a force-reducing cushion (blue).

change, $|\Delta\vec{v}|$, and the change in speed, $\Delta|v|$, are separate quantities, and only the magnitude of the velocity change, $|\Delta\vec{v}|$, is truly correlated with the extent of deformation within the delicate object.

In some circumstances, it is not obvious whether a strategy that is based on lowering the magnitude of the velocity change to address the short impact response, or lowering the acceleration magnitude to address the long impact response will produce the best results. Since the introduction of a protective cushion lengthens the duration of the impact, a transition from the short-impact response to the long-impact response can occur when a cushion is added. The duration of the impact without a cushion, and the characteristic time of the delicate object, which is the critical impact duration for the transition from short- to long-impact response, should both influence the choice between emphasizing force or impulse, when designing a cushion.

1.2 Incorporating visco-elasticity into cushion design

While design of packaging to mitigate forces can be achieved by the use of compliant elastic cushions [13], with no limitations to repeated use, the design of packaging to mitigate impulse is more difficult. In particular, it requires the dissipation of energy. The bicycle helmet is one well-known example of packaging that protects by dissipating energy, by crushing and fracturing during an accident. However, a common feature of these kinds of dissipative cushioning structures is that they can only be used once. After a single use, the packaging needs to be replaced [35]. If multiple-use packaging is required, mechanisms of plasticity and fracture will result in less effective protection with each subsequent impact.

In Chapter II, a numerical model is used to demonstrate how a visco-elastic cushion can minimize both the deceleration and the one-dimensional velocity change of a mass with a known amount of initial kinetic energy. Specifically, a fractional Standard Linear Solid model is chosen to represent the cushion because it accurately reflects the glass transition behavior of real, rather than idealized, visco-elastic materials with a relatively small number of parameters [34]. The acceleration of the delicate object, its total velocity change, and the strain within the cushion are calculated by simulating impacts, using the mathematical method of Atanackovic [3]. Dimensionless results for the strain within the cushion, acceleration, velocity, and impact duration are obtained and expressed as functions of known dimensionless parameters that describe the impact scenario. Then, these results are used to construct a design framework for building visco-elastic cushions for objects with fragile interiors.

1.3 Mild traumatic brain injury

Although many aspects of mild traumatic brain injury are still areas of ongoing research, it is broadly accepted that mild traumatic brain injuries are due to the rapid motion of the head causing dangerous levels of deformation within the brain [16], [4]. Therefore, it was hypothesized that the prevention of mild traumatic brain injuries due to collisions in contact sports is a possible application of the cushion described in Chapter II. Demonstrating that the cushion in Chapter II can prevent head injuries requires that the sources of damage in a potentially harmful collision are of the same kind that are addressed by the cushion. To do that, the fundamental causes of deformation within the brain must be identified, and cast in a format that is appropriate for comparisons with the performance metrics of the cushion. Put in practical terms, if it is known that the cushion can reduce acceleration and velocity change, it must then be determined whether reducing acceleration or velocity change will decrease deformation within the brain.

At the most fundamental level, linear and rotational motion of the skull are expected to produce different types of deformation within the brain. Further, the relative affect of these two different types of motion on the extent of damage during an impact is also a subject of current debate. As early as 1971, it was suggested that linear skull motion was correlated to pressure-driven injury, whereas rotation could be correlated with strain-driven injury [38]. Ommaya et al. also list evidence of the differentiation between linear (translational) impacts and those that involve rotation in a 1994 review article [31], though discussion of the relative influence and possible interaction of these two types of motion continues [10, 21]. It is also recognized that rotation of the skull about different anatomical axes produce different responses within the brain. As with linear motion, angular acceleration and angular velocity of the skull produce mechanical loads within the brain, and rotational analogs to the kinematic quantities used by Kornhauser and Lawton that can predict deformation are of importance. A theoretical framework based on angular acceleration, $\ddot{\theta}$, and angular velocity, $\dot{\theta}$, underpins foundational animal experiments by Ommaya and colleagues in the 1960's and 70's. Therefore, both linear motion and rotational motion of the skull are considered in this thesis.

The analysis presented in Chapters III-VI represents a compromise between extremely simplistic models of head injury and extremely elaborate models of brain deformation, which each have their advantages and disadvantages. The idealized continuum models used in this thesis are used because they combine some of the advantages of each. They are used to show that the brain deforms in proportion with both linear and rotational kinematic quantities, and exhibits aspects of both the short and long impact response described in Section 1.1. The simplest approach to modeling the internal dynamics of a delicate object is the single-degree-of-freedom lumped parameter model, like the one used by Kornhauser and Lawton. Other variations on this approach, like the single-degree-of-freedom model proposed by Gabler et al. [11] and the multiple-degree-of-freedom model of Laksari et. al. [24], are quite useful in representing the essential frequency response of the human head, but since they are themselves derived from observations of brain response or simulations of brain response, they are mainly phenomenological in nature. Additionally, the lack of a spatial dimension in a lumped parameter model severely limits its usefulness in describing the response of continuum objects that are vulnerable throughout their volume. To describe the response of different regions of a continuum body requires more than one position variable, and so the lumped parameter approach is not capable of calculating the maxima of certain variables, like strain, across the entire body in many circumstances. The simplest lumped parameter models cannot address shear deformation and volumetric deformation simultaneously, either. Since both types of deformation are caused by head impacts, it is necessary to use a more sophisticated continuum model which is able to capture them both at once.

Numerous studies over several decades have taken a continuum mechanics-based approach to correlate deformation with observable impact kinematics. Early studies relied on analytical calculations of motion for idealized geometries [25] but more recently, elaborate finite element models of reconstructed impacts are more popular. Often, reconstruction studies employ sophisticated material models and detailed geometry in simulated head impacts that replicate the mechanical observations of experiments and in-situ impacts with as much fidelity as possible [21, 40, 11, 10, 19]. These efforts are related to the work of identifying tissue-level thresholds of deformation and stress that correlate with brain injury. On occasion, these efforts coincide, as finite element reconstructions of impacts that led to injury are used as a basis for arguing in favor of, or against, certain tissue-level damage metrics and kinematic injury criteria [22]. Attempts to distinguish which kinematic variables are most correlated with deformation, such as [10] and [21], are dependent on accurately modeling the mechanical response of brain tissue. For example, recent work by Zhao et al. examines how the different constitutive laws used to represent the brain influence the numerical results a model generates, and determines that calculations of peak principal strain depend extremely heavily on the time-varying shear modulus assumed for the brain [44]. However, consensus on the correct material models for brain tissue is absent, and the strain predictions obtained from human head finite element models inherit this uncertainty [6, 44].

Therefore, a simple continuum model, that captures the general behavior of the whole brain during an impact event, but which does not assume a particular set of constitutive parameters for the brain, is helpful in identifying which kinematic aspects of an impact are most relevant to deformation calculations. These calculations of strain, from hypothetical impacts, can be used to predict helmet efficacy. The link between first principles, such as the relationship between shear modulus and shear wave speed, and observable differences in injury thresholds for different impacts, is made possible by recasting the impact problem in a dimensionless form in Chapters 3-6. In turn, attaining the dimensionless form of the impact events considered in this study is achieved by choosing simple material models and a small number of impact description parameters. Situating the results obtained from finely detailed finite element models within the context of a general framework obtained from simple models, like the one proposed in this thesis, is also advantageous because the effect of adding complexity in an aspect of the finite element model can be isolated by these effort, and then studied.

The relative ease of fabricating and and detecting deformation within this class of delicate objects is an additional benefit to choosing the simple cylindrical geometry used in Chapters III-VI. Although an anatomically-detailed model of the human brain has some advantages, physically assembling such a complex structure, and fully characterizing the constitutive properties of all its components, is beyond the scope of this project. Using a radially symmetric model also greatly eases difficulties in discussing skull rotation, and the circumferential brain motion that attends it. Simple geometry and constitutive laws that facilitate the development of physical models to experimentally characterize cushion performance are therefore quite suitable for this effort.

1.4 Using scaling laws that relate strain to kinematic variable in order to design cushions for preventing head injury and inform future numerical modeling efforts

Data describing the head impacts that athletes are currently experiencing can be obtained by analyzing video records of impacts, or using accelerometer data. Injuries are detected clinically, but the efficacy of a helmet needs to be verified long before a player uses it regularly. Scaling laws relating kinematic variables of the impact to local measures of injury risk, like the maximum principal strain, are essential tools for using mechanical analysis techniques to verify helmet efficacy and designing helmets that take dynamic response of the brain into account.

These types of scaling laws are useful in several ways. First, scaling laws that incorporate kinematic quantities, the impact duration, and the magnitude of a deformation measure, can be used to isolate the kinematic quantity that best correlates with increased levels of deformation. For instance, if the ratio of the maximum shear strain to the maximum magnitude of the angular velocity of the skull is constant, even for impacts of different durations, we conclude that a cushion that significantly reduces the maximum magnitude of the angular velocity during a rotational impact will provide more protection than one which only diminishes the angular velocity slightly. This type of analysis sets up future work in identifying an angular-velocity-based injury criterion that is predicated on the idea that a single threshold angular velocity change value for the skull can indicate that a strain-based tissue threshold has been reached within the brain.

Relatedly, the scaling laws that will be developed in Chapter VI are helpful in distinguishing categories of impact from one another. Even though observable quantities which take on a single numerical value are the most helpful in estimating the severity of impacts, a single parameter is not enough to fully predict the distribution of strain within even a simple object like the visco-elastic cylinder we study here. In fact, angular acceleration pulses with the same maximum angular acceleration values, and the same maximum angular velocity values, sometimes produce different amounts of strain within the cylinder. Although single-valued functions of the angular acceleration and angular velocity of the skull are enough to estimate the approximate magnitude of the strain, additional information about the time-dependence of the angular acceleration pulse is necessary for determining how long the high deformation lasts within the brain, and is useful in obtaining even more accurate estimates of strain. The analysis of the influence of the time-dependence of acceleration is accomplished through considering a few different dimensionless pulse shapes, which span a range of qualitative angular acceleration pulse characteristics.

The third way that these scaling laws are useful is related to concerns with developing accurate models of the human brain, and being able to anticipate how judgement calls in the development of numerical models may bias the model outputs. For example, throughout Chpater V and Chapter VI, we will consider two plausible sets of parameters for modeling the human brain's visco-elastic response. One set of parameters represents a material which is fairly dissipative in the frequency range of the brain's response to rapid rotational loads. The other set produces a response which is not very dissipative of the shear strain waves generated by these types of impacts. The time-dependent strain fields that develop within cylinders that are modeled with these two sets of parameters differ in important ways. Knowing how over-predicting or under-predicting the damping performed by the brain's visco-elasticity has import applications in choosing model parameters which will not over-predict the performance of helmets or under-estimate the severity of an on-field impact to an athlete's head.

1.5 Organization of the Thesis

The goal of this investigation is to develop a visco-elastic cushion and determine its applicability to the mitigation of mild brain injuries by identifying scaling laws that correlate deformation within the brain with skull motion, and identifying the characteristic times that govern transitions from one type of response to another. It is known that both linear motion of the skull, and rotational motion, produce internal stress and deformation within the brain, so both categories of kinematic loading are addressed.

This primary goal will be achieved by:

(i). Providing a conceptual framework for the design of a visco-elastic cushion applicable to both rapid impacts and impacts of long duration [Chapter II].

(ii). Calculating the pressure and strain within a brain-like delicate object that experiences a prescribed amount of linear acceleration [Chapter III].

(iii). Developing and validating an analytical model for shear strain due to rotational motion of the skull-like shell surrounding a brain-like delicate object [Chapter IV].

(iv). Characterizing the features of the short and long-duration asymptotic response of the brain-like delicate object [Chapter V].

(v). Identifying scaling laws involving material properties and brain size to estimate deformation within a brain-like delicate object subject to a variety of rotational loads [Chapter VI] (vi). Determining the characteristic times that delineate the regions in which different scaling laws for deformation and kinematics are applicable [Chapter VI]

(vii). Identifying qualitative aspects of the impact kinematics that influence strain levels [Chapter VI]

CHAPTER II

The use of visco-elastic materials for the design of helmets and packaging

2.1 Introduction

Protective packaging can be used to reduce the risk of damage to delicate objects from accidental impact during transportation or use. In the form of armor, packaging can also provide protection for objects that may be the target of deliberate attack by blast or by projectiles. Helmets or pads that protect the brain, soft tissues, or bones during contact sports also function as protective packaging.

A common perspective is the assumption that packaging serves as no more than a cushion, decreasing the magnitude of the force acting on an object that needs to be protected [13]. This can be achieved by using a large quantity of a very soft material, such as a foam or airbag, for the cushion. Upon impact, the cushion deforms at low loads, limiting the transmitted force. This is one valid design strategy that is discussed later in this paper.

However, a focus on reducing the magnitude of the force transmitted to an object neglects the dynamic aspects of damage. All structures have both density and compliance. Therefore, inertial effects give rise to transient dynamic stresses and strains that can then cause damage to an object as the result of an impact or blast. In particular, the behavior of a compliant body enclosed within a stiff outer casing and subjected to a rapid change in motion can be dominated by these transient waves. As a result of these inertial effects, there are conditions under which effective packaging requires mitigation of the impulse, rather than the force, resulting from an impact [35].

Which protective strategy, mitigation of force or impulse, needs to be employed depends on the duration of the impact compared to a characteristic period, T_c, of vibrations of the dynamic system. It can be shown for a linear, lumped-parameter, dynamic system, with motion in only on dimension, that an assumption of damage being associated at a local scale with a critical level of stress or strain can be recast at a global scale in approximate, but reasonably realistic, terms, as a critical maximum acceleration, a^{tol}, or a critical magnitude of the velocity change, v^{tol}, depending on the duration of the impact [35, 23]. Although a more elaborate symbol could be devised for the critical magnitude of the velocity change, such as $|\Delta\vec{v}|^{tol}$, the symbol v^{tol} is used instead to facilitate comparisons with the critical maximum acceleration, a^{tol}. If the impact is relatively long compared to the characteristic period of the dynamical system, then it is the transmitted force that needs to be limited to prevent damage. This is equivalent to limiting the peak acceleration of the object being protected. If the impact is relatively short compared to the characteristic time of the dynamical system, then it is the magnitude of the transmitted impulse that needs to be limited. This is equivalent to limiting the magnitude of the velocity change of the object being protected. The magnitude of the velocity change is a scalar quantity defined as

$$|\Delta\vec{v}| = |\vec{v}_r - \vec{v}_0| \tag{2.1}$$

where $\vec{v}_r$ is the rebound velocity of the delicate object after an impact, and $\vec{v}_0$ is the initial velocity of the delicate object. It should be noted that the magnitude of the velocity change, $|\Delta\vec{v}|$, is not the same as the change in the speed of the delicate object. The change in speed, defined as $\Delta|\vec{v} = \Delta|\vec{v}_r - \vec{v}_0|$, is not known to correlate with deformation due to one-dimensional translation of delicate objects. In the rest of this chapter, “velocity change,”

Δv, will refer to the magnitude of the velocity change, since the motion considered here is confined to one dimension and these terms are less cumbersome than the more specific term "magnitude of the velocity change" and rigorous symbol $|\Delta\vec{v}|$. The symbol Δv has the benefit of being consistent with the early work of Kornhauser and Lawton [23] on bodily injury due to impact.

The criteria described above can be illustrated graphically for a simple model in which the force transmitted to an object by an impact increases linearly with time to a maximum value of a_{max}, and then decreases linearly to zero, with the total duration of the impact being equal to t_d. If t_d is less than the characteristic time for the dynamic response of the object, T_c, damage will occur if the velocity change of the object is greater than a critical value, v^{tol}. If $t_d > T_c$, damage will occur if the maximum acceleration of the object is greater than a critical value, a^{tol}. For such a simple linear model, it can also be shown that the characteristic period can be replaced by $T_c = v^{tol}/a^{tol}$, so only two parameters are required to construct the damage map illustrated in Fig.2.1(a). This map shows schematically the regime of damage on a plot of Δv against a_{max} imparted to an object by the impulsive load, in terms of the critical velocity change and the critical acceleration for the object. The map also shows representative contours of how Δv varies with a_{max} during linear impacts of different durations.

It will be noted that there are two possible ways to interpret the design map shown in Fig. 2.1(a). The first perspective is that there is a critical velocity change criterion that applies for short impacts, and a critical acceleration criterion that applies for long impacts. The second perspective is that damage only occurs if both the velocity and acceleration criteria are met. This latter perspective provides a very powerful insight into the design of packaging: a safe design can be ensured by preventing one of the two criteria from being met; there is no need to focus on both. While real dynamic systems have a slightly more complex behavior than described here, this approach provides a good approximation for exploring the basic concepts pertinent to the design of packaging.

The human head represents a delicate dynamic system that requires protection against blast and impact, and the simple damage model described above has long been accepted empirically, even if not specifically described in such terms. For example, Holbourn [16] used model experiments to identify velocity-controlled and acceleration-controlled regimes of damage almost eighty years ago, while the alternative, but equivalent, perspective that both a velocity and acceleration damage criterion had to be met simultaneously was expressed almost twenty years later [23] in the context of the vulnerability of a mammalian body to impact. The form of Fig.2.1(a) captures the essential elements of the impact-sensitivity curves shown in Ref [23]. In addition, as we show in Fig.2.1(b), the empirical head-injury criterion known as the "Wayne-State Tolerance Curve" [39] can be approximately described by a maximum velocity change of about 4 m/s for very short impacts, a maximum acceleration of $40g$ for longer impacts, and a characteristic period of about 10 ms. Other head-injury criteria share similar characteristics [10], but all are complicated by the empirical requirements to accommodate the non-linear nature of the brain and multiple characteristic periods. Some head injury criteria recognize the status of velocity, acceleration, and corresponding angular quantities as vectors, but it is also quite common for researchers in this field to reduce one-dimensional and multi-dimensional vector quantities to related scalar quantities [21, 9, 26, 30, 17].

While design of packaging to mitigate forces can be achieved by the use of elastic cushions, with no limitations on repeated use, the design of packaging to mitigate impulse is more difficult. In particular, it requires the dissipation of energy. Well-known examples of packaging that protect by dissipating energy include crash barriers that deform plastically to reduce damage to cars, cars that dissipate energy within the crumple zone of the body [18], and bicycle helmets that crush and fracture to protect cyclists in accidents [**?**]. However, a common feature of all these packages is that their efficiency is greatly reduced after only one impact. After a single use, the packaging needs to be replaced or repaired (*e.g*, a bumper) to restore the efficiency.

In previous work we have shown how visco-elastic materials can dissipate energy and be used for repeated protection against very short-duration events such as blast [35]. In the present paper, we address the longer-duration events associated with impact, and demonstrate design principles of reusable visco-elastic packaging for impact. We do this in two steps. In the first portion of this paper we demonstrate a very simple analytical model of how a visco-elastic cushion can minimize both the deceleration and the velocity change of a mass with an initial level of kinetic energy associated with it. In the second section of the paper, we use these results to discuss a design framework for the use of visco-elastic cushions in packaging.

2.2 Mathematical model

In this section, we show how a visco-elastic cushion can control both transmitted force and impulse during an impact. This is done by considering the model illustrated in Fig.2.2. A rigid object of mass m per unit area is traveling at a speed v_0 towards a rigid wall. The velocity of the rigid object is a one-dimensional vector, $\vec{v}_o = v_o\hat{\imath}$. The rigid delicate object is to be protected from the resultant collision by a visco-elastic cushion of thickness h (assumed to have negligible mass). Upon impact with the wall, the visco-elastic cushion deforms. If the package consisting of the object and cushion has a coefficient of restitution (CoR) equal to zero, it is brought to rest as a result of the collision. If the impact is perfectly elastic, with a CoR equal to one, it will rebound with a speed of v_o in the opposite direction from its initial velocity, such that the rebound velocity is $\vec{v}_f = -v_o\hat{\imath}$. In practice, the CoR will be between these two limits, and the magnitude of the "rebound speed" is always less than v_o.

The analysis that follows can be done quite simply if the cushion is a standard linear solid (SLS), with a relaxed modulus of E_r, an unrelaxed modulus of E_u, and a relaxation time of τ_R. However, the use of such a model for a polymer over-estimates both the sharpness and the intensity of the damping peak compared to those of real materials. Therefore, in this paper we use a generalized Zener model, which is a four-parameter fractional visco-elastic model, or a fractional linear solid [34, 1], to model visco-elastic materials. At the cost of only a single extra material parameter, the fractional derivative order, α, this model does an excellent job of describing the behavior of real visco-elastic materials, without the many extra terms associated with a Prony-series representation.

The relationship between stress, σ, strain, ε, and time, t, for a fractional linear solid is given by [34]

$$\sigma(t) + \tau_R^\alpha \frac{d^\alpha \sigma(t)}{dt^\alpha} = E_r \varepsilon(t) + E_u \tau_R^\alpha \frac{d^\alpha \varepsilon(t)}{dt^\alpha} \ , \tag{2.2}$$

for small displacements. Alternatively, we could express this in terms of frequency (f), rather than time. The equation reduces to that for a standard linear solid when $\alpha = 1$. As a means of illustrating how the behavior of a fractional solid differs from a standard linear solid ($\alpha = 1$), the storage modulus, E', which relates the in-phase components of stress and strain [34, 41] is shown as a function of the normalized oscillation frequency, $\tilde{f} = f\tau_R$, in Fig 2.3(a) for different values of α. Figure 2.3(b) shows a corresponding plot for the loss factor, or $\tan\delta$ [34, 41].

When the visco-elastic cushion comes into contact with the rigid wall at time $t = 0$, the rigid body has an initial speed of v_o. As the boundary between the rigid body and the cushion displaces by the amount $u(t)$ (shown in Fig. 2.2(b)), a stress $\sigma(t)$ develops within the visco-elastic cushion that establishes the equation of motion for the rigid body:

$$\sigma(t) = -m \frac{d^2 u(t)}{dt^2} \ , \tag{2.3}$$

where m is the mass per unit area of the rigid body. $u(t)$ is the time-varying coordinate of displacement with respect to the basis vector $\hat{\imath}$. Recognizing that the normal component of strain in the cushion is given by $\varepsilon(t) = -u(t)/h$, this equation can be coupled with the constitutive relationship of Eqn. 2.2 to give a governing equation of

$$m\frac{d^2u(t)}{dt^2} + \tau_R^\alpha m\frac{d^{2+\alpha}u(t)}{dt^{2+\alpha}} = -\frac{E_r}{h}u(t) - \frac{E_u\tau_R^\alpha}{h}\frac{d^\alpha u(t)}{dt^\alpha} \ , \tag{2.4}$$

with initial conditions:

$$u(0) = 0, \tag{2.5}$$

$$\left.\frac{du(t)}{dt}\right|_{t=0} = v_o \ , \tag{2.6}$$

and

$$\left.\frac{d^2u(t)}{d^2t}\right|_{t=0} = 0 \ . \tag{2.7}$$

These initial conditions reflect the fact that no contact force is developed at the instant of initial contact between the cushion and rigid mass, so there is no deceleration of any portion of the rigid mass at $t = 0$.

The equations listed in terms of parameters with dimensions in the previous paragraph can be re-expressed in a non-dimensional form as

$$\frac{d^2\tilde{u}(\tilde{t})}{d\tilde{t}^2} + \tilde{\tau}^\alpha\frac{d^{2+\alpha}\tilde{u}(\tilde{t})}{d\tilde{t}^{2+\alpha}} = -\tilde{E}\tilde{u}(\tilde{t}) - \tilde{\tau}^\alpha\frac{d^\alpha\tilde{u}(\tilde{t})}{d\tilde{t}^\alpha} \ , \tag{2.8}$$

with

$$\tilde{t} = t\left(\frac{E_u}{mh}\right)^{1/2} \ ,$$

$$\tilde{u}(\tilde{t}) = u(t)\left(\frac{E_u}{mv_o^2h}\right)^{1/2} \ ,$$

$$\tilde{E} = E_r/E_u \ ,$$

and

$$\tilde{\tau} = \tau_R\left(\frac{E_u}{mh}\right)^{1/2} \ .$$

The non-dimensional initial conditions are

$$\tilde{u}(0) = 0 \ , \tag{2.9}$$

$$\left.\frac{d\tilde{u}(\tilde{t})}{d\tilde{t}}\right|_{\tilde{t}=0} = 1 \ , \tag{2.10}$$

and

$$\left.\frac{d^2\tilde{u}(\tilde{t})}{d\tilde{t}^2}\right|_{\tilde{t}=0} = 0 \ . \tag{2.11}$$

2.3 Results

An analytical approach for solving Eqn. 2.8 is described in [3]. In the present case, the equation was solved numerically using the commercial code Matlab[1], with a new variable $\tilde{x}(\tilde{t}) = \tilde{u}(t) - \tilde{t}$ being introduced, and the equations being rewritten in terms of $\tilde{x}$ and its derivatives. The form of Eqn. 2.8 shows that the dimensionless coordinate of displacement, $\tilde{u}(\tilde{t})$, of the rigid mass is a function of only $\tilde{E}, \tilde{\tau}$, and α. The non-dimensional coordinates of velocity, $\tilde{v}(\tilde{t})$, and acceleration, $\tilde{a}(\tilde{t})$, of the rigid block can be readily expressed as

$$\tilde{v}(\tilde{t}) = \frac{d\tilde{u}(\tilde{t})}{d\tilde{t}} = \frac{v(t)}{v_o} \tag{2.12}$$

and

$$\tilde{a}(\tilde{t}) = \frac{d^2\tilde{u}(\tilde{t})}{d\tilde{t}^2} = \frac{a(t)}{v_o}\left(\frac{mh}{E_u}\right)^{1/2} \ . \tag{2.13}$$

Typical examples of how the non-dimensional magnitude of acceleration varies with time while the package is in contact with the rigid wall are shown in Fig. 2.4. From plots such as these, the non-dimensional duration of the impact, $\tilde{t}_d$, and the maximum non-dimensional magnitude of acceleration, $\tilde{a}_{max}$, corresponding to the maximum force exerted on the object, can be found. These are plotted in Figs. 2.5 and 2.6, as functions of $\tilde{\tau}$, and

---

[1] The MathWorks Inc.

for different values of $\tilde{E}$ and α.

The other quantity that is important from a packaging perspective is the magnitude of the velocity change as a result of the impact; it is proportional to the impulse transmitted by the wall to the package. If v_f is the speed with which the package leaves the wall, the magnitude of the change in the non-dimensional velocity is given by

$$\Delta\tilde{v} = 1 - \frac{v_f}{v_o} \,. \tag{2.14}$$

This can vary between 2, for a perfectly elastic collision (maximum impulse transmitted to the package), and 1, for a perfectly plastic collision (minimum impulse transmitted to the package, consisting of the rigid mass and cushion). Plots of how $\Delta\tilde{v}$ depends on the properties of the visco-elastic cushion are shown in Fig. 2.7.

It will be observed from these figures and the non-dimensionalization scheme that the relaxation time of the visco-elastic cushion interacts with the unrelaxed modulus and thickness of the cushion, as well as with the mass of the body, to provide an ability to tune the package so that the cushion can either behave as a stiff elastic material (large $\tilde{\tau}$), a compliant elastic material (small $\tilde{\tau}$), or as an energy-dissipating visco-elastic material (intermediate $\tilde{\tau}$). Of particular note is that it is possible to tune the system so that the CoR of the collision is almost zero (as in a perfectly-plastic collision), especially if α is close to one, and $\tilde{E}$ is very small. However, in this case the deformation is not plastic, but is fully reversible, since the system is visco-elastic.

The thickness of the visco-elastic cushion enters the normalization of $\tilde{\tau}$ as one of the parameters that can be used to tune the design of the package. However, it should be recognized that, in general, there will be a limiting compressive strain ε_{max} above which the governing equations may no longer hold. For example, if there is a densification strain for a foam. Therefore, part of the design process for the packaging must also include a calculation of the maximum compressive displacement, u_{max}. The non-dimensional maximum displacement, $\tilde{u}_{max} = u_{max}\sqrt{E_u/mv_o^2h}$ is plotted as a function of the packaging parameters in Fig. 2.8. The design of the packaging is then subject to a constraint that

$$\tilde{u}_{max} < \varepsilon_{max}\sqrt{\frac{E_u h}{mv_o^2}} \; . \tag{2.15}$$

2.4 Discussion

The results of the previous section can be used to illustrate the process by which one might design packaging for the limiting case to protect a delicate dynamic system contained within a relatively massive supporting structure. For the purposes of this discussion, it will be assumed that damaging internal strains within the dynamic system are induced when both the velocity change and the acceleration magnitude of the supporting structure exceed their respective critical values of v^{tol} and a^{tol}. As discussed in the introduction, this can also be interpreted as two distinct failure criteria for short and long impacts. It is recognized that this is a slight over-simplification even for a linear dynamic system, and certainly for a non-linear system like the brain, but it provides a very useful example of how the design and materials selection for packaging might proceed.

2.4.1 General principles

By way of introduction, first consider an object moving with an initial speed such that $v_o/v^{tol} < 0.5$. Even if the collision with a rigid wall is perfectly elastic, the damage criterion will not be met, because the magnitude of the velocity change, which will be equal to $2v_o$, is less than v^{tol}. Any energy dissipation that might occur will result in a smaller velocity change. As discussed in the introduction, damage requires both the velocity and the acceleration criterion to be met. So, since the magnitude of the velocity change can never exceed v^{tol}, no protection is needed against an impact at these low initial velocities.

Conversely, now consider an object moving with an initial speed such that $v_o/v^{tol} \geq 1$.

Now, even for a perfectly plastic collision, the magnitude of the velocity change will exceed v^{tol}. Therefore, the velocity damage criterion will always be met, no matter how the packaging is designed. Damage of the object can only be avoided if a_{max} is reduced to a value below a^{tol}. Such a reduction in a_{max} can be achieved by extending the duration of the impact.

Inspection of Fig. 2.6 shows that $\tilde{a}_{max}$ is generally a monotonic function of $\tilde{\tau}$, so that decreasing $\tilde{\tau}$ reduces $\tilde{a}_{max}$. Therefore, to reduce a_{max} to below the threshold for damage requires $\tilde{\tau}$ to be reduced below a critical value for given values of α and $\tilde{E}$. This can be done by increasing the thickness of the visco-elastic cushion, and a second step in the design process is then to ensure that this thickness also satisfies the deformation constraint of Eqn. 2.15.

Finally, consider an object moving with an initial speed such that $0.5 < v_o/v_{tol} < 1$. Now the packaging can be designed using either a velocity-controlled approach or an acceleration-controlled approach. The acceleration-based approach has been described above. To avoid a velocity-controlled failure, one must ensure that $\Delta\tilde{v} < \left(v_o/v^{tol}\right)^{-1}$. From Fig. 2.7, it can be seen that this imposes an upper and lower bound on $\tilde{\tau}$ for a safe polymer cushion, depending on the corresponding values of both α and $\tilde{E}$.

As discussed above for the design of acceleration-controlled packaging, the deformation constraint of Eqn. 2.15 is also a concern. This can be addressed by using Fig. 2.8 to obtain the value of $\tilde{u}_{max}$ corresponding to the choice of $\tilde{\tau}$, α, and $\tilde{E}$. The minimum thickness of the polymer cushion to avoid excessive deformation is then given by

$$h > \left(\frac{\tilde{u}_{max}}{\varepsilon_{max}}\right)^2 \frac{mv_o^2}{E_u} \; . \qquad (2.16)$$

Different polymers will be defined by different values of $\tilde{\tau}$, α, $\tilde{E}$, E_u and ε_{max}, so a systematic search through candidate materials can result in the appropriate material to minimize the thickness based on satisfying either the acceleration constraint or the velocity constraint, remembering that only one has to be satisfied for a safe design. The addition of a polymer density into the equations would allow a search for a minimum mass of cushion to be conducted.

2.4.2 Design optimization

The approach outlined above can be refined using the design approach of Ashby [2]. For the purposes of the illustration, we will assume a design problem in which a mass m is travelling at an initial speed such that that $v_o/v^{tol} = 0.8$. In this case both a velocity-controlled approach and an acceleration-controlled approach can be explored; it is assumed that there is a second failure criterion of a^{tol}. We will also assume that the optimization parameter is the thickness of the cushion. Therefore, we are looking for a solution that minimizes h from a universe of different polymers having fixed but known values of τ_R, E_u, E_r, and α.

2.4.2.1 Velocity constraint

If one first considers the velocity criterion, it can immediately be seen from Fig. 2.7 that there is a subset of material properties (corresponding to low values of α and high values of $\tilde{E}$) for which $\Delta\tilde{v} \geq 1.25$. This forms a group of materials that cannot be used to satisfy the velocity constraint for this particular example where $v_o = 0.8v^{tol}$. Figure 2.9 shows a more complete map for safe design when $v_o = 0.8v^{tol}$, in terms of all three non-dimensional material parameters, α, $\tilde{E}$, and $\tilde{\tau}$. Similar maps can be constructed for different values of v_o/v^{tol} in the range of 0.5 to 1.0, with all materials being able to satisfy the velocity constraint below the lower end of this range, and with no materials being able to satisfy the velocity constraint above the higher end. It will be observed from Fig. 2.9 that, for a given value of $\tilde{E}$ and α, there is a lower and an upper bound for $\tilde{\tau}$ that will allow the velocity constraint to be met.

If these lower and upper bounds for the acceptable range of $\tilde{\tau}$ corresponding to a given set of values for α and $\tilde{E}$ are denoted by $\tilde{\tau}_1$ and $\tilde{\tau}_2$, respectively, one can see that for any acceptable polymer there are corresponding constraints on the thickness:

$$\left(\frac{\tau_R}{\tilde{\tau}_2}\right)^2 \frac{E_u}{m} = h_2 < h < h_1 = \left(\frac{\tau_R}{\tilde{\tau}_1}\right)^2 \frac{E_u}{m} \tag{2.17}$$

This is subject to a third constraint on the thickness of the cushion provided by Eqn. 2.16. If this minimum thickness required to satisfy the strain constraint calculated at $\tilde{\tau} = \tilde{\tau}_1$ from Fig 2.8, h_3, is greater than h_1, then the use of a velocity criterion will not result in a valid design. Conversely, for all polymers that satisfy $h_3 < h_1$, the approach of Ref. [2] for multiple constraints can be used to find the optimal polymer that satisfies the velocity constraint.

2.4.2.2 Acceleration constraint

After the optimal design based on velocity control has been identified, a second type of analysis needs to be conducted to assess whether a more efficient design can be found using acceleration control. In other words, one must consider whether a more efficient design can be achieved by satisfying the acceleration constraint of $a_{max} < a^{tol}$. This is a rather more complicated step since the normalization of the acceleration given earlier includes the thickness, which is the parameter being minimized. From this normalization, one can see that acceleration control requires the thickness to be greater than a critical value:

$$h > h_4 = \tilde{a}^{*^2}_{max} \left(\frac{v_o}{a^{tol}}\right)^2 \frac{E_u}{m} \ , \tag{2.18}$$

where $\tilde{a}^*_{max}$ can be an arbitrary value within the range of the plots shown in Fig. 2.6. For a given polymer, $\tilde{a}_{max}$ generally increases with $\tilde{\tau}$. So, if one sets a value of $\tilde{a}^*_{max}$, this corresponds to a value of $\tilde{\tau}^*$ for a given polymer, and one can establish another constraint on h:

$$h > h_5 = \left(\frac{\tau_R}{\tilde{\tau}^*}\right)^2 \frac{E_u}{m} \ . \tag{2.19}$$

Both of these constraints must be met, with the minimum thickness being established by the smaller of the two. However, if one tries to reduce h_4 by reducing $\tilde{a}^*_{max}$ for a given polymer, h_5 is increased as the result of reducing $\tilde{\tau}^*$. In this case, one can establish an optimum value of h by equating h_4 to h_5. A new requirement that

$$\tilde{a}^*_{max}\tilde{\tau}^* = \tau_R a^{tol}/v_o \ . \tag{2.20}$$

emerges from this analysis.

This equality of Eqn. 2.20 can be plotted as straight lines on Fig. 6, corresponding to different values of $\tau_R a^{tol}/v_o$, and the optimum point can be found from the intersection of the line with the plot. From this, the optimum value of $\tilde{\tau} = \tilde{\tau}_{opt}$ can be found, and then used to find the corresponding optimum value of $h = h_{opt}$. Once this has been determined, the corresponding value of $\tilde{u}_{max}$ can be found from Fig. 8. This value of $\tilde{u}_{max}$ can be used to deduce yet another minimum constraint on the thickness $h = h_6$, from Eqn. 2.16. The larger of h_{opt} or h_6 then provides the minimum thickness required to satisfy the acceleration constraint.

Finally, the solutions from both the velocity-controlled calculations and from the acceleration-controlled calculations have to be compared, and the smallest value of the two thicknesses is the optimal solution for packaging that provides protection with a minimum thickness by satisfying either the velocity constraint or the acceleration constraint.

2.4.2.3 An experimental implementation

As part of the authors' submission in the final round of the Head-Health Challenge-III competition in 2017, we used the design concepts described above to develop a system to minimize the coefficient of restitution in a drop-tower test.

The University of Michigan entry to this competition used an open-cell polyurethane foam provided by a polymer manufacturer. We characterized the frequency response of this material using a fractional-derivative model reduced to a reference temperature of 21$^{\text{o}}$C, as shown in Fig. 2.10. As an example, the fitting parameters shown in Fig. 2.10 are $E_u = 17$ MPa, $E_r/E_u = 0.0023$, $\alpha = 0.59$, and $\tau_R = 4 \times 10^{-5}$ s. The cushion had a diameter of 51 mm, a height of 45 mm, and a mass of 26 g. The drop tower contained an anvil with a mass of 2.85 kg. As part of the design process, we noted that our system had to be stiffened very slightly to accommodate the loads resulting from bigger drops. However, these pillars were slightly recessed from the top of the foam, and, therefore, didn't contribute significantly to the energy dissipation at the lowest impact energy of 12.5 J, discussed here.

Using the analysis presented in this paper, and including uncertainties to the fitting properties, we calculated a coefficient of restitution in the range of 0.25 to 0.32, and a maximum transmitted force of 600 ± 200 N. These should be compared with a measured coefficient of restitution of 0.25 ± 0.02, and a transmitted force of 920 ± 10 N for our reinforced foam design. In this context, it is noted that similar measurements on two commercial products designed to dissipate energy in a football helmet, with similar dimensions and masses, gave coefficients of restitution greater than 0.5, and transmitted forces in the range of 1100 to 1300 N.[2]

2.5 Conclusions

In this paper we have discussed the strategies for using visco-elastic materials to design packaging of delicate dynamic structures, such as the head and brain. Failure of such objects occurs as the result of both an excessive velocity change and an excessive acceleration. The velocity constraint is responsible for damage with impacts that are relatively short compared to a characteristic time for the dynamic response of the object, while the acceleration constraint is responsible for damage with longer impacts. However, it is a valid protection strategy to mitigate only one of the criteria, since both need to be satisfied for damage to occur.

For impacts of long duration, mitigation has to be focussed on reducing the acceleration of the object to be protected, by lowering the transmitted force below a critical threshold. This can be done by using a compliant cushion, such as an elastic foam. For impacts of short duration, mitigation can occur by reducing the velocity change of the object to be protected, by lowering the transmitted impulse to below a critical threshold. Alternatively, mitigation can occur by using a compliant material to increase the duration of the impact, moving the problem to the acceleration-controlled regime and ensuring that the acceleration constraint is met for a safe design. If a strategy of reducing the impulse is to be pursued, without resorting to massive armor, then energy needs to be dissipated. However, it should be recognized that this strategy of energy dissipation can reduce the transmitted impulse only by a factor of two, at most.

Energy dissipation generally requires permanent damage such as plasticity or fracture.

---

[2] A video of the drop tower experiment at 33J is provided in the supplemental information.

This limits a packaging cushion to a single use. However, visco-elasticty can be used to dissipate energy, provided the frequency content of the stress within the cushion corresponds to a critical damping frequency. We have shown in this paper how the properties of a visco-elastic material can be matched to the design constraints (initial momentum and kinetic energy of the object to be protected) and the thickness of the packaging layer to maximize the energy dissipated. It is possible to establish an almost perfectly plastic collision with a visco-elastic cushion, yet have the material recover fully for further use. Conversely, poor design, in which the frequencies are not matched, could result in a perfectly elastic collision, with no dissipation of energy.

The use of visco-elastic materials for packaging has the further advantage that the design can be tailored to satisfy either the velocity constraint or the acceleration constraint. As a result, it is possible to produce optimal design of packages using visco-elastic materials. In this paper, we have illustrated such a design process for minimizing the thickness of the package.

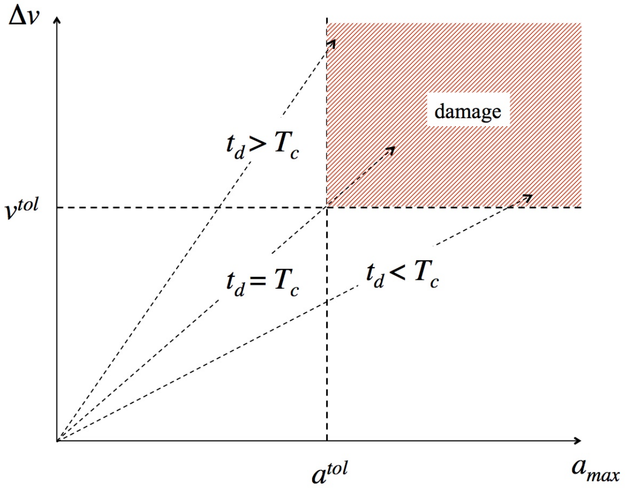

(a)

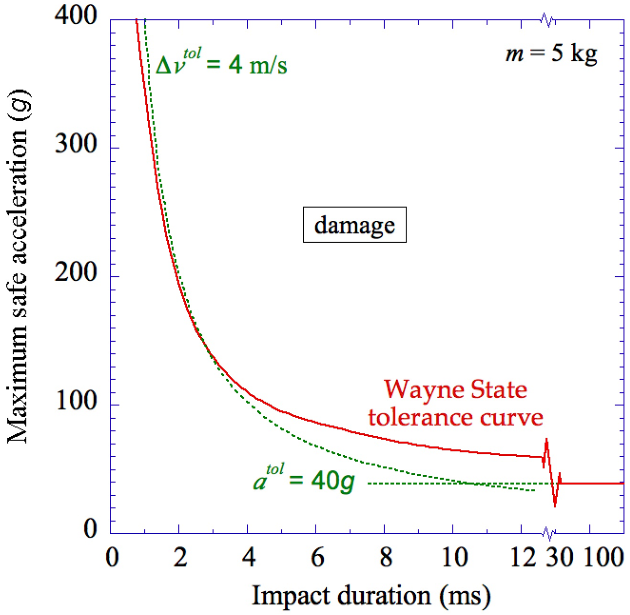

(b)

Figure 2.1: **(a)** An approximate schematic sketch of a map showing how both the critical velocity and critical acceleration criteria must be met for damage to occur. This sketch also shows how the velocity criterion is controlling for short impacts, but the acceleration criterion is controlling for long impacts. **(b)** The Wayne State tolerance curve redrawn from Ref. [39], compared to a critical velocity change of $\Delta v^{tol} = 4$ m/s (assuming a head of mass 5 kg), and a critical acceleration criterion of $a^{tol} = 40g$.

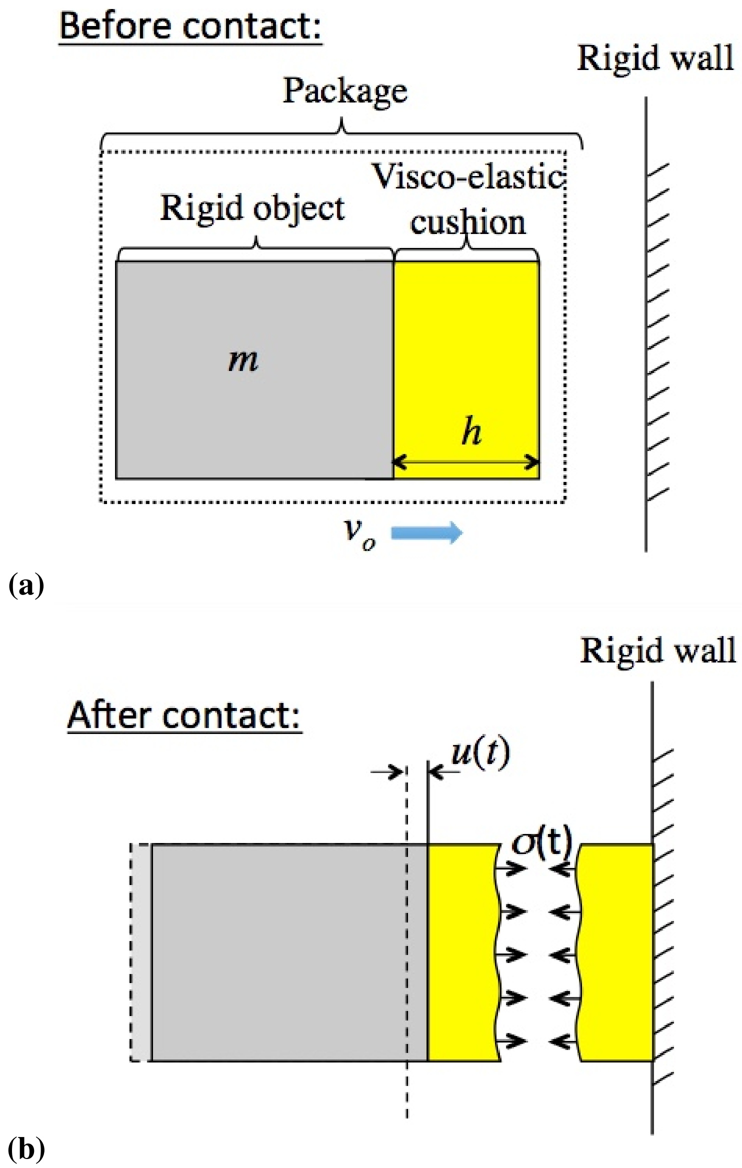

Figure 2.2: An illustration of the model analyzed in this paper. A rigid object of mass m is protected by a visco-elastic cushion of thickness h. **(a)** The package travels towards a rigid wall at an initial speed v_o. **(b)** Upon impact, the visco-elastic cushion deforms by $u(t)$, and generates a corresponding internal stress of $\sigma(t)$.

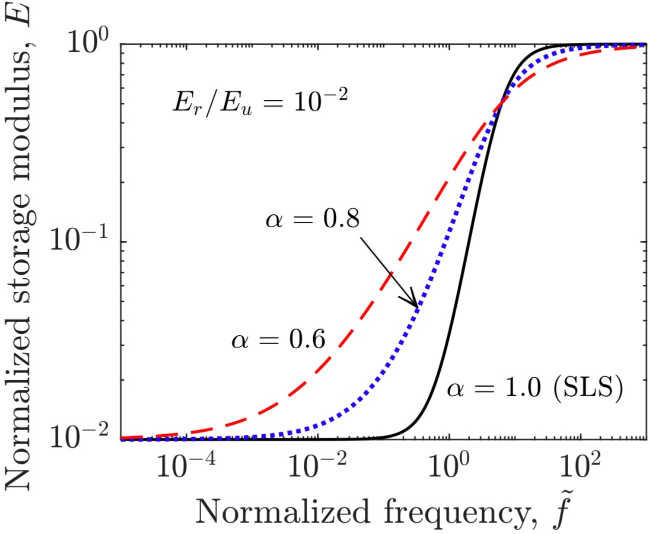

(a)

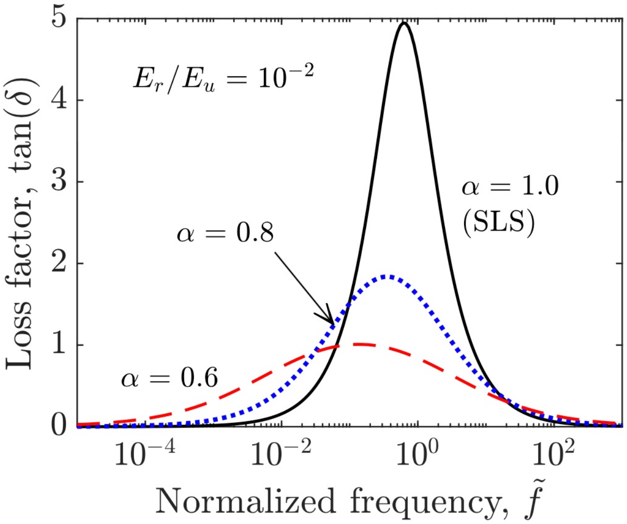

(b)

Figure 2.3: **(a)** Normalized storage modulus, $\tilde{E}' = E'/E_u$, plotted as a function of normalized frequency, $\tilde{f} = f\tau_R$, for different values of α and a ratio of relaxed to unrelaxed modulus of $E_r/E_u = 10^{-2}$. **(b)** Loss factor, $\tan(\delta)$, plotted as a function of normalized frequency, $\tilde{f} = f\tau_R$, for different values of α and a ratio of relaxed to unrelaxed modulus of $E_r/E_u = 10^{-2}$.

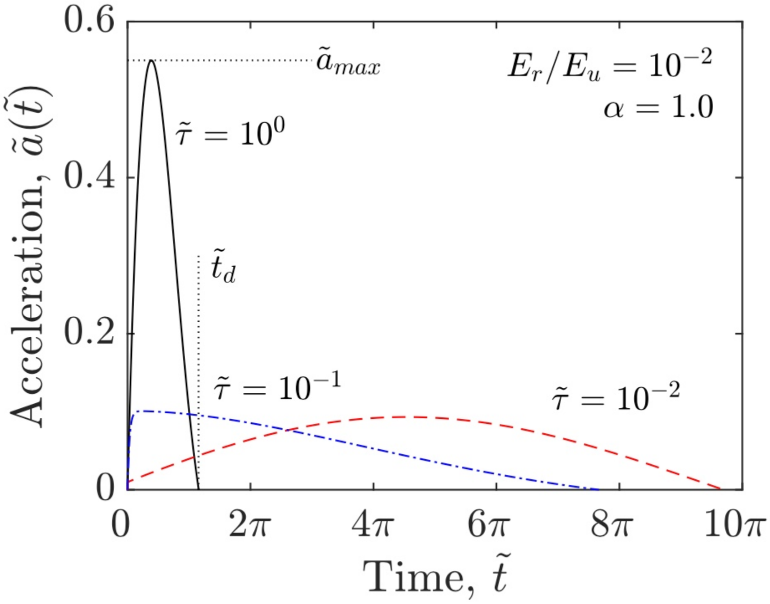

Figure 2.4: Typical examples of how the normalized acceleration, $\tilde{a}(\tilde{\tau}) = [a(t)/v_o][mh/E_u]^{1/2}$ varies with normalized time while the package is in contact with the rigid wall, as shown in Fig. 2.4.

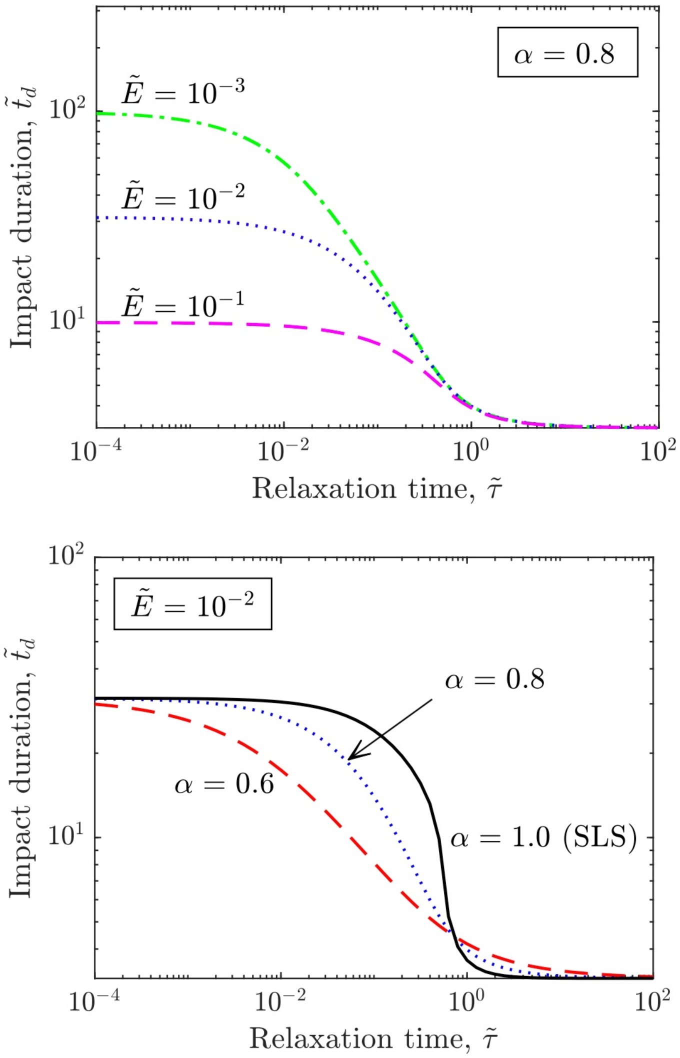

(a)

(b)

Figure 2.5: Normalized impact duration, $\tilde{t}_d = t_d \left(E_u/mh\right)^{1/2}$, plotted as a function of normalized relaxation time, $\tilde{\tau} = \tau_R \left(E_u/mh\right)^{1/2}$, for **(a)** different values of $\tilde{E}$ with $\alpha = 0.8$, and **(b)** different values of α with $\tilde{E} = 10^{-2}$. The transition to a longer duration of impact, associated with a lower value for the maximum acceleration, can be seen with a drop in $\tilde{\tau}$.

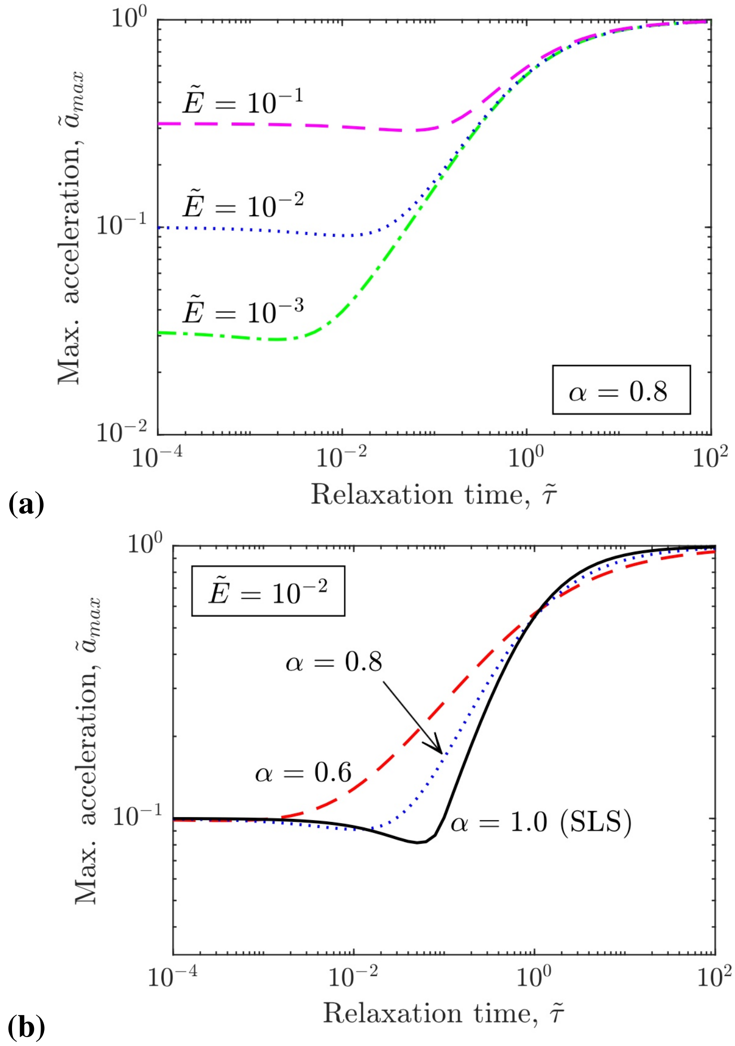

Figure 2.6: Maximum normalized acceleration, $\tilde{a}_{max} = (a_{max}/v_o)\,(mh/E_u)^{1/2}$, plotted as a function of normalized relaxation time, $\tilde{\tau} = \tau_R\,(E_u/mh)^{1/2}$, for **(a)** different values of $\tilde{E}$ with $\alpha = 0.8$, and **(b)** different values of α with $\tilde{E} = 10^{-2}$. The transition to a lower value for the maximum acceleration, associated with a longer impact duration, can be seen with a drop in $\tilde{\tau}$.

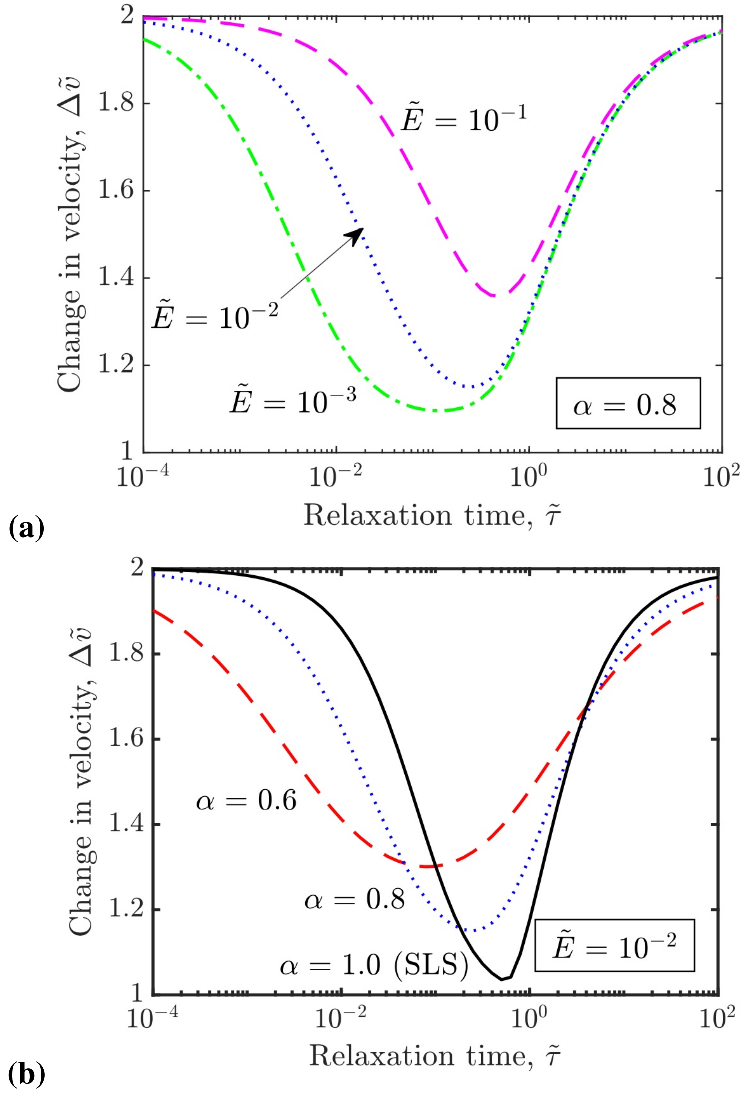

Figure 2.7: Normalized magnitude of the velocity change, $\Delta\tilde{v} = 1 - v_f/v_o$, plotted as a function of normalized relaxation time, $\tilde{\tau} = \tau_R \left(E_u/mh\right)^{1/2}$, for **(a)** different values of $\tilde{E}$ with $\alpha = 0.8$, and **(b)** different values of α with $\tilde{E} = 10^{-2}$. Note that the coefficient of restitution was found to be very close to 0 for $\alpha = 1$ and $\tilde{E} = 10^{-3}$, while it tends to 1 for very small or very large values of $\tilde{\tau}$.

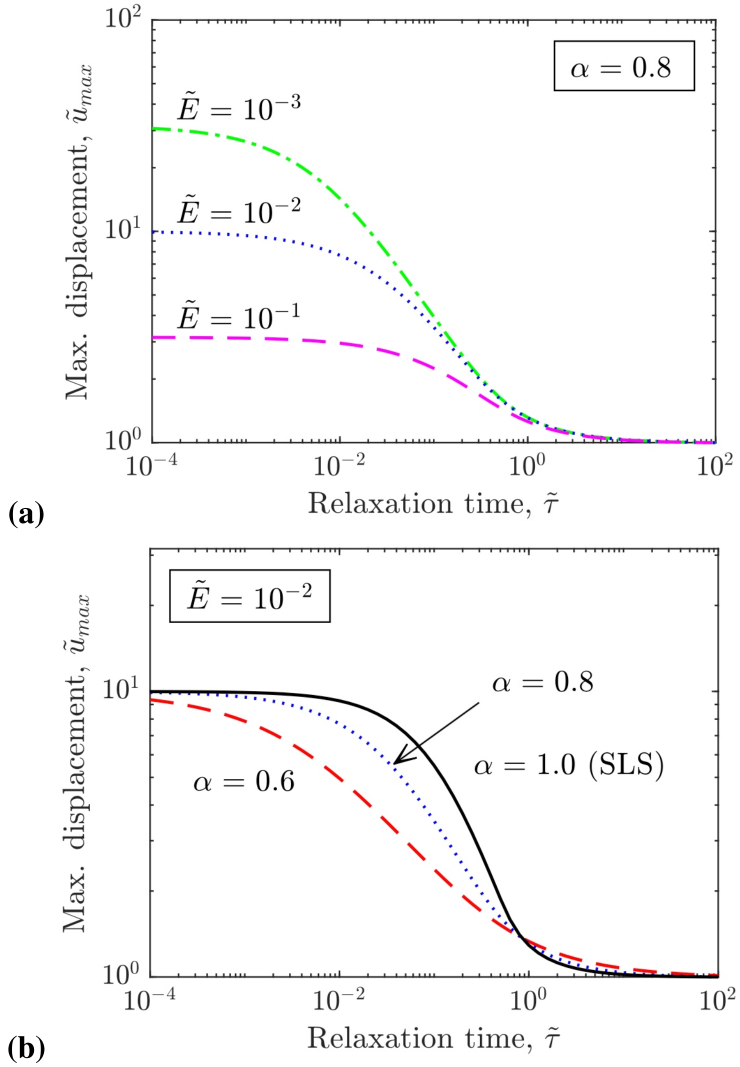

Figure 2.8: Normalized maximum displacement of the cushion, $\tilde{u}_{max} = u_{max}\sqrt{E_u/mv_o^2h}$, plotted as a function of normalized relaxation time, $\tilde{\tau} = \tau_R\left(E_u/mh\right)^{1/2}$, for **(a)** different values of $\tilde{E}$ with $\alpha = 0.8$, and **(b)** different values of α with $\tilde{E} = 10^{-2}$.

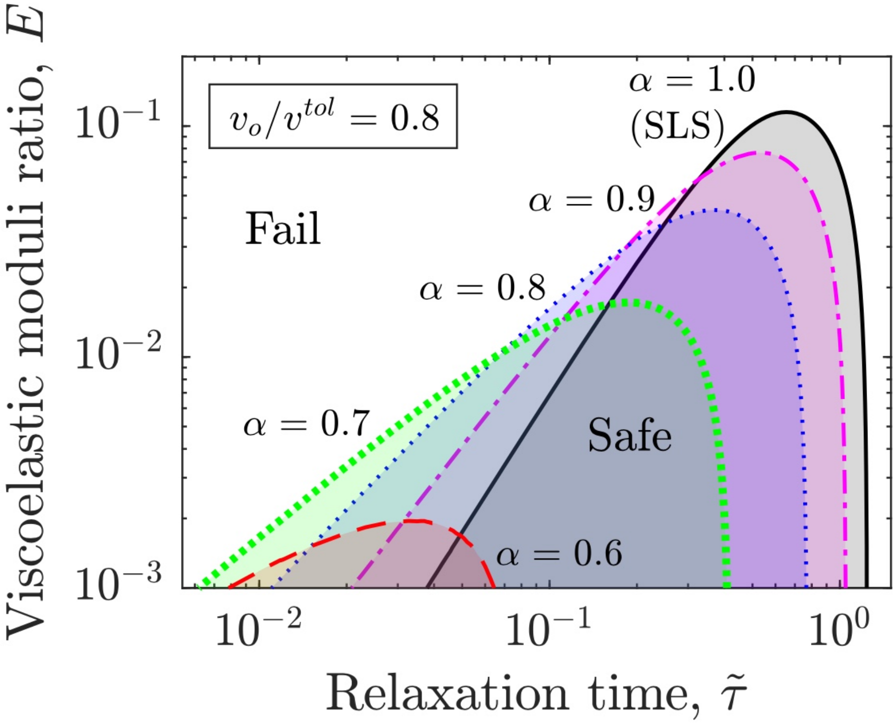

Figure 2.9: Design map showing the regimes in which velocity control can be used to satisfy the velocity criterion for $v_o = 0.8v^{tol}$ for different values of α. The safe design space is beneath each curve. For situations where $v_o < 0.8v^{tol}$, the safe space provides a conservative design.

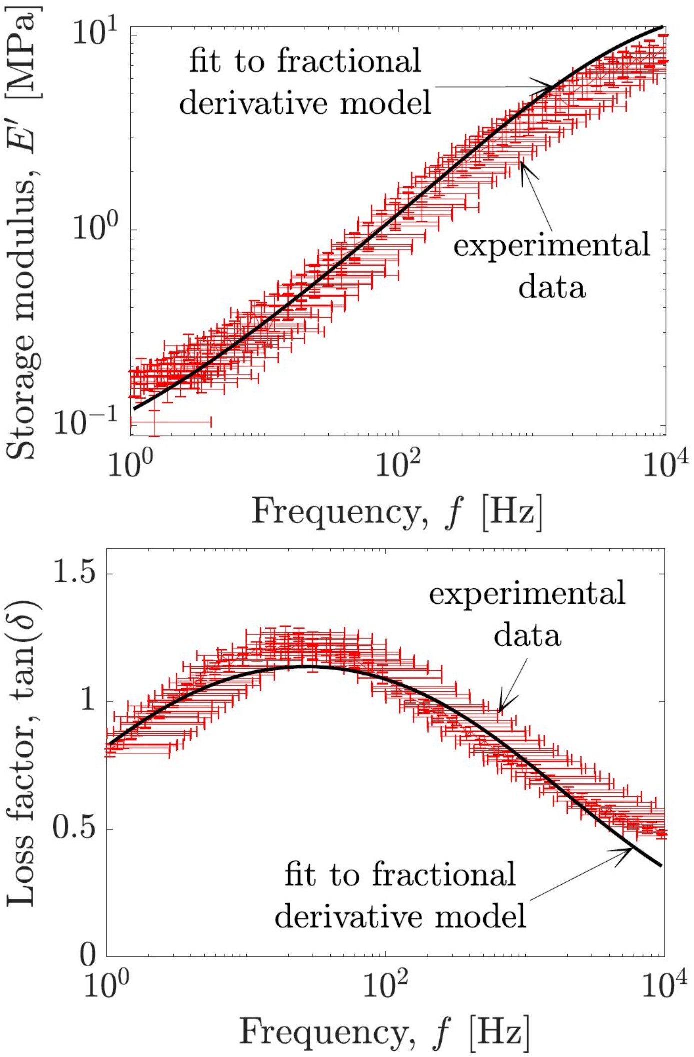

Figure 2.10: The fractional-derivative fit to experimental data for **(a)** the storage modulus, and **(b)** the loss factor for a visco-elastic foam used in a practical implementation of the packaging design. The data have been shifted to a reference temperature of 21 °C.

CHAPTER III

The response of a compliant cylinder to linear acceleration

Introduction

The development of protective helmets is one component of the effort to prevent mild brain injuries in sports. Designing an effective helmet requires both an understanding of which characteristics of the impact cause injury and a strategy to alter those impact characteristics to avoid causing damage. The previous chapter, Chapter II, provides a strategy for reducing the peak acceleration and magnitude of the velocity change during an impact. Therefore, in order to argue that the cushion in Chapter II is capable of providing adequate protection to the head, injury to the human brain must be shown to depend on the extent of these two quantities. The causes of injury can be expressed with kinematic injury criteria, which indicate the type and amount of head motion that cause injury.

The identification of kinematic brain injury criteria is an ongoing area of research, and the next few chapters provide an analysis of the causes of brain deformation that is tailored to the specific goal of demonstrating the efficacy of the cushion in Chapter II, in a head impact scenario. Given the importance of preventing brain injury in automobile and bicycle collisions, these results are situated in a wider research context that stretches back decades and spans a variety of experimental and numerical approaches to identifying the causes of brain injury in closed-head impacts.

It is recognized that the motion of the skull drives deformation within the brain and that delicate objects, like the brain, can be injured by impulsive loading and inertial loading that lead to harmfully high levels of deformation [16]. This is consistent with the theory of bodily injury [23] and also with the discussion of the structural response of an even wider range of non-biological targets [15]. In head injuries, and in some other types of harmful impact and blast loading, either the magnitude of the impulse or force dominates, depending on the ratio of the duration of the loading to the characteristic time of the delicate object. If this ratio is small, then impulse will govern the extent of the deformation within the object; if this ratio is large, then it is the force that will govern the extent of deformation. The underlying mechanics that give rise to these two kinds of response are discussed in greater detail in [23], Section 1.1, and Section 2.1.

In the context of collisions and head impacts, the magnitude of impulse and force can be re-framed as the magnitude of the velocity change and magnitude of the acceleration of the skull. These types of kinematic quantities, both linear and rotational, and their derivatives, are the basis of most kinematic brain injury criteria. Since the motion of the brain itself is obscured, the motion of the skull must be used to estimate the motion of the brain. Examples of kinematic criteria include BRIC, PRHIC, HIC, GSI, KLC, and RVCI, which are described, compared, and evaluated in [10]. Although there is evidence that both rotational and linear motion of the skull can lead to brain injury, the relative importance of rotational and linear components of the head's motion is still uncertain, and the thresholds associated with a given type of motion, such as rotational acceleration in the coronal plane for example, are not well-established. Numerical continuum models can be used to understand this better, but injury criteria developed from numerical simulations alone rely on tissue-level tolerances and material models that are not definitive [6].

In particular, the uncertainty in brain stiffness is known to be problematic since it is recognized that the shear modulus of the brain, which determines its deviatoric deformation response, governs the magnitude of the strain that evolves within the brain during and shortly after an impact [20, 44]. Some finite element models have been validated with pressure and displacement data obtained from impacts to cadaver heads, but there is still a lack of certainty about the stiffness and dissipation of living brain tissue, and the experimental measurements for cadaver brain tissue are not consistent with one another [6]. Recent efforts to measure the visco-elastic constitutive properties of living brain using shear wave elastography are promising, but the results of these studies have yet to be incorporated into commonly used numerical brain models. Among the models currently in use, a range of shear moduli between 100 Pa and 20 kPa are used [42, 44]. This is an extremely wide range, and will lead to vastly different calculations for strain from the same amount of skull motion when a low modulus is used compared to when a relatively high modulus is used.

To address the variation between the constitutive parameters recorded in different experimental investigations, numerical studies have been conducted to probe the influence of different constitutive assumptions on brain deformation metrics, such as local principal strain, and spatial aggregation of strain history maxima (*e.g.* CSDM) [45, 20, 44]. However, none of these studies explicitly considers the influence of brain constitutive properties on the characteristic time of the brain, which is the parameter which governs which kinematic injury criterion is most appropriate for a given impact scenario. Until the constitutive properties of brain tissue are fully quantified and the variation between individuals can be characterized, cautious choices for brain descriptors should be selected. This is to avoid under-predicting the harmfulness of simulated impact events. Using scaling laws that relate dimensionless strain magnitude with brain properties and kinematic descriptors of the impact, a set of cautiously-selected brain properties will be identified in this chapter. The scaling laws presented in this chapter can also be used to determine which material properties and kinematic impact parameters warrant additional study because they heavily influence strain or pressure magnitudes, and which are less critical, because they do not strongly affect these results.

More fundamentally, we will show that the deviatoric response and the volumetric response of the cylinder evolve separately and are governed by different sets of constitutive parameters. The differences in the scaling laws for relating volumetric and deviatoric deformation to skull motion suggest that different mechanisms drive these two different types of response. Specifically, the magnitude of the volumetric response primarily depends on the maximum acceleration of the cylinder and the extent of the deviatoric response depends on the jerk of the cylinder. Relating these kinds of observable kinematic quantities to the amount of shear strain and pressure within the cylinder will enable rapid estimation of the deformation and internal stress due to an impact. Although the simplicity of this model makes it unsuitable for predicting deformation within particular regions in the brain, or as a tool for diagnosing mild traumatic brain injury in a clinical setting, the general conclusions drawn from this analysis can function as guiding principles for the design of deformation-reducing cushions and helmets.

This chapter will consider the development of pressure and strain within brain-like cylinders during linear impacts, specifically. These are impacts which involve only unidirectional translation of the shell that surrounds the cylinder, and involve no rotational motion of this shell. Chapters IV-VI address deformation due to rotational impacts.

3.1 Computational model

3.1.1 Model geometry

The geometry of the human head can be greatly simplified into a two-dimensional cylinder surrounded by an annular shell, as shown in Figure 3.9. The delicate object represents the brain and the shell represents the skull. The compliant cylindrical delicate object is fully attached to the rigid shell, so that the material on the outer radius of the cylinder moves exactly with the interior surface of the rigid shell, in both the normal and circumferential directions. The spatial dimensions of the cylinder are expressed in polar coordinates, with radial coordinate r and circumferential coordinate θ. The circumferential coordinate θ is measured with respect to unit vector parallel to the translation of the cylinder's shell.

The size of the brain is expressed with its radius, R_i, and the brain-like cylindrical object is referred to as the "cylinder" in this chapter and subsequent chapters. In this and subsequent chapters, the radius of the cylinder used to perform calculations is 10 cm, though the dimensionless formulation of the results presented here enable generalizations for cylinders of different sizes.

The plane strain constraint for the axial direction is used in this work, though the plane stress case is also worthy of investigation. The plane strain case was chosen because the brain is enclosed by the skull in all directions. For instance, the lateral sections of the skull and falx will constrain coronal brain motion during motion of the skull in the sagittal plane, and the anterior and posterior sections of the skull will constrain brain motion in the sagittal plane during horizontal motion of the skull. The resistance to large out-of-plane strains caused by the true shape of the skull would be lost in a two-dimensional model that does not confine normal strain in the out-of-plane axis. However, in a real human head, there is is some capacity for normal strain in all three dimensions. Therefore, the plane stress model is still of interest, since it can exhibit tri-axial strain.

3.1.2 Constitutive model for the cylinder

The cylinder has the Standard Linear Solid (SLS) constitutive law for the shear response. The SLS model is defined with an unrelaxed modulus, G_u, a relaxed shear modulus, G_r, and a relaxation time, τ_R^G. The ratio of the unrelaxed to relaxed shear modulus is fixed at the value 5 in this study. Although some constitutive models for the brain use higher or lower ratios, this is within the commonly accepted range [42]. The same is true of the choice of relaxation time for the shear stress relaxation function, which is 0.1 s in this chapter. A further discussion of the influence of relaxation time on the extent of shear strain due to rotational motion is included in Chapters V and VI. For the volumetric response, two different constitutive forms are considered. For the study of the dependence of the pressure on loading pulse duration, a rate independent bulk modulus, K_0, was chosen.

The brain's high bulk modulus is due to the incompressibility of water, which is one of the main components of the brain. For the study of the shear strain, a weakly visco-elastic SLS model was chosen. The parameters that describe this constitutive model are K_u, K_r, and τ_R^K. For the visco-elastic model, the ratio of the unrelaxed to relaxed modulus is 2. This low value is used because the resistance to volumetric change within the brain is thought to be independent of strain rate, but some dissipation was needed to prevent the resonance of high amplitude "whispering gallery" modes. The relaxation time is set to a small value, so that the high frequency modes are preferentially damped. The brain's density is 1040 kg/m^3, which is slightly above that of water. However, in order to keep dimensionless groups in forms that can be expressed with only a few significant figures, the density for the cylinder is rounded down to 1000 kg/m^3 in these calculations.

3.1.3 Linear acceleration of the shell results in linear acceleration of the points on the outer radius of the cylinder

The method of loading in this study is the prescribed acceleration of the shell that encloses the cylinder. Since the outer surface of the cylinder is bonded to the shell, the motion of the shell is replicated by the material on the outer radius of the cylinder. The time-dependence of the acceleration of the shell is prescribed to follow one of two specific functional forms in these simulations. The two types of pulses that are used in this chapter have some similarities and some differences. In both types of pulses, acceleration begins with a period of positive acceleration and ends with a period of negative acceleration. The positive and negative regions of the pulse each cause changes in the velocity of the shell of equal magnitudes, but opposite signs. Therefore, the shell comes to rest after the pulse is complete. The outer radius of the cylinder is then held stationary for the rest of the simulation. The two forms used in this chapter are shown in Figure 3.2. In the shear strain study, a smooth pulse with the form below is used.

$$a(t)/a_{max} = \begin{cases} \xi_1^3(10 - 15\xi_1 + 6\xi_1^2) & 0 < t < t_0/4 \\ 1 - 2(\xi_2^3(10 - 15\xi_2 + 6\xi_2^2)) & t_0/4 < t < 3t_0/4 \\ -1 + \xi_3^3(10 - 15\xi_3 + 6\xi_3^2) & t_0/4 < t < 3t_0/4 \\ 0 & t > t_0 \end{cases}$$

where $\xi_1 = \frac{t}{t_0/4}$, $\xi_2 = \frac{t - t_0/4}{t_0/2}$, and $\xi_3 = \frac{t - 3t_0/4}{t_0/4}$. This form is easily accessed using the "Smooth Step" option for "Amplitude" definition, in Abaqus 2018. The "Smooth Step" option is intended for minimizing the amplitude of high frequency vibrations excited by the rapidly applied forces needed to accomplish rapid changes in acceleration.

For the pressure study, one cycle of a sinusoidal wave is used for the loading pulse. It has some of the same features as the acceleration function for the shear strain study, but introduces some high frequency vibrations that do not affect the pressure field greatly, but do affect the strain fields significantly.

3.1.4 Linearity of strain with the magnitude of prescribed kinematic load

Since the constitutive law for the cylinder is linear, the stress and strain are proportional with the magnitude of the acceleration pulse, provided that the time-dependence (i.e. "shape" and duration) of the loading pulse is held constant. Therefore, when the time-dependence of the loading pulse is held constant, increasing one kinematic quantity, such as acceleration, by some factor will also increase the velocity, displacement, and jerk by the same factor. In this situation, which quantity truly governs the amount of strain or stress cannot be known, since it is impossible to separate an increase in one kinematic quantity from an increase in another. If the real cause of increased deformation is, for instance, increased acceleration but not increased jerk, that cannot be determined if acceleration cannot be varied independently from jerk. Therefore, the time-dependence of the pulse must be varied in order to identify the kinematic quantity (e.g. jerk, acceleration, velocity, displacement) that causes the stress and strain magnitudes to be of the observed value. By varying the pulse duration, pulses with the same values for some kinematic quantities but different values for other kinematic quantities can be compared, and the kinematic quantities which correlate with stress and strain for a range of impact durations can be identified. In this study, the acceleration is chosen as the default kinematic quantity for expressing the size of the loading pulse, but each impact with a known a_{max} and t_0 can be characterized with its maximum velocity, displacement, or jerk. For the acceleration formula for the shear strain study, the corresponding values for maximum speed, distance, and jerk are given below:

$$u_{max} = 0.134\, t_0^2\, a_{max} \tag{3.1}$$

$$v_{max} = 0.297\, t_0\, a_{max} \tag{3.2}$$

$$j_{max} = 7.50\, t_0^{-1}\, a_{max} \tag{3.3}$$

Modeling the brain with linear materials is a significant simplification of the actual mechanical properties of the brain, since the brain is known to have a nonlinear response at high levels of deformation. Nevertheless, limiting this analysis to linear material models makes the creation of approximate comparisons between different levels of loading much simpler. Rather than needing to perform calculations for many loading levels with the same time-dependence, one simulation is sufficient. The results of a single simulation can be non-dimensionalized, in order to determine relative increases in deformation and internal stress for different levels of kinematic loading.

3.1.5 Dimensional Analysis

One of the benefits of a simple model is that it can be non-dimensionalized easily, and the relationships between dimensionless groups can be used to understand the fundamental properties of the system. In this chapter, the Buckingham π theorem is used to generate the dimensionless groups relevant to the problem. We assume that there are eleven physically meaningful variables in the pressure study and thirteen in the strain study. Nine of these variables are the same, in both. They are: R_i, ρ, G_u, G_r, τ_R^G, t_0, a_{max}, x, and y. In the pressure study, the tenth and eleventh variable are maximum pressure, p_{max}, and the bulk modulus, K_0. In the shear strain study, the additional variables are ε_{max}, and the parameters for the volumetric visco-elastic response, K_u, K_r, and τ_R^K. The dimensionless groups for the pressure study are: G_u/K_0, G_r/G_u, $\tilde{t}_K = t_0\sqrt{K_0/\rho}/R_i$, $\tau_R^G\sqrt{G_u/\rho}/R_i$, x/R_i, y/R_i, and $\tilde{p}_{max} = p_{max}/a_{max}\rho R_i$. Only seven dimensionless groups are needed because the response p_{max} is linear with a_{max}. Similarly, there are only nine groups necessary for the shear strain study. They are G_r/G_u,K_u/G_u, K_r/K_u, $\tilde{t}_0 = t_0\sqrt{G_u/\rho}/R_i$, $\tau_R^G\sqrt{G_u/\rho}/R_i$, $\tau_R^K\sqrt{K_u/\rho}/R_i$, x/R_i, y/R_i, and $\tilde{\varepsilon}_{max} = \varepsilon_{max}K_u t_0 G_u^{1/2}/(a_{max}\rho^{3/2}R_i^2)$. Although it is not essential, the dimensionless quantity $\frac{G_u}{a_{max}\rho R_i}$ is helpful in generating the dimensionless strain group, and it would be necessary if it was not already known that the strain is linear with acceleration when all other parameters are held constant.

3.2 Results

Linear acceleration pulses initiate a few different kinds of transient stress waves. Some of the waves that are created by the motion of the shell involve deformation and propagation behaviors that are similar to those of dilatational and shear plane waves. Dilatational waves are tensile and compressive waves with volumetric change. The particle motion of a dilatational wave is parallel to the direction of propagation. Shear waves have particle motion orthogonal to the direction of propagation. The behavior of the transient waves in the cylinder that are similar to dilatational waves is primarily governed by the bulk modulus, and the behavior of the shear waves depends on both the bulk modulus and shear response.

The large bulk modulus of the brain limits the amount of volumetric strain that can occur during an impact, so Mohr's circle for strain is centered near zero. Therefore, the absolute values of both the principal strains, ε_1 and ε_2, are approximately equal to the maximum shear strain, ε_s. The maximum value of shear strain, then, is enough to approximate the maximum of the absolute values of the two principal strains, too. In contrast, the pressure serves as an approximation of the maximum of the absolute values of the principal stress. Since the shear modulus is quite small, the material responds to even large shear strains with relatively small shear stresses. In this situation involving a large bulk modulus and a small shear modulus, the maximum principal stress is approximately equal to the absolute value of the pressure. This is because the radius of Mohr's circle for stress is relatively small compared to the σ-coordinate of its center. Since shear strain also approximates principal strain magnitudes, and pressure approximates principal stress magnitudes, only the dependence of maximum shear strain and pressure on kinematic impact variables are considered in this chapter.

3.2.1 Pressure

The pressure at a given time within the cylinder depends mainly on the acceleration of the shell, at that instant. That is because, after the transient waves have died out, the unidirectional, linear acceleration of the shell produces internal loads that are equivalent to an elasto-static problem with a constant body force in one direction.

Figure 3.3 shows a contour plot of the dimensionless pressure, $p(x, y, t)/a(t)\rho R_i$, within the cylinder during the application of the acceleration pulse. The magnitude of the pressure at each point is proportional with the acceleration at that instant in time, and the spatial distribution within the cylinder remains the same, regardless of the acceleration magnitude. This trend holds across the four values of G_u/K_0 that were considered in this study, for which the dimensionless parameter $\tilde{t}_K = t_0\sqrt{K_0/\rho}/R_i$ is chosen to be larger than 20. Only one value of G_r/G_u and one value of $\tau_R\sqrt{G_u/\rho}/R_i$ were used in this analysis, but it is unlikely that the visco-elastic proprties of the deviatoric response affect the pressure because the pressure is associated with the volumetric response.

Figure 3.4 shows the dependence of the maximum dimensionless pressure as a function of a dimensionless acceleration pulse duration, $\tilde{t}_K$. This is a different dimensionless time than the one that is used throughout the rest of this chapter and in later chapters, which is $\tilde{t}_0 = t_0\sqrt{G_u/\rho}/R_i$. The pressure is made non-dimensional by dividing by the quantity $a_{max}\rho R_i$, as stated in Section 3.1.5. For large values of $\tilde{t}_K$, independent of K_0/G_u, the maximum dimensionless pressure approaches the limit of 1. The existence of this limit, and its physical meaning, are discussed in the next section.

3.2.1.1 Discussion

The quantity $a_{max}\rho R_i$ is the maximum pressure that would be attained in a one-dimensional object, such as a rod, that is adhered at each end to a pair of rigid bodies that maintain a fixed distance from each other, and are subjected to an identical acceleration pulse, $a(t)$. This is the one-dimensional analog to the two dimensional cylinder being enclosed within a rigid shell that experienced a prescribed acceleration. The expression for the pressure in the one-dimensional scenario is explained below.

The equilibrium equation in one dimension with no body forces is

$$\frac{\partial \sigma}{\partial x} = \rho a. \tag{3.4}$$

Placing the origin at the center of the body, the stress field will be anti-symmetric in x. Therefore the stress field will be

$$\sigma(x) = \rho a x \tag{3.5}$$

and the maximum stress will be located at one end of the object, at $x = R_i$, and have the value $\sigma_{max} = a_{max}\rho R_i$.

In the analysis of the cylinder, the acceleration pulse duration, t_0, is non-dimensionalized by dividing by the quantity $R_i\sqrt{\rho/K_0}$. This represents the approximate time it takes a P-wave to travel the distance from the outer radius of the cylinder to its center, which functions as a characteristic time for the propagation of this type of wave within the cylinder. Although a P-wave travels with the speed $\sqrt{M/\rho}$, where M is the P-wave modulus, $\sqrt{K_0/\rho}$ is an acceptable approximation of this speed when the ratio of the shear modulus, G, is very low compared to the bulk modulus, K.

For cylinders with different K_0/G_u ratios that are sufficiently large, the response to a linear acceleration pulse is approximately the same, when considered using dimensionless parameters. This is evident in the overlap of the curves for various G_u/K_0 ratios. In the region between $\tilde{t}_K = 40$ and $\tilde{t}_K = 130$, the curves for all four G_u/K_0 ratios overlap. As long as $\tilde{t}_K$ is larger than 40, the maximum pressure within the cylinder is proportional to the maximum acceleration of the cylinder's outer radius. This holds regardless of the exact value of the pulse duration, provided it is sufficiently long. However, for $\tilde{t}_K$ values less than 40, the maximum pressure can be larger than the long-pulse limit, and the relationship between pressure and acceleration depends on the pulse duration. We can see from this plot that non-dimensionalizing the pulse duration, which converts between t_0 and $\tilde{t}_K$, collapses the dimensionless maximum pressure curves for multiple G_u/K_u ratios onto one curve. That suggests that $R_i\sqrt{\rho/K_0}$ is the characteristic time associated with the temporal evolution of the maximum pressure value.

In the context of head injury, the properties of the brain can be substituted into these dimensionless relationships to determine whether the brain's pressure is proportional with acceleration, magnitude of the velocity change, or a different kinematic parameter.

This type of analysis is detailed here. First, we must confirm that we can use the dimensionless maximum pressure results in Figure 3.4, which were obtained for different values of K_u/G_u, (*e.g.* 3.33×10^4 and 3.33×10^5). Since the results are the same for these two values, we assume that if the K_0/G_u-value of the brain is within this range, then the dimensionless pressure results will be equally applicable. The shear modulus of the human brain is on the order of 10 kPa or lower, and the bulk modulus is on the order of the effective bulk modulus of water, which is 2.19 GPa. Therefore, the K_0/G_u ratio of the human brain is at least 2.19×10^5, and falls within an acceptable range for using the results in Figure 3.4.

Next, we consider two representative head impacts and calculate approximate maximum pressures for them. The $\tilde{t}_K$-value for a 10 ms pulse applied to a head with a radius of 10 cm is 148, which is in the range where the maximum pressure depends exclusively on the maximum acceleration, the density of the brain, and its radius. 10 ms is approximately the average duration of head impacts recorded in football practices and games [7]. A lower bound for the applicability of this simple correlation can also be attained with these curves. A $\tilde{t}_K$-value of 40 corresponds to a pulse duration of 3.7 ms. It can be seen in Figure 2 of [17], that sports-related collisions are significantly longer than 3.7 ms, and most falls are generally not very much shorter than this duration. Therefore, the maximum pressure during any head impact that can lead to injury is expected to be proportional with the maximum acceleration of the skull, and independent of the impact's duration, because these impacts are longer than the characteristic time of the brain in this loading arrangement. For brain injuries due to dangerously high levels of pressure within the brain, we expect that an injury criterion based on a threshold of the maximum acceleration of the skull will be most effective in classifying injury risk.

3.2.2 Shear strain

Numerous studies have shown that excessive deformation of brain tissue can lead to injury [6]. Although the most common measures of deformation are based on maximum principal strain, the maximum shear strain is an acceptable alternative for classifying the extent of deformation, since it generally coincides with the maximum principal strain, when the bulk modulus of the material is much larger than the shear modulus. Further, shear strain provides a complementary view of the internal dynamics of the brain, when paired with pressure. This is because pressure is associated with volumetric deformation and the shear strain is associated with deviatoric strain. Using both pressure and shear strain, we are able to gather a broad view of the response of the brain during and shortly after an impact.

Although strain is already a dimensionless quantity, defining a "dimensionless strain" facilitates the scaling law analysis in this section, which is later used to estimate the magnitude of strain during linear impacts. Strain can be written in a dimensionless form with the expression

$$\tilde{\varepsilon} = \varepsilon \frac{K_u}{a\rho R_i} \frac{t_0\sqrt{G_u}}{R_i\sqrt{\rho}}. \tag{3.6}$$

The definition in Equation 3.6 incorporates the other known dimensionless parameters $G_u/a_{max}\rho R_i$, $\tilde{t}_0$, and K_u/G_u. In Section 3.2.2.5, the motivation for using this formula for the dimensionless shear strain is explored.

3.2.2.1 Shear wave propagation

Figure 3.5 depicts how the shear strain, at a range of positions, changes over time, as a propagating strain pulse travels away from the outer radius of the cylinder, where it was initiated. This transient deformation disturbance has many of the properties of a shear plane wave. The shear strain at four different times, that are separated by the time period Δt, is plotted here as a function of position along the vertical line $x = 0$, which passes through the center of the cylinder and extends out to the outer radius of the cylinder. In these plots, it is shown that a transient wave is generated at the outer radius of the cylinder, at $\tilde{r} = 1$, and it propagates inward at approximately the speed $v_u = \sqrt{G_u/\rho}$. The dimensionless distance, $\Delta\tilde{r}$, that a wave with the speed v_u would travel in the time between plotted instants, Δt, is marked on this figure. A dimensionless version of Δt, with the form $\Delta\tilde{t} = \Delta t\sqrt{G_u/\rho}/R_i$, is the same as the dimensionless distance $\Delta\tilde{r}$. That the dimensionless quantity $\Delta\tilde{r}$, which is based on an idealized wave speed of v_u, correlates with the actual dimensionless distance that the wave travels in this simulation, suggests that the strain disturbance studied here travels with a speed near to the idealized unrelaxed wave speed v_u. Since the particle motion for this disturbance is also orthogonal to the direction of propagation, the behavior of this transient disturbance is very similar to that of a plane shear wave. This similarity provides support for analyzing the shear strain due to this propagating disturbance with concepts from the analysis of plane shear waves.

3.2.2.2 Definition of dimensionless maximum shear strain, $\tilde{\varepsilon}_{max}$

The dimensionless maximum shear strain, $\tilde{\varepsilon}_{max}(x, y)$, is of interest because it is a useful measure of the extent of deviatoric deformation that has occurred. This dimensionless quantity, and all other strain-based dimensionless quantities covered in this section, is obtained from the corresponding strain using the scheme in Equation 3.6. The spatial distribution of this value can be examined to see which regions experience the most severe deformation. In this chapter, the quantity $\tilde{\varepsilon}_{max}$ refers to the dimensionless form of the temporal maximum of the maximum shear strain at a given location, (x, y). This section describes how this value is obtained from the strain tensor, which varies in time and space.

The quantity, $\tilde{\varepsilon}_{max}(x, y)$, is obtained from the dimensionless instantaneous maximum shear strain for each instant, referred to here as $\tilde{\varepsilon}_s(x, y, t)$. $\tilde{\varepsilon}_s$ is the dimensionless time-varying maximum shear strain in the context of Mohr's circle. That is, it is the dimensionless form of the maximum value of the shear strain that can be attained by changing the basis vectors that the strain tensor is expressed in. In Figure 3.5, the magnitude of the dimensionless shear strain in the (x-y) coordinate system, $|\tilde{\varepsilon}_{xy}|$, coincides with $\tilde{\varepsilon}_s$, at some locations. These locations are the points which lie on the vertical line that passes through the center of the cylinder, where $x = x_0 = 0$ m. However, this is not true for all positions within the cylinder, so it is necessary to calculate the dimensionless maximum shear strain at each position, using the dimensionless form of the full strain tensor.

Figure 3.6 shows an example of the progression from $\tilde{\varepsilon}_{xy}(x_0, y, t)$ to $\tilde{\varepsilon}^*_{max}(x_0, y, t)$ for the strain at a range of positions. Since the leading edge of the strain pulse has reached $y/R_i = 0.76$, we can see that the maximum shear strain that a point has experienced prior to time t, known as $\tilde{\varepsilon}^*_{max}(t)$, increases when higher-magnitude sections of the strain disturbance passes by. When the impact is complete and all the waves within the cylinder have dissipated, then $\tilde{\varepsilon}^*_{max}(\infty)$ will give the value for the dimensionless maximum shear strain for the whole impact, $\tilde{\varepsilon}_{max}$.

3.2.2.3 Dependence of $\tilde{\varepsilon}_{max}$ on the cylinder bulk modulus to shear modulus ratio, K_u/G_u

Having defined $\tilde{\varepsilon}_{max}$, we consider its dependence on the constitutive properties of the cylinder, on the location of interest within the cylinder, and on the duration of the linear acceleration pulse that caused the deformation. Figure 3.7 shows the dimensionless maximum shear strain along the vertical line passing through the center of the cylinder, $\tilde{\varepsilon}_{max}(x_0, y)$, for acceleration pulses with three different dimensionless durations, $\tilde{t}_0$, and ratios of K_u/G_u. The spatial distribution of the dimensionless maximum shear strain, $\tilde{\varepsilon}_{max}$, depends strongly on the dimensionless duration of the pulse, $\tilde{t}_0$, but only very weakly on the ratio of bulk to shear modulus, K_u/G_u. The weak dependence of dimensionless maximum shear strain on this ratio can be observed from the overlapping of the maximum shear strain curves for different K_u/G_u values in each subplot, a-c. For example, in Figure 3.7b, for which $\tilde{t}_0 = \sqrt{6} \times 10^{-0.5}$, all three curves, each with a different K_u/G_u value, have maximum dimensionless strain values within 10% of one another, and have their spatial maxima at the same location. In the other two subplots, which have different dimensionless durations, the curves for different G_u/K_u-values are also similar to each other, and nearly overlap.

Further evidence of the lack of dependence of the dimensionless maximum shear strain $\tilde{\varepsilon}_{max}$ on the ratio K_u/G_u is found in Figures 3.8a-c and 3.9a-c. These depict the dimensionless maximum shear strain as a function of position within the cylinder, the dimensionless loading pulse duration, and the ratio K_u/G_u for a variety of cylinder constitutive property selections. The maximum strain experienced by the material at five different positions is reported. These five positions are evenly distributed along the vertical line extending from the middle of the cylinder up to its outer boundary, at $y = R_i$. This is the same line from which the results in Figure 3.7 were drawn. (Strain at $y/R_i = 0$ is not reported because it approaches zero.)

Figure 3.8a gives the dependence of $\tilde{\varepsilon}_{max}$ on the ratio of K_u to G_u for relatively short pulses, which have dimensionless duration $\tilde{t}_0 = \sqrt{6} \times 10^{-1}$. For a cylinder with unrelaxed shear modulus $G_u = 6$ kPa, density $\rho = 1000$ kg/m^3, and internal radius 10 cm, this dimensionless pulse duration is associated with pulses that are 10 ms long. Figures 3.8b and 3.8c are associated with longer pulses, with dimensionless durations $\tilde{t}_0 = \sqrt{6} \times 10^{-0.5}$ and $\tilde{t}_0 = \sqrt{6}$. For the results in this figure, all simulations have the same values for the remaining dimensionless parameters: $G_u/G_r = 5$, $K_u/K_r = 2$, $\tau_R^G \sqrt{G_u/\rho}/R_i = \sqrt{6}$ and $\tau_R^K \sqrt{K_u/\rho}/R_i = 0.16$. For the shortest impact duration considered here, shown in Figure 3.8a, there is a slight dependence of $\tilde{\varepsilon}_{max}$ on K_u/G_u, with decreasing $\tilde{\varepsilon}_{max}$ associated with increasing K_u/G_u. However, above approximately $K_u/G_u = 5 \times 10^4$, the resolution the in $\tilde{\varepsilon}_{max}$ dependence is not large enough to see the details of the relationship between $\tilde{\varepsilon}_{max}$ and K_u/G_u. For the other two durations considered, there is relatively little dependence of the dimensionless shear strain on the ratio of bulk modulus to shear modulus, in the sense that any K_u/G_u ratio between 1.05×10^4 and 1.05×10^5 results in approximately the same value of $\tilde{\varepsilon}_{max}$ at each position.

3.2.2.4 Dependence of $\tilde{\varepsilon}_{max}$ on the dimensionless acceleration pulse duration, $\tilde{t}_0$

As with the ratio K_u/G_u, the dependence of $\tilde{\varepsilon}_{max}$ on dimensionless relaxation time, $\tilde{t}_0$ is not large for the five positions considered in Figures 3.8 and 3.9. Specifically, over a range of pulse durations that span an order of magnitude (*i.e.* a factor of 10), the greatest variation between $\tilde{\varepsilon}_{max}$-values is less than a factor of 4 for the innermost position ($r/R_i = 0.2$), and less than a factor of 2 for the other positions that were considered ($/R_i = 0.4, 0.6, 0.8,$ and 1.0). Further, the magnitude of the dimensionless maximum strain stays between the values 6 and 1.5 for all five positions, r/R_i, and across the full range of dimensionless pulse durations, $\tilde{t}_0$.

However, Figure 3.9 considers only five points, all with $r/R_i \geq 0.2$. Within the range of dimensionless values studied here, the spatial maximum of $\tilde{\varepsilon}_{max}$ along the vertical line $x = 0$ is usually attained at a point within $r/R_i < 0.2$. Figure 3.10a contains a plot of the maximum shear strain within the cylinder as a function of loading pulse duration for the vertical line, $x = 0$, and the horizontal line (and $y = 0$) that each pass through the center of the cylinder. Figure 3.10b has the radial coordinate of the point where the maximum shear strain is attained plotted against dimensionless pulse duration. The increasing maximum shear strain seen for decreasing dimensionless pulse duration is associated with the position where that maximum is attained, $\tilde{r}^*$, being smaller, and therefore closer to the center. This relationship holds for all ratios of K_u to G_u that were considered.

3.2.2.5 Discussion: Calculation of an upper bound for shear strain in linear impacts

The definition for the maximum dimensionless shear strain in Equation 3.6 is chosen in order to normalize the magnitude of the strain with the severity of the acceleration pulse and the constitutive parameters of the cylinder. The dimensionless quantity $\tilde{\varepsilon}_{max}$, referred to as the dimensionless maximum shear strain, is a function of G_u/K_u, $\tilde{t}_0$, G_r/G_u, K_r/K_u, $\tilde{t}_K = t_0\sqrt{K_0/\rho}/R_i$, and $\tau_R^G\sqrt{G_u/\rho}/R_i$, as well as the dimensionless position variables $\tilde{x} = x/R_i$ and $\tilde{y} = y/R_i$. In the previous section, the dependence of $\tilde{\varepsilon}_{max}$ on K_u/G_u and $\tilde{t}_0$ was explored in detail. The other dimensionless parameters, $\tilde{t}_K = t_0\sqrt{K_0/\rho}/R_i$, and $\tau_R^G\sqrt{G_u/\rho}/R_i$, are not the focus of this study, and are fixed to values that are consistent with, and representative of, the properties of the human brain.

The definition for the maximum dimensionless shear strain in Equation 3.6 can be rearranged into the expression

$$\varepsilon = \tilde{\varepsilon}_{max}\frac{a_{max}}{t_0}\frac{\rho R_i^2}{K_u}\frac{\sqrt{\rho}}{\sqrt{G_u}}, \tag{3.7}$$

where $\tilde{\varepsilon}_{max}$ acts as a coefficient that depends weakly on G_u/K_u and $\tilde{t}_0$, and which relates known variables to an estimate of strain. The dimensionless position parameter r/R_i must also be sufficiently large, approximately $r/R_i > 0.2$ in the case shown here, for $\tilde{\varepsilon}_{max}$ to remain within a small band of values across a range of G_u/K_u and $\tilde{t}_0$ values. For $r/R_i < 0.2$, the shear strain is noticeably higher, in the case of the most rapid pulses, or lower, in the case of longer pulses, than in the rest of the cylinder. Higher strain values at the center of the cylinder, that are observed especially in the shortest acceleration pulse scenarios, are due to the stress wave being focused at the center of the cylinder. The lack of radial symmetry and material homogeneity of a human brain may prevent the evolution of these relatively high strains, because waves initiated at the interface between the shell and the cylinder will not arrive at the same radial location coordinate within the interior simultaneously, and can be scattered by internal interfaces between sections of the brain. Additional high frequency damping would also likely suppress the magnitude of these peaks. The region that experiences these high levels of strain is also relatively small.

An upper bound for shear strain can be obtained with the results from this section and cautious choices for unknown parameters, like the bulk and shear moduli, using Equation 3.7. From Figure 3.8d and 3.9d, it can be seen that the maximum $\tilde{\varepsilon}_{max}$ is 15 for accelerations pulses in the range relevant to sport impacts. The bulk modulus of the brain is approximately 2.19 GPa, the density of the brain is 1040 kg/m^3, and the radius of the brain of an adult human is on the order of 10 cm. 1 kPa is a fairly cautious estimate for the unrelaxed modulus of human brain. For the sake of seeking an upper bound on ε_{max}, this is an appropriate choice, though the true unrelaxed shear modulus of the brain is likely higher. Assuming a hypothetical impact lasting 15 ms, with a maximum linear acceleration of 1000 m/s^2 and no rotation of the skull, the upper bound of strain is expected to be on the order of 0.005 or less. This is well below most strain-based tissue damage criteria, which are most often on the order of 0.05 to 0.5. Therefore, the linear component of skull motion is expected to make a relatively modest contribution to shear strain within the brain.

3.3 Conclusions

For the simplified geometry considered in this chapter, the pressure at all points within the cylinder is proportional with the linear acceleration of the cylinder's outer radius, when the dimensionless duration of the pulse is more than roughly 40. The pressure is proportional with the acceleration in all these impacts because the pressure within the whole cylinder reaches its steady-state behavior quickly, compared to the pulse duration, so the spatial variation in pressure remains the same, up to a multiplying magnitude coefficient, regardless of duration of the pulse. The magnitude of this steady-state field at any given time depends entirely on density, bulk modulus, and the current acceleration value. Substituting in the parameters for the human head, the dimensionless duration of 40, above which pressure is dependent only on acceleration and is independent of duration, corresponds to approximately 3.7 ms. Since nearly all head impacts involving a helmet, and many of those lacking head protection, last longer than 3.7 ms, it can be concluded that acceleration should be the underling kinematic variable for kinematic injury criteria for focal brain injuries that are thought to be caused by dangerously high pressures.

The deviatoric part of the deformation due to the linear acceleration of the shell surrounding the cylinder is more complicated, and so the development of a kinematic injury criterion for diffuse brain injuries caused by large deviatoric deformations within the brain is also not simple. Although the lumped-parameter model of [23] suggests that strain from short loading pulses will be proportional with the magnitude of the velocity change of the shell, that sort of behavior was not observed in these simulations. Instead, when acceleration pulses with a range of durations are applied to the shell, it was seen that the maximum shear strain in the interior of the cylinder is roughly proportional with the ratio of the shell's acceleration magnitude to the pulse duration, a_{max}/t_0. This ratio is proportional with the maximum value of the jerk of the shell. Therefore, it is proposed that the shear strain is proportional with this kinematic quantity, rather than the magnitude of the shell's maximum acceleration or velocity change.

The proportionality between maximum shear strain and the maximum jerk of the shell is due to the development of a transient wave with a lateral displacement magnitude that is proportional to the acceleration of the shell. The shear strain of the transient wave initiated during the pulse is roughly proportional with the magnitude of the particle velocity at each material point that is on the vertical line passing through the center of the cylinder. Further, the shear strain is also roughly inversely proportional with the speed of an infinite-frequency shear wave, $v_u = \sqrt{G_u/\rho}$, for the region close to the outer radius of the cylinder. This is analogous to what occurs in a plane wave, where the magnitude of the shear strain is proportional with the magnitude of the lateral particle velocity and inversely proportional with the speed $\sqrt{G_u \rho}$. This commonality between an idealized plane wave and the transient wave in the cylinder suggests that the shear strain within the cylinder is due to the lateral motion of the top and bottom of the cylinder's outer radius driving a shear wave. This shear wave is superposed onto the lateral motion of the whole brain, which is mostly brought on by rapidly-traveling longitudinal waves. The lateral displacement that is associated with the shear wave has a magnitude which is proportional with the acceleration of the shell, so its particle velocity magnitude is therefore proportional with the jerk of the shell. The strain due to this slow-moving wave is also approximately proportional to the quantity $R_i^2 \rho / K_u$. This quantity is of the same order as the square of the time it would take an elastic P-wave to travel the distance of the radius of the cylinder, $R_i \sqrt{M/\rho}$. In that way, the bulk modulus of the cylinder medium influences the magnitude of shear strain.

In this chapter, scaling laws involving dimensionless quantities were paired with cautious approximations for other brain parameters, in order to draw conclusions about kinematic causes of tissue level deformation within the brain. First, it was shown that pressure within the brain in neatly correlated with acceleration. Then, an upper bound for the strain within the brain during a typical head impact in football was identified and found to be on the order of 0.005, which is much less than most published injury thresholds for brain tissue. Therefore, the development of kinematic head injury criteria for linear head impacts should focus mainly on characterizing acceleration thresholds, because that is the quantity which provides the best correlation with pressure.

The magnitude of the velocity change of the skull need not be studied in greater detail, since it was shown that the magnitude of the velocity change is not directly correlated to increasing strain or pressure, since those two quantities correlate best with jerk and acceleration, respectively. Although the jerk of the skull is correlated with the shear strain magnitude, and the potential risks associated with exceedingly short impacts should not be completely ignored, it was shown that the magnitude of the shear strain will remain small in purely linear impacts with acceleration magnitudes and durations like those that currently occur in contact sports. This is because the existing cushioning strategies, which give rise to the typical football impacts considered here, are sufficient to keep shear strain well below the tissue tolerance levels.

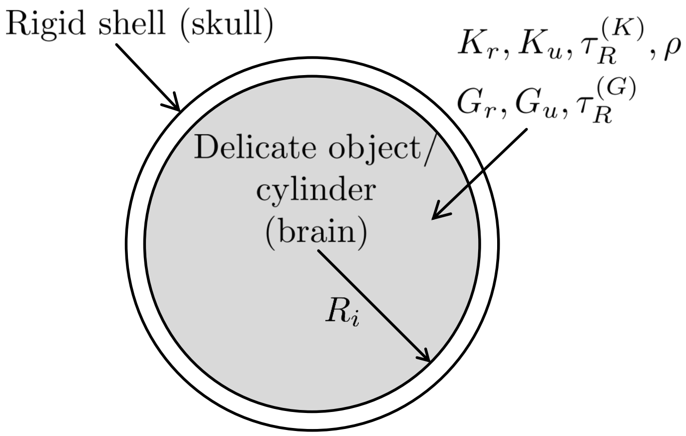

Figure 3.1: Diagram of a cylindrical delicate object that is enclosed by a rigid shell. The rigid shell is perfectly attached to the outer radius of the delicate object, so the motion of the rigid shell is transfered directly to the material on the outer radius of the cylinder. The shell, and therefore also the material on the outer radius of the cylinder, is forced to follow a prescribed trajectory. The rigid shell is an analog to the skull and the cylinder is analogous to the brain. The size of the cylinder is described by its outer radius, R_i. The cylinder material is a linear visco-elastic material with density ρ. The shear response is modeled with a Standard Linear Solid, with the parameters G_r, G_u and $\tau_R^{(G)}$. The volumetric response is modeled with either linear elasticity, with K_0 for the bulk modulus, or another SLS model, with the parameters K_r, K_u and $\tau_R^{(K)}$. The unrelaxed and relaxed shear moduli, G_u and G_r, are much smaller than the bulk modulus, K_0, and the unrelaxed and relaxed bulk moduli, K_u and K_r.

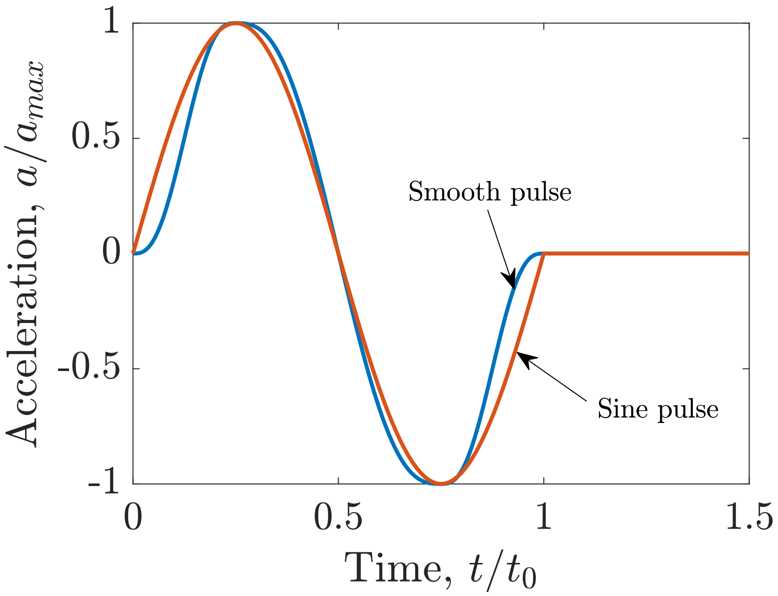

Figure 3.2: The magnitude of the linear, unidirectional acceleration of the cylinder's outer radius, a, as a function of time. The magnitude of the acceleration is normalized by its maximum value over time, a_{max}, and time, t, is normalized by the duration of the pulse itself, t_0. The smooth pulse was used in the analysis of the maximum shear strain, and the sine pulse was used in the study of the pressure magnitude. Both forms have a positive region and a negative region, and both result in the final speed of the cylinder's outer radius being equal to its initial speed.

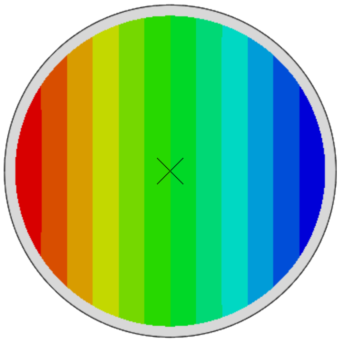

Figure 3.3: Dimensionless pressure distribution, $\tilde{p}(\tilde{t}, \tilde{x}, \tilde{y}) = p(t, x, y)/(a(t)\rho R_i)$, due to a linear acceleration pulse of sinusoidal shape, oriented along the horizontal unit vector. The darkest red corresponds to a value of 1 and the darkest blue corresponds to a value of -1. The even spacing of the contours indicates that pressure varies linearly across the cylinder, with no pressure along the vertical line that passes through the center of the cylinder. The magnitude of this field varies in time with the magnitude of the acceleration.

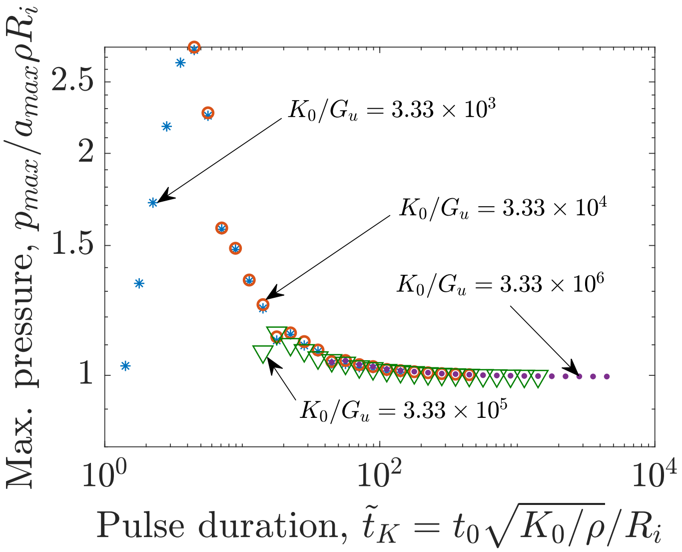

Figure 3.4: Maximum dimensionless pressure as a function of dimensionless acceleration pulse duration and K_0/G_u ratio. The human brain has a K_0/G_u ratio on the order of 2×10^5 and sports-related impacts have dimensionless pulse durations larger than 40, so the maximum pressure that develops in such an impact is proportional with the maximum acceleration of the cylinder's outer radius.

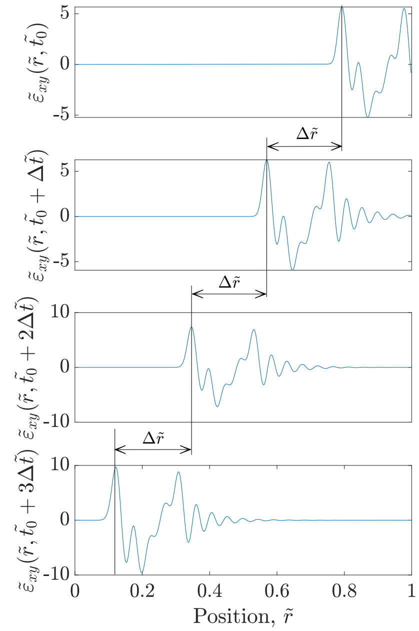

Figure 3.5: Dimensionless shear strain at four time-points after the completion of the acceleration pulse. The dimensionless distance that a nondispersive pulse travels in the time Δt, if it has speed $\sqrt{G_u/\rho}$, is $\Delta\tilde{r}$ and is marked on the plots with a two-sided arrow that spans this dimensionless distance. This approximates the distance that the simulated wave travels; therefore, the speed of the pulse can be seen to be roughly $\sqrt{G_u/\rho}$

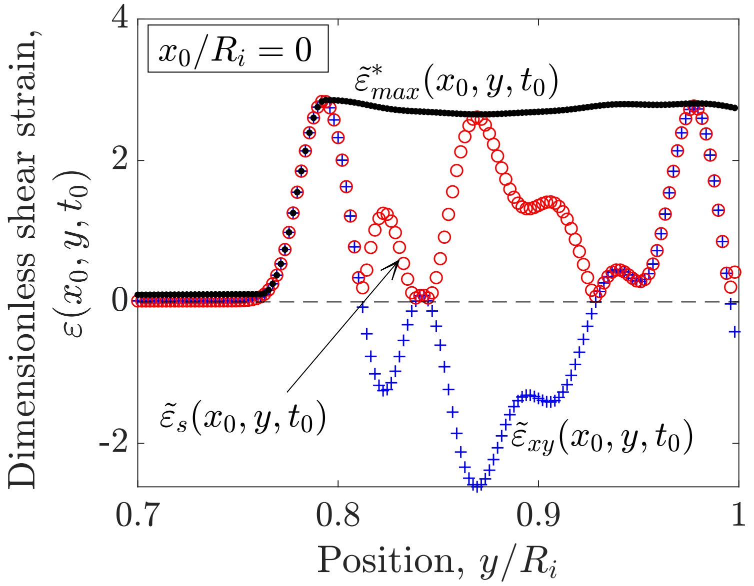

Figure 3.6: Example of the relationship between the shear component of the strain tensor,$\tilde{\varepsilon}_{xy}$, the maximum shear strain with respect to Mohr's circle, $\tilde{\varepsilon}_s$, and the maximum shear strain that has occurred up to time t, $\tilde{\varepsilon}^*_{max}(t)$. The direction of the propagation of the shear wave is toward lower values of dimensionless vertical position, y/R_i.

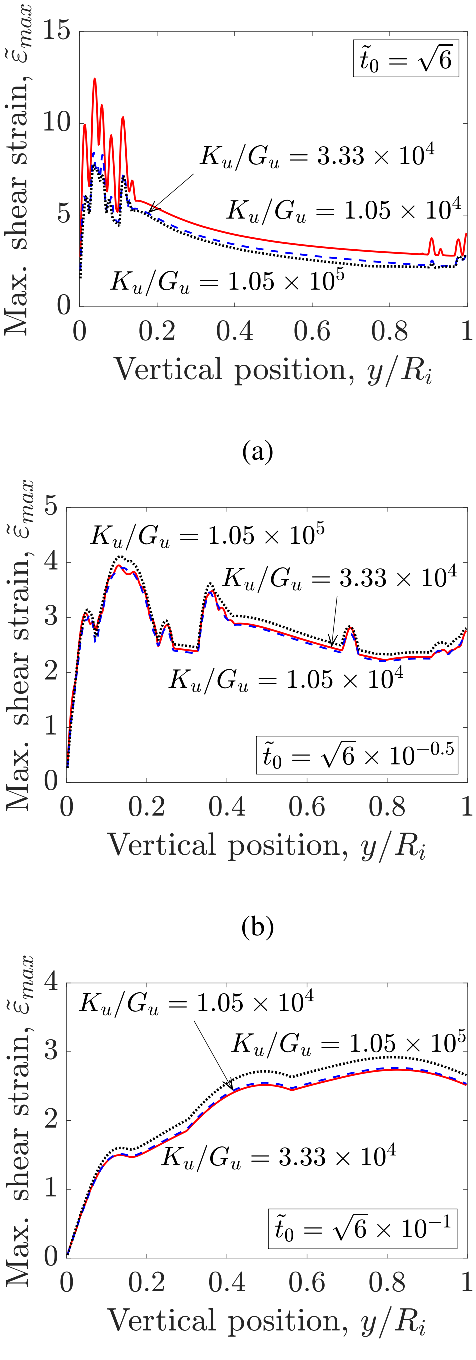

Figure 3.7: Maximum dimensionless shear strain within the cylinder as a function of position for three different ratios G_u/K_u and eleven dimensionless pulse durations $\tilde{t}_0$. a.) $\tilde{t}_0 = \sqrt{6} \times 10^{-1}$ b.) $\tilde{t}_0 = \sqrt{6} \times 10^{-0.5}$ c.) $\tilde{t}_0 = \sqrt{6} \times 10^{0}$.

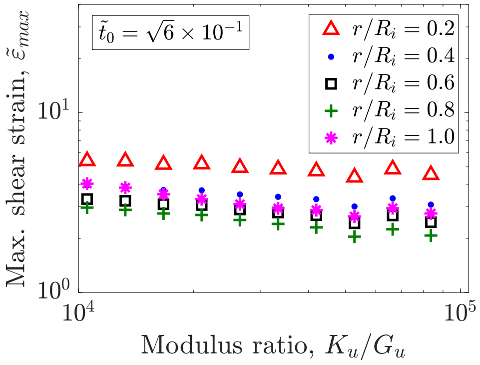

(a)

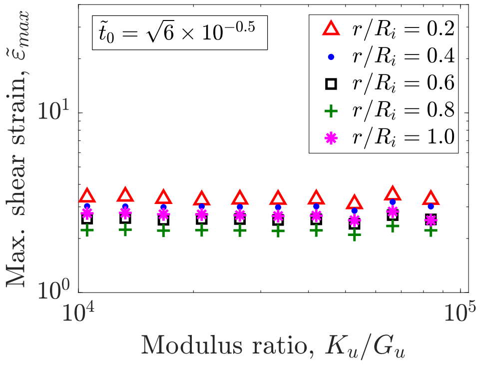

(b)

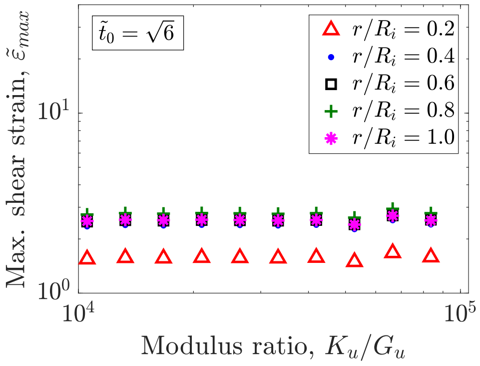

(c)

Figure 3.8: Maximum dimensionless shear strain within the cylinder at five location as a function of K_u/G_u for three different pulse durations. a.) $\tilde{t}_0 = \sqrt{6} \times 10^{-1}$. b.) $\tilde{t}_0 = \sqrt{6} \times 10^{-0.5}$ c.) $\tilde{t}_0 = \sqrt{6} \times 10^{0}$

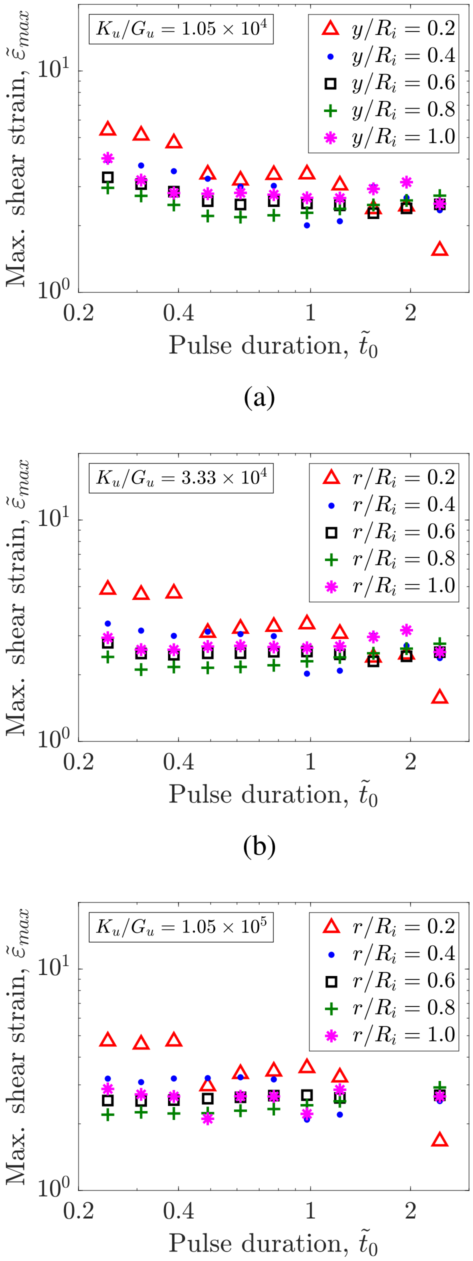

(a)

(b)

(c)

Figure 3.9: Maximum dimensionless shear strain at five positions along the vertical line passing through the center of the cylinder. Maximum dimensionless shear strain is plotted as a function of dimensionless pulse duration, $\tilde{t}_0$, for three different K_u/G_u ratios.

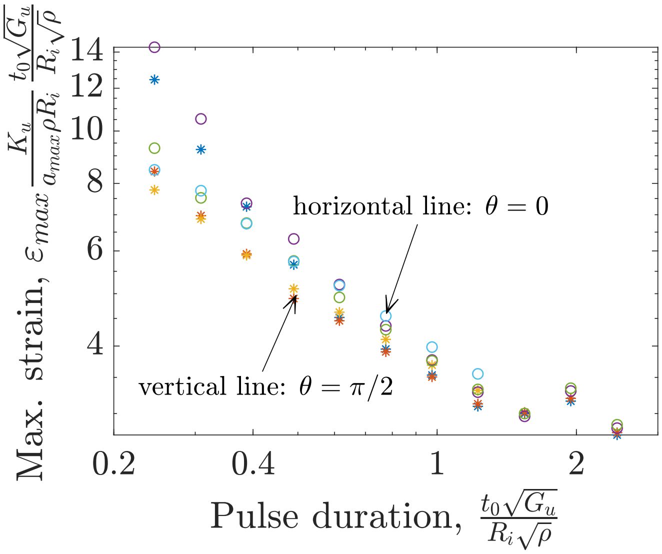

(a)

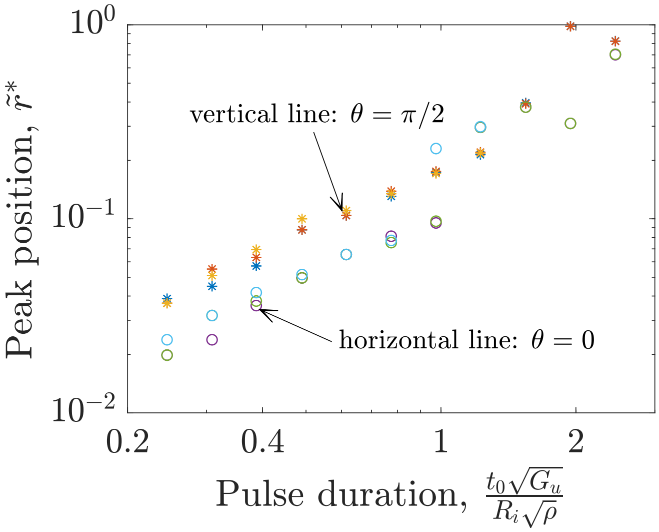

(b)

Figure 3.10: (a) Maximum strain along the vertical ($*$) and the horizontal ($\circ$) lines that pass through the center of the cylinder. Inspection of spatial contour plots of maximum shear strain distributions indicate that the spatial maxima for dimensionless maximum shear strain are always located on either the vertical or horizontal line that passes though the cylinder. Decreasing dimensionless pulse duration increases the maximum dimensionless shear strain along both the horizontal and vertical lines considered here. (b) Decreasing dimensionless pulse duration, $\tilde{t}_0$, is associated with the spatial maximum of dimensionless maximum shear strain occurring at a position, $\tilde{r}^*$, that is closer to the center of the cylinder.

CHAPTER IV

Analytical calculation of shear strain within a rotating cylinder and comparison with finite element results

4.1 Introduction

Most injurious head impacts involve both linear motion of the skull and rotational motion of the skull. Unterharnscheidt suggests that focal injuries are primarily caused by high pressures within the brain, due to linear acceleration, whereas diffuse injury is more likely to be caused by rotation [38]. In the previous chapter, a finite element model of a visco-elastic cylinder, modeled with a Standard Linear Solid constitutive model, with brain-like properties and dimensions, was used to study both the pressure and strain caused by linear acceleration of the brain's outer radius. It was shown that the shear strain is relatively small in linear impacts. In this chapter, an analytical model for calculating the shear strain brought on by the rotation of the outer shell of a similarly idealized cylindrical head model, with a homogeneous SLS visco-elastic material model for the brain's shear response and no compressibility, will be described. Then, some results obtained with this model will be compared to those from a finite element analysis of a nearly identical scenario, in order to verify the accuracy of the analytical approach. The model described in this chapter is the basis for the results and discussion presented in the next two chapters, Chapter V and VI. Chapters V and VI both include discussions of which qualitative aspects of the time-dependence of the rotational motion of the shell influence the interior cylinder strain most heavily, so we take this opportunity to describe the four different pulse shapes which form the basis of those analyses. As with the previous chapter, our attention remains focused on identifying the cylinder parameters that influence the scaling between the maximum shear strain and kinematic descriptions of impact severity.

The link between rotation of the skull and brain tissue injury is the dangerously high levels of shear strain that evolve during rotational impacts [28, 16, 32]. Sometimes, the first principal strain is used to quantify the extent of deformation [22, 43], though the maximum shear strain provides a similar type of result, as explained in Section 3.2. Similarly, tissue-level tolerances for deformation are sometimes expressed in terms of Lagrange strain [29]. Although there are slight differences in the exact definitions of these various strains, they all attempt to describe similar types of deformation. Since the brain has a very high bulk modulus [32], the volumetric deformation of the brain is constrained to be quite small, so most measures of strain will be dominated by the deviatoric strain. In this model, where the shear strain is the only component of strain, because the material is modeled as an incompressible solid, this single strain component is expected to show the same trends as most other strain measures.

An analytical solution to this rotational kinematic loading problem, such as the one presented in this chapter, is particularly advantageous in this situation because the shear waves in the brain move very slowly, due to the low value of the shear modulus of the medium. Recent work by Giudice et al. [12] suggests that some of the commonly used finite element models produce vastly different results for maximum principal strain when the element type is changed or the mesh is refined. This is concerning, as numerical dispersion in inadequately meshed models is well-documented and dispersion of this kind results in under-prediction of strain. Even studies that confirm convergence for the mesh, using one set of constitutive properties, need to ascertain whether the mesh remains adequate if new, more compliant, material properties are substituted into the original model. The effect of an overly-coarse mesh was seen in early versions of the the finite element model used here, and was corrected after a mesh refinement study was completed.

The analysis presented here relies heavily on previous analyses that use purely analytical approaches to calculate the strain in a rotating cylinder. One assumption that is common to several previous analyses, and will be used in this chapter and the next two chapters, is the elimination of compressibility within the cylinder medium. Although the brain and other structures have some compressibility, it is accepted that for rapid impacts, this small amount of compressibility can be ignored [6]. Eliminating compressibility and choosing a simplified cylindrical geometry, as in the previous chapter, facilitates simplifying the two-dimensional problem into a one-dimensional partial differential equation, with only circumferential displacement and the resulting radial-circumferential shear strain allowed. Earlier work on this problem explicitly considers this one-dimensional approach as a model for diffuse axonal injury, as in the work by Margulies and Thibault [25, 26]. The first of these early studies includes a description of an analytical approach for calculating strain due to impacts of various durations [25], and the latter offers an associated tolerance criterion for the human brain [26]. The analysis in these studies is based on the deformation of a visco-elastic cylinder with a Kelvin-Voigt model, for which the influence of shear modulus and loading duration on the strain experienced within the brain is evident. More recently, due to interest in new techniques for measuring brain deformation directly, the solution to a related problem, involving similar geometry, is used to verify the performance of a transient strain detection method, in work by Bayly et al. [5]. The solution provided there is for the deformation in a cylinder of SLS visco-elastic media brought to rest from an initially rotating state, and uses a Laplace transform method to arrive at the solution. Later related work, by Massouros et al., addresses the rotation of a cylinder with a Maxwell visco-elastic material definition and obtains an analytical solution [27]. Each of these studies involves at least one facet of the problem we seek to answer in the next few chapters.

4.2 Model

As with the finite element model in the previous chapter, the delicate object considered in the next two chapters is a cylinder made of visco-elastic media that is fully bonded to a rigid exterior shell, and is subject to plane-strain conditions. Whereas the previous chapter focused on the cylinder's response to linear acceleration of its shell, $a(t)$, this chapter, and the two that follow it, are focused on the response of the cylinder to the prescribed rotation of the shell that bounds it. Specifically, the rotation of the shell about its center, in the radial-circumferential plane, with its angular velocity vector parallel to the axial direction, is of interest. Since the geometry under consideration is two dimensional, this is the only possible direction the angular velocity vector can point, and the angular velocity has only one component. When the shell rotates about the cylinder's longitudinal axis, the angle that each point on the rigid shell traces out with respect to its original orientation, $\theta(t)$, fully characterizes this motion. Since it is a rigid body, the angle that each point on the shell sweeps out is the same, regardless of the circumferential coordinates of each point.

The first and second time-derivatives of the angular displacement, $\dot{\theta}$ and $\ddot{\theta}$, are referred to here as the the angular velocity and the angular acceleration of the shell. This mirrors the convention in the literature to use these symbols to refer to the angular velocity and angular acceleration of the skull during a rotational impact [30]. Alternatively, symbols involving ω and α are also commonly used to represent these variables within head injury research [5, 10, 22, 36]. Nevertheless, the $\dot{\theta}$ framework is used here in order to emphasize that $\dot{\theta}(t)$ and $\ddot{\theta}(t)$ are scalar, not vector quantities. They are scalar quantities because they are the time-varying components of the angular velocity and angular acceleration vectors, which are both constrained to have but one component in this scenario. Further, this eliminates any confusion between $\dot{\theta}(t)$ and angular frequencies, which are often represented with ω alone. Since there is only one component of angular velocity and angular acceleration involved in the motion of the cylinder's shell, these components will be referred to as the angular velocity and angular acceleration themselves.

The circumferential displacement by points at the outer radius of the cylinder can be expressed with the symbol, $u_\theta(R_i, t)$. $u_\theta(R_i, t)$ is directly proportional to $\theta(t)$ and to R_i, the outer radius of the cylinder, such that

$$u_{\theta,t}(r, t) = R_i\theta(t). \tag{4.1}$$

The strain that is brought on by the rotation of shell, and the circumferential motion of the cylinder's outer radius, is due to the radial variations in the relative circumferential displacement of the material points within the cylinder, $u_\theta(r, t)/r$, and can be calculated directly from the displacement field using a strain-displacement relation. These quantities are indicated on the diagram in Figure 4.1.

The other difference between the model that is analyzed in this chapter and the one from the previous chapter is volumetric behavior of the material. Although the materials in the previous chapter had a visco-elastic response for the volumetric deformation as well as the deviatoric deformation, the materials considered in this chapter are incompressible and have an SLS-type behavior for the deviatoric response, only.

4.2.1 Mathematical model and solution

The governing equation used to calculate the circumferential displacement within the interior of the cylinder, $u_\theta(r, t)$, is derived from the analysis in [5]. In that paper, the correspondence principle is used to obtain the governing differential equation for the visco-elastic case from the equation for the analogous elastic case. This step of the analysis takes place in the Laplace domain. Alternatively, the visco-elastic solution can be obtained directly, within the time domain, as is demonstrated here. The equation of motion for the cylinder interior is

$$\frac{\partial \sigma_{r\theta}}{\partial r} + \frac{2}{r}\sigma_{r\theta} = \rho\frac{\partial^2 u_\theta}{\partial t^2}, \tag{4.2}$$

where r is the radial position coordinate, t is the time, ρ is the density of the cylinder medium, $\sigma_{r\theta}$ is the shear stress, and u_θ is the circumferential coordinate of displacement. The constitutive equation for the cylinder medium takes the SLS form, expressed as

$$\sigma_{r\theta} + \tau_R \frac{d\sigma_{r\theta}}{dt} = 2G_u \varepsilon_{r\theta} + 2G_r \tau_R \frac{d\varepsilon_{r\theta}}{dt}, \tag{4.3}$$

where $\varepsilon_{r\theta}$ is the tensor shear strain, G_u is the unrelaxed shear modulus, G_r is the relaxed shear modulus, and τ_R is the relaxation time. Rigorously, this is accompanied by the initial condition that $\sigma_{r\theta}(0^+) = 2G_u \varepsilon_{r\theta}(0^+)$, but this is not an essential aspect of the analysis since both the stress and strain have no discontinuities. The strain-displacement relation for the radial-circumferential shear strain is

$$\varepsilon_{r\theta} = \frac{1}{2}\left(\frac{\partial u_\theta}{\partial r} - \frac{u_\theta}{r}\right). \tag{4.4}$$

The governing equation for circumferential displacement, u_θ, can be derived from combining these. Multiplying Equation 4.2 by τ_R and taking its derivative with respect to time, and adding that equation to the original form of 4.2 results in the expression

$$\left(\frac{\partial \sigma_{r\theta}}{\partial r} + \frac{2}{r}\sigma_{r\theta}\right) + \tau_R \frac{d}{dt}\left(\frac{\partial \sigma_{r\theta}}{\partial r} + \frac{2}{r}\sigma_{r\theta}\right) = \rho \frac{\partial^2 u_\theta}{\partial t^2} + \tau_R \frac{d}{dt}\left(\rho \frac{\partial^2 u_\theta}{\partial t^2}\right). \tag{4.5}$$

This can be re-arranged into

$$\frac{\partial}{\partial r}\left(\sigma_{r\theta} + \tau_R \frac{d}{dt}\sigma_{r\theta}\right) + \frac{2}{r}\left(\sigma_{r\theta} + \tau_R \frac{d}{dt}\sigma_{r\theta}\right) = \rho \frac{\partial^2 u_\theta}{\partial t^2} + \tau_R \rho \frac{\partial^3 u_\theta}{\partial t^3}. \tag{4.6}$$

By substituting 4.4 into 4.3, displacements can be related directly to stress and its derivatives, and the resulting expression can be substituted into 4.6 to obtain the governing equation. Distributing out the derivatives gives

$$\left(\frac{G_r\tau_R}{2}\frac{\partial^3 u_\theta}{\partial t\,\partial r^2}+\frac{G_u}{2}\frac{\partial^2 u_\theta}{\partial r^2}\right)+\frac{1}{r}\left(\frac{G_r\tau_R}{2}\frac{\partial^2 u_\theta}{\partial t\,\partial r}+\frac{G_u}{2}\frac{\partial u_\theta}{\partial r}\right) \\ -\frac{1}{r^2}\left(\frac{G_r\tau_R}{2}\frac{\partial u_\theta}{\partial t}+\frac{G_\infty}{2}u_\theta\right)-\rho\left(\tau_R\frac{\partial^3 u_\theta}{\partial t^3}+\frac{\partial^2 u_\theta}{\partial t^2}\right)=0.$$

A dimensionless form of this equation is

$$\beta_r\tilde{r}^2\frac{\partial^3\tilde{u}_\theta}{\partial\tilde{t}\partial\tilde{r}^2}+\beta_u\tilde{r}^2\frac{\partial^2\tilde{u}_\theta}{\partial\tilde{r}^2}+\beta_r\tilde{r}\frac{\partial^2\tilde{u}_\theta}{\partial\tilde{t}\partial\tilde{r}}+\beta_u\tilde{r}\frac{\partial\tilde{u}_\theta}{\partial\tilde{r}}-\beta_r\frac{\partial\tilde{u}_\theta}{\partial\tilde{t}}-\beta_u\tilde{u}_\theta-\tilde{r}^2\frac{\partial^3\tilde{u}_\theta}{\partial\tilde{t}^3}-\tilde{r}^2\frac{\partial^2\tilde{u}_\theta}{\partial\tilde{t}^2}=0 \tag{4.7}$$

where the dimensionless quantities are

$$\tilde{u}_\theta=u_\theta/R_i \tag{4.8}$$

$$\tilde{t}=t/\tau_R \tag{4.9}$$

$$\tilde{r}=r/R_i \tag{4.10}$$

$$\beta_r=\frac{G_r\tau_R^2}{\rho R_i^2} \tag{4.11}$$

$$\beta_u=\frac{G_u\tau_R^2}{\rho R_i^2} \tag{4.12}$$

where R_i is the radius of the cylinder.

A Fourier transform of 4.7 results in the equation

$$(i\tilde{\omega}\beta_r+\beta_u)\left(\tilde{r}^2\frac{\partial^2\tilde{u}_\theta}{\partial\tilde{r}^2}+\tilde{r}\frac{\partial\tilde{u}_\theta}{\partial\tilde{r}}-\tilde{u}_\theta\right)-\tilde{r}^2\left((i\tilde{\omega})^3+(i\tilde{\omega})^2\right)\tilde{u}_\theta=0 \tag{4.13}$$

which can be rearranged as

$$\tilde{r}^2\frac{\partial^2\tilde{u}_\theta}{\partial\tilde{r}^2}+\tilde{r}\frac{\partial\tilde{u}_\theta}{\partial\tilde{r}}-\left(\frac{(i\tilde{\omega})^3+(i\tilde{\omega})^2}{i\tilde{\omega}\beta_r+\beta_u}\tilde{r}^2+1\right)\tilde{u}_\theta=0. \tag{4.14}$$

Choosing a change of variables $x = \tilde{r}\beta$ where

$$\beta = \sqrt{\frac{(i\tilde{\omega})^3 + (i\tilde{\omega})^2}{i\tilde{\omega}\beta_r + \beta_u}} \tag{4.15}$$

gives the equation

$$x^2 \frac{\partial^2 \tilde{u}_\theta}{\partial x^2} + x \frac{\partial \tilde{u}_\theta}{\partial x} - \left(x^2 + 1\right) \tilde{u}_\theta = 0. \tag{4.16}$$

Equation 4.16 has the form of the modified Bessel equation, which has the modified Bessel functions as solutions. Since the circumferential displacement at the center of the disk must be zero, there is no contribution from the modified Bessel functions of the second kind. The solution then has the form

$$\tilde{u}_\theta(\tilde{r}, \tilde{\omega}) = (U_0/R_i) \frac{I_1(\tilde{r}\beta)}{I_1(\beta)}, \tag{4.17}$$

where U_0 is the amplitude of the circumferential displacement of the points on the cylinder's outer radius.

The strain within the cylinder may be calculated in either the time domain or frequency domain, though it is generally more efficient to do this calculation in the frequency domain before transforming the solution back into the time domain. When the operations are performed in that order, derivatives need only be taken once at each location rather than for each time point for which strain is requested. This is much more efficient when the complete time-dependence of the strain is of interest.

Multiplying 4.17, or the associated strain, by the frequency spectrum of the circumferential displacement of the points on the outer radius of the cylinder, $u_\theta(R_i, t)$, gives the frequency domain solution, which can be mapped back into the time domain numerically, using the inverse Fast Fourier Transform. This approach is well-suited for the consideration of acceleration pulses with different types of time-dependence.

4.3 Angular acceleration pulse shapes

Since the pulse shape matters in some circumstances, which are described further in Chapters V and VI, four different pulse shapes are introduced here and used in Chapters V and VI to probe the role that pulse shape plays in the magnitude of the shear strain within the cylinder. The four types of pulses used are the sine (Sine) pulse, the half sine (HS) pulse, the single rectangular (SR) pulse, and the bipolar rectangular (BR) pulse. Sketches of the dimensionless time-dependence of the dimensionless angular acceleration, $\tilde{\ddot{\theta}}(\tilde{t})$, of these four pulses is shown in Figure 4.2. The dimensionless pulse duration in this chapter and subsequent chapters is the same as $\tilde{t}_0$ from the previous chapter, which is defined as $\tilde{t}_0 = t_0\sqrt{G_u/\rho}/R_i$. The time in the simulation is likewise dimensionless, with $\tilde{t} = t\sqrt{G_u/\rho}/R_i$. The dimensionless maximum angular acceleration magnitude is $|\tilde{\ddot{\theta}}|_{max} = |\ddot{\theta}|_{max}\rho R_i^2/G_u$.

These pulse shapes were selected for this investigation because they can be neatly categorized in two different ways. First, they can be categorized by their sharpness or smoothness. The sine pulse and the half sine pulse have a relatively smooth increase in acceleration, initially. In contrast, the single rectangular pulse and the bipolar rectangular pulse have steep, sharp increases and decreases in acceleration. The second method of categorizing these pulses is to divide them by the angular speed that the angular acceleration pulse imparts to the shell, which was initially at rest, $|\dot{\theta}|_f$. The sine pulse and the bipolar rectangular pulse both result the the final angular speed of the shell being 0 rad/s, $|\dot{\theta}|_f = 0$ rad/s. In contrast, the half sine and single rectangular pulses result in the angular speed of the shell being non-zero ($|\dot{\theta}|_f \neq 0$).

Considering these four pulse types, two different ways of defining the dimensionless pulse duration are possible. They are the true dimensionless pulse duration, $\tilde{t}_0$, which is defined in the previous chapter and is familiar, and includes both the positive and negative regions. The other is the dimensionless duration of only the positive section of the pulse, $\tilde{t}_p$. For the pulses which have a non-zero final angular speed, such as the half sine pulse and the rectangular pulse, these two dimensionless durations are the same. However, $\tilde{t}_p$ is half of $\tilde{t}_0$ for the sine pulse and the bipolar rectangular pulse. It will be shown later that the quantity $\tilde{t}_p$ is sometimes more useful in comparing pulses of different types to one another than $\tilde{t}_0$ is.

4.4 Validation of analytical results with analogous finite element calculations

The solution method in Section 4.2.1 is verified by comparing the shear strain fields calculated with it to analogous results obtained with a finite element model, for a nearly identical situation.

The finite element models used to validate the analytical results have a small amount of compressibility, which does not affect the calculated shear strains significantly. Specifically, the results in the figures discussed in this section are for cylinders that have 8.37×10^4 as their bulk modulus to unrelaxed shear modulus ratio. This value was chosen for the validation study because it is the ratio of 2.4 kPa to 0.2 GPa. 2.4 kPa is a relatively low estimate for the shear modulus of the brain. Although the bulk modulus of the brain is probably closer to 2.19 GPa than 0.2 GPa, increasing the bulk modulus to 2.19 GPa extended the computational time significantly, with negligible influence on the calculated shear strains.

Figure 4.3, Figure 4.4, and Figure 4.5 depict the comparison between the finite element results and the analytical results, with the analytical results represented with lines and the finite element results represented with dots and circles. Figure 4.3 considers the strain at the outer radius of the cylinder, $\tilde{r} = 1$, as a function of time. The strain from three scenarios is depicted. The different scenarios each correspond to the cylinder's shell experiencing a prescribed angular acceleration in the shape of the a sine pulse, each with different dimensionless duration, $\tilde{t}_0$. In this figure, the magnitude of the shear strain is normalized by the magnitude of the angular acceleration pulse, and that normalized quantity is rendered dimensionless with other system variables, such as the unrelaxed modulus of the cylinder medium. The dimensionless quantity corresponding to the magnitude of the shear strain is $|\tilde{\varepsilon}_{r\theta}| = |\varepsilon_{r\theta}|\sqrt{G_u/\rho}/(R_i\dot{\theta}_{max})$, where $|\dot{\theta}|_{max}$ is the maximum angular speed that the shell attains during the loading pulse. $|\dot{\theta}|_{max}$ is not the same as $|\dot{\theta}|_f$, though the value of $|\dot{\theta}|_f$ is the same as the value for $|\dot{\theta}|_{max}$, when the acceleration pulse has the sine pulse shape or the rectangular pulse shape.

The other dimensionless parameters that describe these simulations are the dimensionless relaxation time, $\tilde{\tau}_R$, and the ratio of the relaxed shear modulus to the unrelaxed shear modulus, G_r/G_u. For Figure 4.3, the dimensionless relaxation time, $\tilde{\tau}_R$, and ratio of the relaxed and unrelaxed shear moduli, G_r/G_u, are held constant. Their values are $\tilde{\tau}_R = 2.45$ and $G_r/G_u = 0.2$. Figure 4.4 confirms that altering the ratio of the relaxed and unrelaxed shear moduli, G_r/G_u, does not reduce the accuracy of the analytical calculations. For Figure 4.5, four different dimensionless relaxation times are investigated in the same way. For the three shorter dimensionless relaxation times, the finite element results and the analytical results agree well.

There was only one instance of the analytical incompressible results not correlating well with the finite element results. This was for the simulation involving $\tilde{\tau}_R = 24.5$ in Figure 4.5. In this case, the finite element results have relatively high frequency vibrations that occur near sharp changes in the time-derivative of the shear strain, whereas these oscillations do not appear in the analogous analytical result. However, the maximum values of shear strain still correlate quite well in this situation, and that is the quantity that is of the most importance in subsequent sections. Nevertheless, further study of this difference between the finite element results and analytical results under these conditions is warranted. One possible cause of the additional oscillations in the finite element simulations is an insufficiently fine mesh or insufficiently small time steps in this model. Spurious oscillations are known to develop on some occasions when a mesh is inadequate. The larger dimensionless relaxation time in this situation, $\tilde{\tau}_R = 24.5$, is associated with less dissipation of high frequency vibrations, and the initial mesh refinement study for this model was performed with a smaller dimensionless relaxation time and higher unrelaxed modulus, G_u, so it is possible that the mesh needs to be refined further to gather accurate results for this set of parameters, when using the finite element method.

4.5 Conclusion

In this chapter, an analytical method for calculating the shear strain within a viscoelastic cylinder that is enclosed within and connected to a rigid rotating shell, was presented and validated with results from analogous finite element simulations. Terms for the quantification of the motion of the bounding shell, such as $\dot{\theta}(t)$, were also introduced, as were some dimensionless parameters that are useful in reducing the number of variables needed to describe the essential character of the system, such as $\tilde{\tau}_R$. The four pulse shapes that are used in subsequent chapters to probe the affect of altering the time dependence of the angular acceleration pulse, $\ddot{\theta}(t)$, were also described here. This chapter, in conjunction with previous discussion of short and long duration responses, is intended to supply the background and some of the terminology necessary for understanding the context of the results and discussion in the next two chapters.

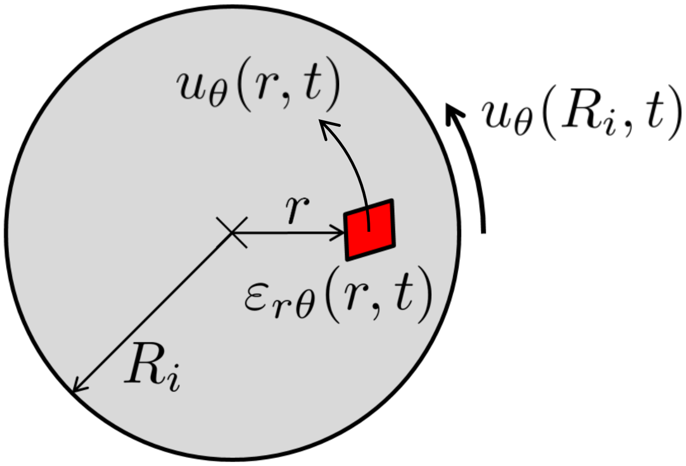

Figure 4.1: Diagram of circumferential displacement and shear strain in rotational impacts. The rotation of the outer shell (not shown) about its center produces circumferential motion of the points on the outer radius of the cylinder, $u_\theta(R_i,t)$. The circumferential displacement of points within the cylinder, $u_\theta(r,t)$, are driven by the motion at the outer radius of the cylinder. Radial variation in the $u_\theta(r,t)/r$ field produces the radial-circumferential strain field, $\varepsilon_{r\theta}(r,t)$.

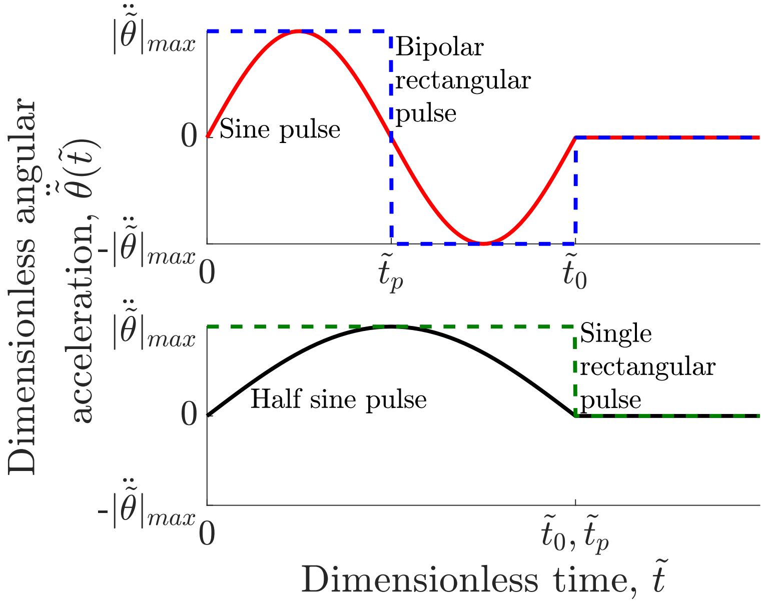

Figure 4.2: Four angular acceleration pulse shapes and their dimensionless angular acceleration as a function of dimensionless time. The dimensionless pulse duration $\tilde{t}_0$ and the dimensionless positive pulse duration, $\tilde{t}_p$ are indicated on the x-axis for each.

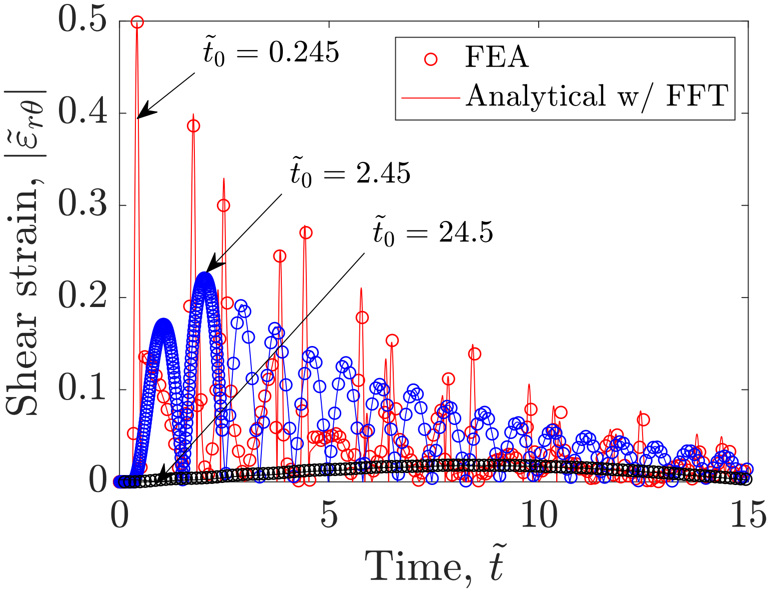

Figure 4.3: Comparison of analytical and FEA solutions for dimensionless shear strain as a function of dimensionless time for angular acceleration pulses with three different dimensionless pulse durations. The analytical and finite element analysis results agree for both short pulses ($\tilde{t}_0 = 0.245$), intermediate-duration pulses ($\tilde{t}_0 = 2.45$) and long pulses ($\tilde{t}_0 = 24.5$). $\tilde{\tau}_R = 2.45$, $G_r/G_u = 0.2$.

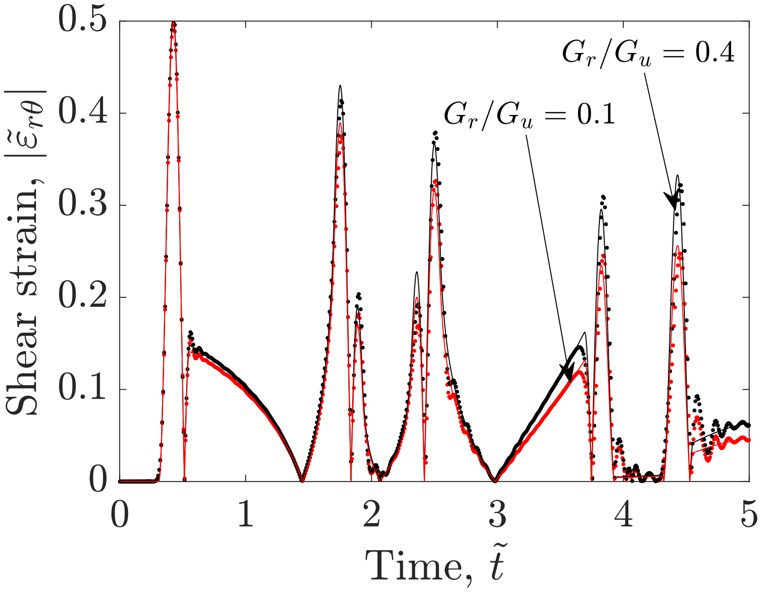

Figure 4.4: Comparison of analytical and FEA solutions for two different ratios of G_r to G_u. $\tilde{\tau}_R = 2.45$, $\tilde{t}_0 = 0.245$.

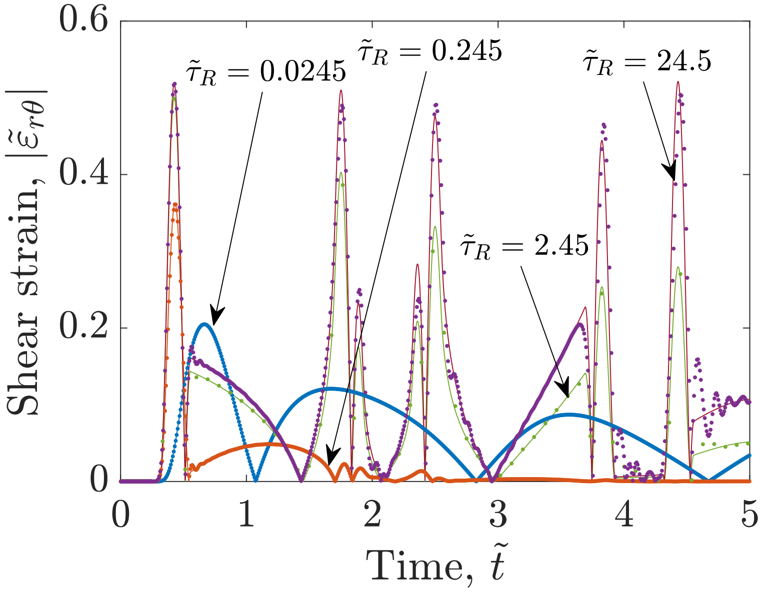

Figure 4.5: Comparison of analytical and FEA solutions for four different dimensionless relaxation times, $\tilde{\tau}_R$. $\tilde{t}_0 = 0.245$, $G_r/G_u = 0.2$.

CHAPTER V

Characteristics of the long pulse response and the short pulse response

5.1 Introduction

In the previous chapter, a model for the shear strain that evolves in a cylinder enclosed in a shell, when the shell is forced to rotate about the cylinder's longitudinal axis, was described. The application of a prescribed amount of angular acceleration to the shell surrounding the cylinder is referred to as an "angular acceleration pulse." This type of shell motion brings about internal dynamic deformation within the cylinder. In this chapter, this model will be used to calculate the shear strain that evolves in a diverse range of scenarios, and the responses in these scenarios will be described and then categorized. The primary variable for categorizing the dynamic response of the class of delicate objects studied here is the duration of the angular acceleration pulse. The primary question to be answered for any kinematic loading event of this type is whether that duration is shorter than the characteristic time of the cylinder, and therefore induces the "short pulse response", or if the angular acceleration pulse duration is longer than the characteristic time of the cylinder and produces the "long pulse response." The "short pulse response" and the "long pulse response" of a spring-mass system are discussed in detail in Section 1.1, and the goal of this chapter is to describe how the concepts described there, and analogous behaviors, are manifested by this similar, but more complicated, system.

In this effort to describe the short and long pulse responses, and delineate differences between them and identify the causes of these differences, this chapter will focus on how the spatial distribution of shear strain within the cylinder depends on the magnitude, duration, and time-dependence shape of the angular acceleration of the shell, $\ddot{\theta}(t)$. Both the time-dependent changes to the strain field and the maximum shear strain magnitude will be considered. That is, trends in both the time-dependence of shear strain, $\varepsilon_{r\theta}(r,t)$, and the temporal maxima of those functions, $\varepsilon_{r\theta}^{max}(r)$, will be identified and linked back to pulse duration, t_0, the pulse's shape, (*e.g.* sine, half sine, rectangular, bipolar rectangular), the unrelaxed modulus of the cylinder, G_u, and the cylinder's visco-elastic stress relaxation time, τ_R. These trends underpin the dominant features of the short-pulse response and the long-pulse response, and the phenomena described in this chapter will be categorized by whether they mainly operate during short pulses or long pulses. An understanding of how different combinations of these parameters and pulse shapes bring about different types of shear strain response, in both a qualitative and quantitative sense, is necessary context for the discussion of the scaling laws that relate maximum shear strain to kinematic attributes of impacts. Providing evidence for, and analysis of, these dimensionless scaling laws is the purpose of the next chapter, Chapter VI.

The first section of this chapter addresses the long-pulse response and the second section concerns the short-pulse response. When the angular acceleration pulse is long, the strain response reaches dynamic equilibrium, so the strain fields that develop have a steady-state component and a transient component. The short-pulse response is mainly characterized by the propagation of transient shear waves, that are created by the circumferential motion of the cylinder's shell. This motion is perpendicular to the direction the wave can propagate, so it produces a shear wave. The overall shape (i.e. qualitative temporal evolution) of the strain response that is produced by the motion of the shell, the initial magnitude and maximum value of this strain response, and how the shear wave propagates and attenuates over time and space, are analyzed in this section.

5.2 Short-pulse and long-pulse limits for dynamic systems

A diagram of the rotational loading of a compliant visco-elastic cylinder, and the shear strain that results, is given in Figure 5.1. The compliant visco-elastic cylinder of interest here has density, ρ, and is incompressible. It has a visco-elastic response to deviatoric stress and strain that can be modeled with the Standard Linear Solid (SLS) model, which is parameterized by the unrelaxed shear modulus, G_u, the relaxed shear modulus, G_r, and the stress relaxation time, τ_R. The size of the cylinder is described by its radius, R_i. The cylinder in enclosed within a rigid shell, and its exterior is bonded to the inner surface of the shell. The only non-zero component of angular acceleration of the shell, $\ddot{\theta}(t)$, can be forced to follow a particular functional form, such as that of a rectangular pulse of amplitude $|\ddot{\theta}|_{max}$ and duration t_0. The cylinder and its shell are initially at rest, and the angular acceleration pulse being applied to the shell causes the shell to rotate with angular velocity $\vec{\omega}(t) = \dot{\theta}(t)\hat{z}$, where $\hat{z}$ is the longitudinal axis of the cylinder, which points out of the plane defined by the radial and circumferential unit vectors.

The angle swept out by the points on the shell, $\theta(t)$, produces the circumferential displacement $u_\theta(R_i, t) = R_i\theta(t)$ at the outer radius of the cylinder. The angular velocity component, $\dot{\theta}$, and the angular acceleration component, $\ddot{\theta}$, are the first and second time-derivatives of the angle that the shell rotates through, $\theta(t)$. In this chapter, these components will be referred to more simply as the angular velocity and the angular acceleration, since all other components of these vector quantities are constrained to be zero.

Compliant cylinders respond differently to angular acceleration pulses of different durations because of their internal dynamics. In the work by Kornhauser and Lawton [23], the internal dynamics of a spring-mass system are shown to respond in different ways to short acceleration pulses and long ones. Figures 1.1 and 1.2, reproduced here as Figures 5.2 and 5.3, are adapted from [23]. 5.3 provides examples of the types of response that are seen in the spring-mass system, shown in Figure 5.2a, and conveys how the different types of response have different injury mechanisms. Figure 5.2a is a diagram of the spring mass system, and Figure 5.2b is a diagram showing how the kinematic parameters associated with a linear acceleration pulse, $a_s(t)$, are determined. Figure 5.3a contains plots of the extension and compression of the spring as a result of two different, and representative, input acceleration pulses. A short-duration pulse produces a response that is dominated by the natural vibration of the system. The long-duration pulse results in the internal deformation having roughly the same normalized time-dependence as the angular acceleration input function has. In the short-pulse scenario, the maximum amount of deformation in the spring is proportional to the magnitude of the velocity change of the excitation point, which can be calculated by examining the time-integral of the acceleration pulse function. In the long-pulse scenario, the maximum deformation in the spring is proportional to the maximum acceleration of the excitation point. For very short impacts, damage is due to exceeding a threshold of the magnitude of the velocity change, v^{tol}, with little influence from the a_{max}-value of the impact. For very long impacts, damage is mainly due to exceeding an acceleration threshold a^{tol}, with little influence from the velocity Δv. The magnitude of the the velocity change matters more, and the maximum magnitude of acceleration matters less, as impulse duration shrinks. The dominance of the velocity-tolerance, v^{tol}, is one asymptote, and it applies to pulses with short durations. The velocity change matters less and the maximum of the magnitude of acceleration matters more as impulse duration increases. The dominance of the acceleration-tolerance, a^{tol}, is the other asymptote, and it applies to pulses of long durations. Figure 5.2c depicts what combinations of Δv and a_{max} cause damage to this type of simple dynamic system, and locates the examples in (b) within $\Delta v - a_{max}$ space.

As discussed in Chapter I, the asymptotes in Figure 5.2c are analogous to the “laws of injury” identified by Holbourn [16] and the pressure-impulse framework outlined by Hetherington [15] for all vulnerable objects. The rotational forms of these two types of responses are presented in the work of Ommaya and others [30], and are identifiable also in the work of Margulies and Thibault [25], which followed. In this chapter, the symbols $|\dot{\theta}|_{max}$ and $|\ddot{\theta}|_{max}$ will refer to the maximum of the magnitude of the angular velocity of the shell and the maximum of the magnitude of the angular acceleration of the shell, respectively. These are analogous to the the linear quantities Δv and a_{max}.

Since both the long and short-term shear moduli of the brain are quite low, each within an order of magnitude of 1 kPa, the transient waves that propagate within the brain are relatively slow-moving and the natural period of vibration of the brain is relatively long. Therefore, angular acceleration pulses that last several milliseconds produce the short-pulse response, and angular acceleration pulses that last nearly a full second or longer produce the long-pulse response.

5.3 Long-pulse rotational response

5.3.1 The relative contributions of the steady-state shear strain response and the transient shear strain response for angular acceleration inputs of different time-dependence shapes

For cylinders with shells that are subject to prescribed rotational acceleration pulses of long duration, the strain-response has two main components. The two main components are the steady-state response, $\varepsilon^s_{r\theta}(r,t)$ and the transient response $\varepsilon^t_{r\theta}(r,t)$.

$$\varepsilon_{r\theta}(r,t) = \varepsilon^s_{r\theta}(r,t) + \varepsilon^t_{r\theta}(r,t) \tag{5.1}$$

The steady state response component, $\varepsilon^s_{r\theta}(r,t)$, has a time-dependence that mirrors the time-dependence of the angular acceleration, $\ddot{\theta}(t)$. The other component is the transient component, which is a sum of higher frequency oscillations that can be excited by sharp changes in the shell's angular acceleration. The time-dependence shape of the angular acceleration pulse, and its duration, influence the relative magnitudes of these two components of the entire shear strain response. In this section, the responses to a bipolar rectangular angular acceleration pulse, which has $|\dot{\theta}_f| = 0$ rad/s and a relatively rapid increase in acceleration initially, and to a triangular angular acceleration pulse, which has $|\dot{\theta}_f| \neq 0$ rad/s and a relatively slow increase in angular acceleration initially, are compared, and used to identify which types of angular acceleration pulses have responses that are dominated by either the steady-state or transient component.

When a long rotational acceleration pulse is applied to the cylinder's shell, shear strain develops within the cylinder relatively slowly. In Figure 5.4a, the strain response to a triangular acceleration pulse lasting 2.5 s is plotted. Figure 5.4b shows the response to a long bipolar rectangular acceleration pulse, also lasting 2.5 s. The complex shear modulus of the cylinder is modeled with a Standard Linear Solid visco-elastic model, with the parameters $G_u = 6$ kPa, $G_r = 1.2$ kPa, and $\tau_R = 2$ ms. These values for $G_u = 6$ kPa, $G_r = 1.2$ kPa are of similar magnitude to those used in other brain mechanics studies. The relaxation time, $\tau_R = 2$ ms is somewhat lower than what is observed for human and other mammalian brains [42]. The cylinder's density is $\rho = 1000$ kg/m^3 and its outer radius, which corresponds to the inner radius of the shell, is $R_i = 0.1$ m.

The complex modulus and density of the cylinder material govern how fast a shear wave travels within the medium. Shear waves travel more slowly in media with smaller complex shear modulus and larger densities, but 2.5 s is still much longer than it takes a shear wave to travel from the outer radius to the center of the cylinder and back, in this medium. Therefore, both the triangular acceleration pulse and the bipolar rectangular pulse in Figure 5.4 have sufficiently long durations for waves to travel from the outer radius to the center of the cylinder, and back, a few times, within the time it takes for the acceleration pulse to be completed. While transient waves propagate across the cylinder, strain builds up in the interior of the cylinder. The strain that accumulates at the outer radius of the cylinder approximately mirrors the time-dependence of the rotational acceleration, especially for the triangular pulse. However, for the bipolar rectangular pulse, which has a rapid change in acceleration initially, there are noticeable additional higher amplitude transient oscillations. These dissipate over time, though, and this allows the strain to settle into proportionality with the applied angular acceleration, eventually.

5.3.2 Spatial scaling of shear strain in the steady-state solution

The difference in the spatial distribution of strain for these two types of pulses is also evident in Figure 5.5, which shows the shear strain as a function of time at four evenly-spaced points, including a point on the outer radius of the cylinder. Whether the angular acceleration pulse has a steep increase in angular acceleration initially also affects the magnitude of the shear strain throughout the cylinder. This is because the steady state response and the transient response depend on the radial position, r, in different ways.

The steady-state component of strain is due to the stress needed to accelerate the cylinder's interior to match the angular acceleration of the shell. An expression for the shear strain at a radial position, r, within the cylinder, can be obtained by analyzing that requirement. Calculating the torque about the center of mass, T, needed to accelerate the material on the interior of a given ring of material ($r' < r$) yields the shear stress that ring of material, dr. In the derivation below, $I_z^{IC}(r')$ represents the polar moment of inertia of the cylinder of material on the interior of the ring, and $\sigma_{r\theta}$ represents the shear stress on the outside surface of that cylinder. The total torque is calculated in terms of $\sigma_{r\theta}$ by integrating infinitesimal elements of torque, dT, due to the shear stress acting at a distance r from the center of mass.

$$\int dT = I_z^{IC}\ddot{\theta} \tag{5.2}$$

$$\int_0^{2\pi} r\sigma_{r\theta}r\ d\theta = \frac{1}{2}(\rho\pi r^4)\ddot{\theta} \tag{5.3}$$

$$2\pi\sigma_{r\theta} = \frac{1}{2}(\rho\pi r^2)\ddot{\theta} \tag{5.4}$$

$$\sigma_{r\theta} = \frac{1}{4}\rho r^2\ddot{\theta} \tag{5.5}$$

If the cylinder medium were an elastic material, the tensor shear strain, $\varepsilon_{r\theta}$, within the cylinder would be calculated by dividing the shear stress $\sigma_{r\theta}$ by twice the shear modulus, $2G$.

$$\varepsilon_{r\theta} = \sigma_{r\theta}/2G \tag{5.6}$$

$$= \frac{\rho r^2\ddot{\theta}}{8G} \tag{5.7}$$

The preceding analysis explains the r^2-dependence of shear strain for the steady-state strain response of the cylinder. For the triangular acceleration pulse, the transient oscillations have a relatively small amplitude, so the r^2-scaling is evident in the maximum strain observed at each point. These values are shown by the set of black markers in Figure 5.7. A dashed red line is overlaid on this to indicate this power law relationship for maximum strain and position. For the bipolar rectangular pulse, the transient has a larger magnitude relative to the steady-state component, so the r^2-scaling of the steady-state response is obscured, and the transient oscillatory response dominates the spatial distribution of the maximum strain.

5.3.3 Relaxation time and visco-elastic damping

For Figure 5.7, the cylinder medium has a relatively short relaxation time, $\tau_R = 2$ ms. There is a transition from the strain being related to the angular acceleration through the relaxed modulus to being related through the unrelaxed modulus, as the relaxation time is increased. Specifically, this transition is governed by the relative duration of the relaxation time to the other time-scales that are present, such as the loading pulse duration, and the time it takes a wave to propagate from the cylinder's outer radius to its center. This is evident in Figure 5.8, where the strain inside the cylinder with a relaxation time of 0.001 s (blue circles) approaches $\rho r^2|\ddot{\theta}|_{max}/(8G_r)$ (dashed black) and the strain inside the cylinder with a relaxation time of 1 s (purple triangles) approaches $\rho r^2|\ddot{\theta}|_{max}/(8G_u)$ (dashed black). The scaling for long relaxation times is used in Chapter VI to non-dimensionalize $\varepsilon_{r\theta}(t)$ and $\varepsilon_{r\theta}^{max}$ with respect to $|\ddot{\theta}|_{max}$.

5.4 Short-pulse rotational impacts cause shear waves to propagate

A short pulse is a pulse that has a duration that is shorter than the time it takes a stress wave to travel across the structure being loaded. A short angular acceleration pulse applied to the cylinder's shell causes a shear stress wave to propagate toward the cylinder's interior. After the loading pulse is over, this wave continues to propagate toward the center of the cylinder, and when it arrives there, it is reflected back out toward the outer radius of the cylinder. This process occurs over a longer period of time than the angular acceleration pulse takes. In this way, the angular acceleration pulse may be complete, but the cylinder is still experiencing dynamic deformation within its interior.

In this section, we will show that we can predict the overall shape of the time-dependence of the shear strain response at a location near the outer radius of the cylinder from the time-dependence of the angular velocity of the shell. Further, we can predict the amplitude of the shear wave that starts at the shell-cylinder interface during the angular acceleration pulse, using only the shear wave speed within the cylinder and the maximum change in circumferential speed of the points on the shell, even for angular acceleration pulses with different time-dependence shapes. Then, we will consider how the material properties of the cylinder govern the magnitude of the strain response, over time, as the shear wave propagates toward the center of the cylinder. With these three pieces of information, we can begin to identify which aspects of an angular acceleration pulse, brought on by an impact, are correlated most strongly with large shear strain within the cylinder.

5.4.1 The final angular speed of the shell, after the angular acceleration pulse is complete, strongly influences the time-dependence of the resulting strain response

In the short-pulse limit, the time-dependence of the strain depends on the time-dependence of the angular velocity of the shell. Even if it is the angular acceleration which is originally specified, the angular velocity that results from the prescribed angular acceleration pulse is the variable which governs the time-dependence of the shear wave that forms. It is possible to observe how the angular velocity and angular acceleration affect the shear strain by considering angular acceleration pulses with different time-dependence shapes.

In Section 4.3, four pulse shapes were described and were divided into two categories: those that produce a non-zero final angular speed of the shell, $|\dot{\theta}_f| \neq 0$, and those that bring it back to rest by the end of the pulse, $|\dot{\theta}_f| = 0$. Another way to think about this categorization is whether the angular velocity history of the shell is more similar to a step function or a delta function. Naturally, we expect the responses to these two types of loading to be quite different from each other. Both types of pulses increase the strain within the cylinder initially, but differ in how rapidly the shear strain magnitude returns to zero or attains a negative value, after this initial positive region comes to an end. When the angular acceleration pulse results in a non-zero final angular speed, the decrease in strain following the completion of the acceleration pulse is slow, and governed by the properties of the cylinder. When the angular velocity is reduced immediately after it reaches its peak value, so that the shell returns to rest as rapidly as it reached its maximum angular speed, the strain also decreases rapidly, too.

In Figure 5.9a, the triangular **acceleration** pulse causes the cylinder's shell to have a non-zero final angular speed, $|\dot{\theta}_f| \neq 0$. Specifically, in this instance, the maximum angular speed of the shell is $|\dot{\theta}|_{max} = 1$ rad/s, which can be calculated with the area under the angular acceleration-time curve, $|\dot{\theta}|_{max} = (1/2)t_0|\ddot{\theta}|_{max}$. Since the maximum angular acceleration,$|\ddot{\theta}|_{max}$, is 800 rad/s^2, and the pulse duration is $t_0 = 0.0025$ s, this gives the previously stated maximum angular speed of $|\dot{\theta}|_{max} = 1$ rad/s. The angular acceleration pulse brings the shell, which was initially at rest, up to this magnitude of angular speed, and the angular acceleration is held at 0 rad/s^2, so the shell keeps rotating at this speed, thereafter. This causes the shear strain to linger around its maximum after the angular acceleration pulse is complete. However, a bipolar rectangular pulse, which leads to a triangular **velocity** pulse, and a final angular speed of 0 rad/s, produces a strain response that returns to zero shortly after the stress wave passes by. This response is shown in Figure 5.9b. Both pulses have the same maximum angular speed, $|\dot{\theta}|_{max} = 1$ rad/s; the difference is mainly in whether the maximum angular velocity of the shell is maintained or not. If the maximum angular velocity is maintained at its maximum value in perpetuity, the input is similar to a step function in $\dot{\theta}(t)$, but if the angular velocity of the shell is rapidly decreased from the maximum value, the input is more like an impulse. Since one input is the derivative of the other, the relative contributions of high and low frequency modes will be different for these two kinds of loading. An approach to analyzing loading that looks exclusively at the maximum magnitude of the angular acceleration history may obscure both the magnitude of the maximum strain experienced within the cylinder, and the duration of time that the material spends at those high deformation levels.

This fundamental difference between pulses which have a non-zero final angular speed, and those which do not, is manifested across a range of pulse durations. In Figures 5.10a and 5.10b, the responses to an angular acceleration pulse with a non-zero final acceleration pulse are compared with the responses to angular acceleration pulses that result in the final angular speed being 0 rad/s. In these figures, pulses with several different durations are considered, and the cylinder modeled here also has slightly more damping than the one associated with Figure 5.9.

The two angular acceleration pulse shapes used for this comparison are the rectangular pulse and the bipolar rectangular pulse. This is a slightly different comparison than the one in Figure 5.9, which compared the response to a triangular angular acceleration pulse to the response to a triangular angular velocity pulse, which is identical to a bipolar rectangular angular acceleration pulse. Nevertheless, the response of the cylinder to the triangular angular acceleration pulse and its response to the rectangular angular acceleration pulse are qualitatively similar. When the final angular speed of the shell is not zero ($|\dot{\theta}_f| \neq 0$ rad/s, Figure 5.10a), the strain response for short pulses again lacks the rapid decrease seen for pulses that leave the shell at rest when they are complete ($|\dot{\theta}_f| = 0$ rad/s, Figure 5.10b). Instead, the strain increases slightly after the loading pulse is over, and stays at a relatively high value for longer, in Figure 5.10a. For these pulses, the strain pulse has approximately the same shape for the $t_p = 0.001, 0.0025, 0.0063,$ and 0.016 s pulses. The bipolar rectangular pulses, which have the same durations for the positive section of the pulse, t_p, as in Figure 5.10a, generate a different type of response. These strain pulses are approximately triangular when plotted against time, like the angular velocity, and last the same amount of time as the corresponding angular acceleration pulse lasts.

5.4.2 Initial shear strain magnitude at the outer radius of the cylinder is proportional to the reciprocal of shear wave speed and the maximum circumferential speed

The purpose of a kinematic injury criterion is to relate observable kinematic quantities to the risk of damage posed by an impact situation, so that dangerous impacts can be prevented, and if they cannot be prevented, at least identified in order to provide treatment.

Since it is known that large interior strains are damaging, knowing the parameters of impact that correlate to large strains can form the basis of a kinematic injury criterion. In the simplified head model in this chapter, it can be shown that there is a straightforward relationship between the magnitude of the shear wave that is created by rotational skull motion, and the circumferential speed of the points at the interface between the skull and brain. Although the shear wave produces different levels of strain within the cylinder as time progresses, the initial magnitude of the shear strain pulse provides a good reference from which to estimate the strain throughout the brain, and from which to measure how much the strain changes as the shear wave propagates.

It is useful to use the behavior of plane shear waves as context for the behavior of the more complicated visco-elastic shear waves that exist in the cylinder because they have some important similarities. For elastic waves, the shear strain associated with a plane wave is proportional to the particle velocity and inversely proportional to the phase velocity of a shear wave in the medium. The ratio of shear strain to particle velocity within a plane wave is calculated below:

$$\vec{u}(x,y,t) = u_y(x,t)\hat{j} \tag{5.8}$$

$$u_y(x,t) = u_0 \exp i(\omega t - kx) \tag{5.9}$$

$$\dot{u}_y(x,t) = i\omega u_0 \exp i(\omega t - kx) \tag{5.10}$$

$$\gamma_{xy}(x,t) = \frac{\partial u_y}{\partial x} + \frac{\partial u_x}{\partial y} \tag{5.11}$$

$$\gamma_{xy}(x,t) = -iku_0 \exp i(\omega t - kx) + 0 \tag{5.12}$$

$$\varepsilon_{xy}(x,t) = (1/2)\gamma_{xy}(x,t) \tag{5.13}$$

$$\varepsilon_{xy}/\dot{u}_y = -(1/2)k/\omega \tag{5.14}$$

$$\varepsilon_{xy}/\dot{u}_y = -(1/2)1/c_s \tag{5.15}$$

$$\varepsilon_{xy}/\dot{u}_y = -(1/2)\sqrt{\rho/G} \tag{5.16}$$

In the preceding derivation, x is the coordinate in the direction of wave propagation, y is the perpendicular component, t is time, u_y is the displacement perpendicular to the direction of wave propagation, $\dot{u}_y$ is the particle velocity, u_0 is the amplitude of the wave, ω is the frequency of the plane wave, k is the wave number, γ_{xy} is the engineering shear strain, c_s is the phase velocity of the wave, ρ is the density of the medium, and G is the shear modulus of the medium.

The amplitude of a visco-elastic plane wave is more complicated than that of an elastic wave, since the frequency content of the strain response governs how it propagates and attenuates. A more rigorous discussion of the propagation of plane visco-elastic waves can be found in [8]. However, in the context of brain injury, an approximate treatment is acceptable in justifying the choice of parameters used as the basis for scaling laws that are obtained using the rigorous model outlined in the previous chapter. It is noted here that since the relaxation time of the brain is on the order of 0.01 s to 1 s, there is little need to consider the behavior of waves in media with relaxation times that are more than one order of magnitude outside this range. Relaxation times that are dramatically shorter than the angular acceleration pulse duration and the time it takes a shear wave to travel across the brain would produce waves that behave somewhat differently than those that evolve in the brain. The behavior of the brain during impact is the focus of this analysis, so the range of relaxation times used here will be constrained to those which are at least one-third the duration of relatively short head impacts, which last about 3 ms. This limits the influence of G_r on the cylinder response, and allows for the use of G_u as the primary model parameter defining the stiffness of the visco-elastic material, during rapid impacts.

The cylindrical geometry of the model being studied here provides a clear link between the angular velocity of the shell, $\dot{\theta}(t)$, and the circumferential speed of the material at the outer radius of the cylinder, that generates the shear waves within the cylinder. This relation can be obtained by taking the time-derivatives of both sides of Equation 4.1, anf then taking the appropriate magnitudes. The circumferential speed of the points on the outer radius of the cylinder is analogous to the particle velocity of the elastic shear plane wave. The cylindrical geometry makes calculating how the shear wave propagates a more complicated problem than the propagation of a plane wave, but initially, they are quite similar.

Specifically, the magnitude of the shear wave created by rotating the cylinder's shell follows a similar scaling to that of the strain in elastic plane waves. The maximum of the magnitude of the shear strain at the outer radius of the cylinder, in the time during the application of the angular acceleration pulse, is denoted with the symbol $\varepsilon^*_{r\theta}$. It is approximately equal to the ratio of the circumferential speed of the points on the outer radius of the cylinder, $|\dot{u}_\theta|_{max}$, to the square root of the unrelaxed shear modulus divided by the density, $\sqrt{G_u/\rho}$. Therefore, as with the elastic plane wave, the material properties of the visco-elastic cylinder also play a role in the defining the magnitude of the shear wave, though it is not as precise a relationship.

The exact proportionality between the unrelaxed shear modulus of the cylinder, the density of the cylinder, and the circumferential speed of the points on the outer radius of the cylinder, for angular acceleration pulses of different shapes and cylinders with a few different relaxation times, is shown in Figures 5.6a and 5.6b. Figure 5.6a is for sinusoidal pulses of two durations ($t_0 = 0.001$ s and $t_0 = 0.01$ s) and three different relaxation times ($\tau_R = 0.01, 0.0316, 0.1$ s). The density of the medium is 1000 kg/m^3. The dotted grey lines represent the scaling between the shear modulus and the shear strain for an elastic plane wave, with the shear modulus being the same as the unrelaxed shear modulus listed on the x-axis, and the corresponding magnitude of particle velocity.

The sine pulse is used to show this correlation because it varies smoothly, and generates a comparably smooth circumferential speed history for the points on the outer radius of the cylinder. Further, this type of angular acceleration pulse produces a final angular speed of 0 rad/s after the angular acceleration is complete, which has the affect of reducing the influence of the relaxation time on the amount of strain. The result of this is that the strain response that is generated is also smoothly increasing and therefore does not produce spatially narrow response features that require a fine spatial discretization to resolve. The sine pulse and half sine pulse are also commonly used forms for acceleration in other studies of brain deformation due to skull motion. For example, the sine pulse shape is used in [25] and [21]. Figure 5.6b shows the corresponding result for a single rectangular acceleration pulse. The relation between the unrelaxed shear modulus, density, and circumferential speed of the points on the outer radius of the cylinder, is more approximate in this case than it is for an elastic plane wave or for the sine pulse. Nevertheless, this is a relatively robust result showing that the initial magnitude of the wave is roughly proportional with the maximum of the magnitude of the angular velocity.

In Figure 5.6b, the initial strain for the cylinder with $\tau_R = 0.01$ s and G_u below 3 kPa is above the grey line for Equation 5.16. This may be due to the shorter relaxation time causing the visco-elastic material to respond with a stiffness noticeably lower than the unrelaxed shear modulus G_u. This lower stiffness results in shear strain values that are higher than for other relaxation times.

5.5 Propagation and attenuation

Once the wave is created at the shell-cylinder interface, it propagates into the interior of the cylinder. Since the medium is visco-elastic, the wave will be dissipated the longer and farther it travels. The exact amount that the shear strain attenuates as the shear wave propagates depends on the amount of dissipation that the material performs. The amount of dissipation the cylinder medium performs depends on the frequency content of the shear wave, and how much that spectrum overlaps with the vibration frequencies the material damps well. The speed with which the strain wave travels also depends on the frequency content of the strain pulse and the properties of the medium. If the strain pulse has mainly low frequency content, it will propagate more slowly than a pulse with mainly high frequency content. The dissipation of the shear wave has important consequences for the maximum strain that is attained at different regions within the cylinder.

5.5.1 Wave attenuation depends on the material properties of the cylinder

Figure 5.11 contains plots of the strain inside deforming cylinders under different conditions, specifically two different relaxation times and two different pulse durations, for a bipolar rectangular angular acceleration pulse. Figure 5.11a and Figure 5.12b are for cylinders with relatively low damping, due to a relaxation time of 0.1 s, which is somewhat longer than the pulses considered, and of the same order as the time it takes a shear wave to travel from the shell to the center of the cylinder. Figure 5.11c and Figure 5.11d are for a cylinder with higher damping, due to a relaxation time of 0.01 s, which is shorter than for Figure 5.11a and Figure 5.11b. Experimentally obtained values for the relaxation time of the brain and those used in finite element simulations vary over a few orders of magnitude [33, 37, 42], but the exact amount of damping the brain achieves is not fully characterized, so we have considered two plausible values of relaxation time for modeling the relaxation behavior of the brain.

Four positions within the cylinder are considered. These points are evenly spaced along the path toward the center of the cylinder, from the outer radius. The low damping for the 0.1 s relaxation time results in strain waves that propagate across the cylinder repeatedly before they damp out, as is visible in Figure 5.11a and Figure 5.11b. The strain associated with the shear wave increases as it propagates toward the middle of the the cylinder, especially in Figure 5.11a. In contrast, the cylinder with the shorter relaxation time, $\tau_R = 0.01$ s, damps the strain response more rapidly, both in space and time, shown in Figure 5.11c and Figure 5.11d. As the shear wave propagates toward the interior of the cylinder, the magnitude of the strain associated with the wave passing by a particular radial location decreases.

In Figure 5.12, a wider range of scenarios is considered, and attention is focused on the magnitude of the strain at the outer radius of the cylinder. Figure 5.12c and Figure 5.12e show the shear strain due to bipolar rectangular angular acceleration pulses, which have the shape shown in Figure 5.12a. Figure 5.12d and Figure 5.12f are for single rectangular pulses, of the form shown in Figure 5.12b. All the angular acceleration pulses result in a maximum angular speed $|\dot{\theta}|_{max} = 10$ rad/s.

The lack of damping of the strain in Figure 5.12d reduces the amount the wave attenuates, so the magnitude of the wave is still high when it returns to the outer radius of the cylinder, after reflecting off the center of the cylinder, located at $r/R_i = 0$. The reflection of the wave by the interface between the shell and the cylinder, at the cylinder's outer radius, $r = R_i$, produces high shear strain at that location temporarily. This is especially significant for the two shorter pulses, $t_0 = 0.0025$ s and $t_0 = 0.0063$ s, and those scenarios produce the highest shear strain of all the scenarios considered here. However, the shorter relaxation time, $\tau_R = 0.01$ s, which is associated with better damping, also causes the cylinder material to respond with more compliance. This results in $t_0 = 0.016$ s pulses and $t_0 = 0.04$ s pulses, for both the rectangular pulse shape and the bipolar rectangular pulse shape, leading to higher maximum strains than are seen with the larger relaxation time, $\tau_R = 0.1$ s. In Figure 5.12e, the maximum shear strains for the longer two pulses are larger than in Figure 5.12c, and the maximum shear strains for the longer two pulses in Figure 5.12f are larger than in Figure 5.12d. Therefore, we see that the increased damping from a smaller relaxation time, $\tau_R = 0.01$ s, reduces the maximum strain for shorter pulses but increases the maximum strain for longer pulses. Incorrect estimates of relaxation time of the brain will the produce a bias in the predicted performance of helmets that produce either longer or short impacts. If, for instance, a proposed design produces a relatively long-duration impact, on the order of 16 ms, but the brain model uses a relaxation time which is too short, then the prediction of strain during the impact will be over-estimated and the performance of the helmet consequently under-estimated.

5.5.2 Geometry focuses strain in the middle; visco-elastic damping can compensate for this.

In some circumstances, the strain at the interior of the cylinder can be much higher than at the exterior, as is seen in Figure 5.11a. In general, this increase in strain at smaller radial coordinates occurs when the cylinder medium does not damp out the transient component of the shear strain, and the pulse has a sufficiently short duration. In Figure 5.11a, four radial locations were considered, but a more finely resolved picture of the spatial dependence of the maximum shear strain is necessary for drawing broader conclusions about the propagation and attenuation of shear waves in compliant cylinders.

Figure 5.13 depicts the maximum shear strain at a range of radial positions within the cylinder. Each plot corresponds to a different loading pulse duration ($t_0 = 0.001$ and 0.01 s) and contains results for four different relaxation times ($\tau_R = 0.001, 0.01, 0.1, 1.0$ s).

Since both pulses are significantly shorter than the time it takes a shear wave to travel from the edge of the cylinder, a shear strain pulse forms at the place where the cylinder connects to the shell, and propagates into the middle of the cylinder over time. For the three longer relaxation times $\tau_R = 0.01, 0.1, 1.0$ s, the initial magnitude of the shear strain pulse is approximated by Equation 5.16. The initial magnitude is higher for $\tau_R = 0.001$ s because the visco-elastic medium creeps when the relaxation time is shorter than, or of the same order as, the angular acceleration pulse duration.

For the cylinders with the two longer relaxation times, $\tau_R = 0.1$ s and $\tau_R = 1$ s, the maximum shear strain distributions have slight peaks at the larger radii, near the interface of the cylinder and shell. There is also a local maximum near the center of the cylinder, $r/R_i = 0$, though the peak near the middle has a higher relative magnitude and is closer to the center, for the shorter pulse, than for the longer pulse. These interior maxima are due to the circular geometry of the cylinder concentrating the shear waves at the center of the cylinder. For the relaxation time in the intermediate range ($\tau_R = 0.01$ s) the cylinder has a nearly constant maximum shear strain what the shorter pulse is applied. For the slightly longer pulse, there is a decrease in the maximum shear strain farther into the interior of the cylinder. In this case, the maximum shear strain over the whole cylinder is attained at the outer radius of the cylinder in both cases. With the shortest relaxation time considered here, $\tau_R = 0.001$ s, the maximum shear strain is observed at the the outer radius of the cylinder, with the maximum shear strain monotonically decreasing farther into the cylinder interior. The two shorter relaxation times are associated with cylinder media which have higher critical damping frequencies, and dissipate energy more effectively at the frequencies which compose the angular velocity pulses than do the media with longer relaxation times. Therefore, in this situation, it can be seen that the dissipation of a shear wave by a medium with the critical damping frequency suitably close to the frequencies of the traveling shear wave can mitigate the focusing affects of the circular geometry.

5.5.3 Conclusions

In this chapter, many features of the short-pulse response and the long-pulse response of a cylindrical rotating delicate object were identified. This enumeration of the qualitative aspects of the response of a compliant cylinder enclosed within, and connected to, a rotated rigid shell, enables an informed discussion of the the quantitative response of this cylinder. In the next chapter, this background will be used to explain why certain scaling laws emerge, based on the overall categories of response that can be observed under different circumstances. We also introduced some quantitative results associated with the magnitude of the transient wave initiated by short angular acceleration pulses and the the spatial distribution of strain within the steady state response. These facilitate making meaningful choices for the dimensionless groups used in the next chapter.

The behavior of cylinders loaded with long pulses is consistent with the concept of the long-duration response presented by Kornhauser and Lawton. The discussion of the long pulse response identified two main components of the shear strain field: the transient mode excited by sharp increases or decreases in angular acceleration, and the steady state response. Although the presence of the transient oscillations increase deformation with respect to the steady-state response, these oscillations are relatively small for the triangular pulse. The steady-state strain field is proportional with the magnitude of the rotational acceleration, the square of the radius, and the density. When the relaxation time of the medium is small compared to the other time-scales, the strain will be proportional with the reciprocal of the relaxed shear modulus. Otherwise, the strain will approach proportionality with the reciprocal of the unrelaxed modulus for increasingly longer relaxation times. These are the relaxed and unrelaxed limits for the steady-state response.

The consideration of the short-pulse response indicates that short angular acceleration pulses generate shear strain pulses with time-dependence that is most similar to the time-dependence of the angular velocity of the shell. When the angular acceleration pulse leaves the final angular speed of the shell above 0 rad/s, the resulting shear strain at the outer radius of the cylinder rises quickly and decays relatively slowly. When the angular acceleration pulse increases the angular speed but then reduces it to 0 rad/s, the shear strain at the shell both increases and decreases rapidly, over the same time-scale as the pulse duration. Therefore, kinematic brain injury criteria should not neglect to incorporate the effects of the overall time-dependence shape of the angular acceleration pulse; whether the angular velocity remains high after the non-zero part of the angular acceleration pulse is over governs the amount of time that high shear strains persist within the brain.

Although the time-dependence of the shear strain within the cylinder is heavily dependent on the angular acceleration pulse shape, the initial magnitude of the strain wave generated at the shell is relatively insensitive to it, and instead depends mainly on the maximum angular velocity of the shell, and the shear wave speed within the medium. The maximum angular velocity of the shell produces circumferential motion of the outer radius of the cylinder, and this rapid motion causes a shear wave to form. The influence of relaxation time on the initial magnitude of this shear wave is generally negligible, as long as the relaxation times considered are sufficiently large compared to the pulse duration. However, relaxation time does influence the amount of damping within the cylinder. More damping is associated with waves being attenuated as they propagate, resulting in lower strains within the interior of the cylinder and lower maximum shear strain at the exterior. Relatively low damping results in the shear strain increasing farther within the cylinder.

In the next chapter, it will be shown how the behaviors identified in this chapter, for the short-pulse and long-pulse limits, underpin the scaling laws that describe the shear strain response of cylinders rotated at different rates, over a range of time-scales.

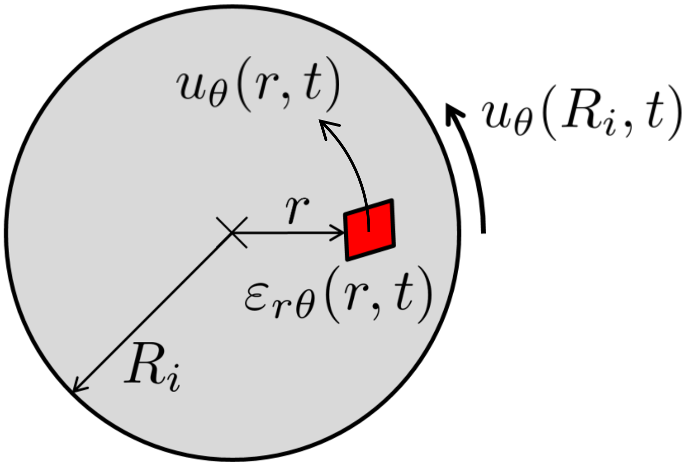

Figure 5.1: Diagram of circumferential displacement and shear strain in rotational impacts. The rotation of the outer shell (not shown) about its center produces circumferential motion of the outer radius of the cylinder, $u_\theta(R_i, t)$. The circumferential displacement of points within the cylinder, $u_\theta(r, t)$, are driven by the motion at the outer radius of the cylinder. Radial variation in the $u_\theta(r, t)/r$ field produces the radial-circumferential strain field, $\varepsilon_{r\theta}(r, t)$.

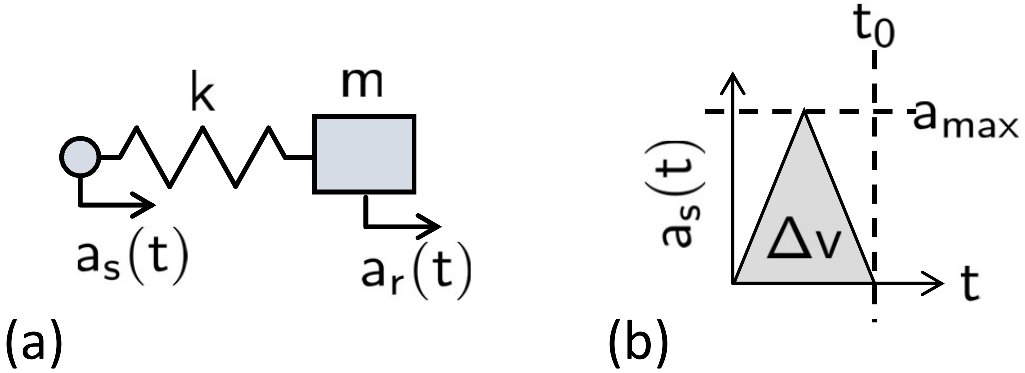

Figure 5.2: A simple lumped parameter model of a delicate object surrounded by a rigid shell, composed of a spring, mass, and excitation point, experiences internal loads when the excitation point is accelerated a prescribed amount, $a_s(t)$. (a) Diagram of the spring-mass representation of a delicate object that is adhered to a rigid shell. The rigid shell is forced to follow the acceleration history $a_s(t)$, which causes the mass to accelerate by the amount $a_r(t)$. The excursion of the spring, which is proportional with $a_r(t)$, represents the stress or strain within the delicate. (b) Two important parameters that describe the acceleration pulse, $a_s(t)$, are the maximum of the magnitude of the acceleration, a_{max}, and the magnitude of the velocity change, Δv.[23]

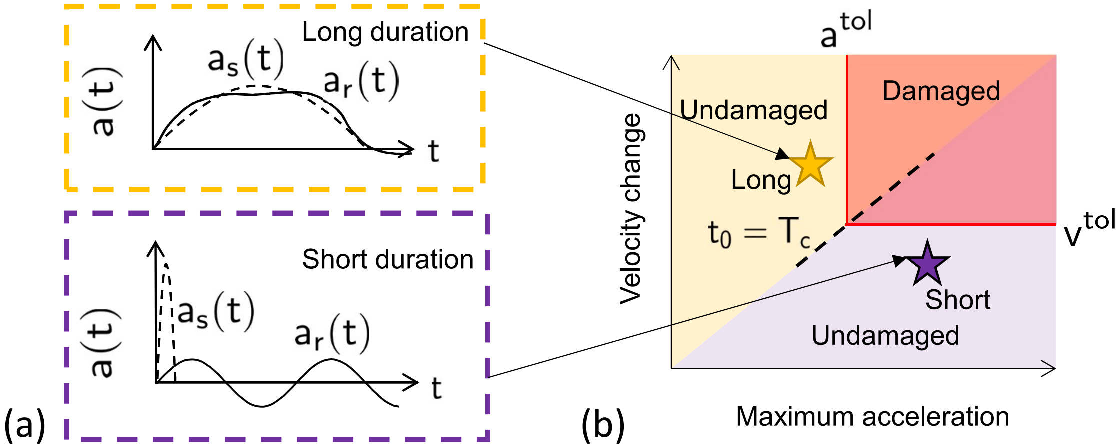

Figure 5.3: Kinematic injury criteria regimes for a simple lumped parameter model are differentiated by impact duration. (a) Short impacts have short-duration acceleration pulses and responses that are delayed with respect to the completion of the acceleration pulse. Long-duration impacts have responses that match the time-dependence of the acceleration pulse. (b) If exceeding a maximum tolerable level of stress or strain leads to damage, then damage may also be detected with an acceleration and velocity tolerance, a^{tol} and v^{tol}, respectively, which are related by the critical impact duration, T_c. If a short acceleration pulse results in a change in speed that exceeds to the tolerance of the delicate object, damage occurs. If the acceleration pulse duration is longer than the critical time T_c, then an acceleration tolerance is more appropriate. [23]

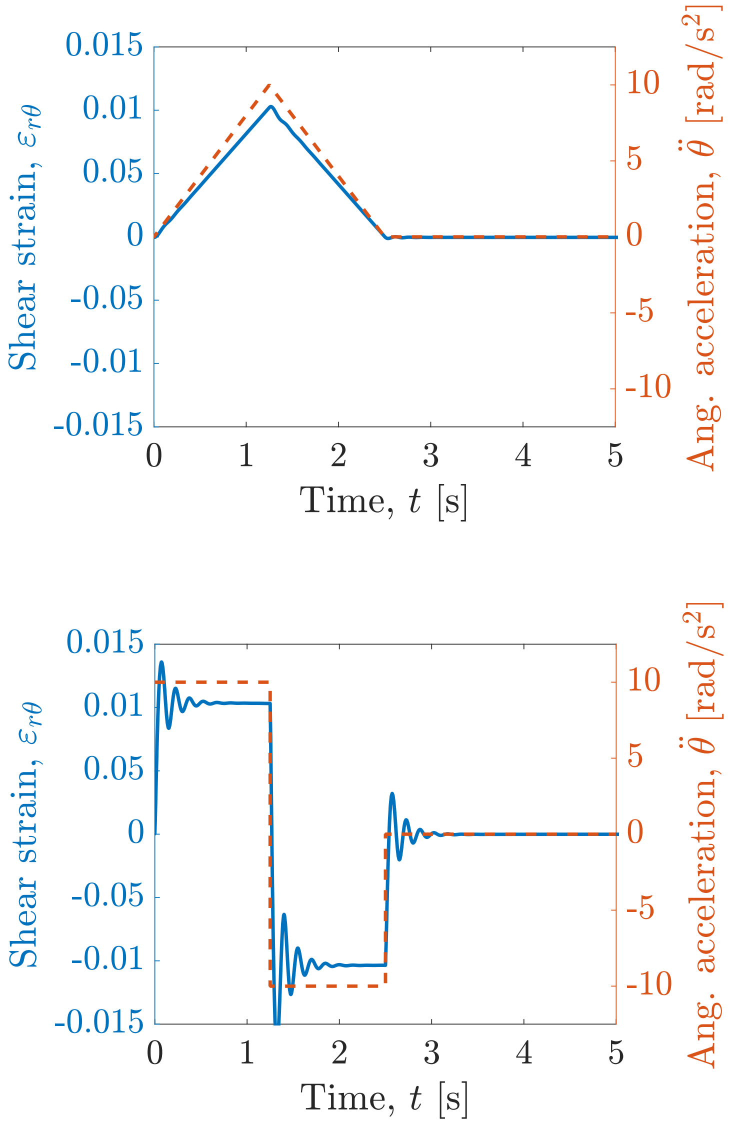

(a)

(b)

Figure 5.4: Shear strain at the shell of a rotating cylinder for two types of prescribed angular acceleration pulses. The cylinder has the properties $G_u = 6$ kPa, $G_r = 1.2$ kPa, $\rho = 1000$ kg/m^3, $R_i = 0.1$ m, and $\tau_R = 2$ ms. a.) Tangential acceleration a_T, and shear strain due to a triangular angular acceleration pulse with $|\ddot{\theta}|_{max} = 10$ rad/s^2. The blue curve is the shear strain history at a point just inside the cylinder, near the interface with the shell, at $r = R_i$. The orange curve is the tangential acceleration applied to the shell. The tangential acceleration of the points on the shell can be converted to the angular acceleration of the shell by dividing by the radius of the cylinder, $R_i = 0.1$ m. The time-dependence of the shear strain mirrors that of the angular acceleration. b.) For a prescribed angular acceleration pulse with a sharp increase at its leading edge, a transient mode is visible, but the steady-state solution emerges after the transient has dissipated. The strain levels off to the same maximum value that is seen briefly in the triangular pulse case in (a).

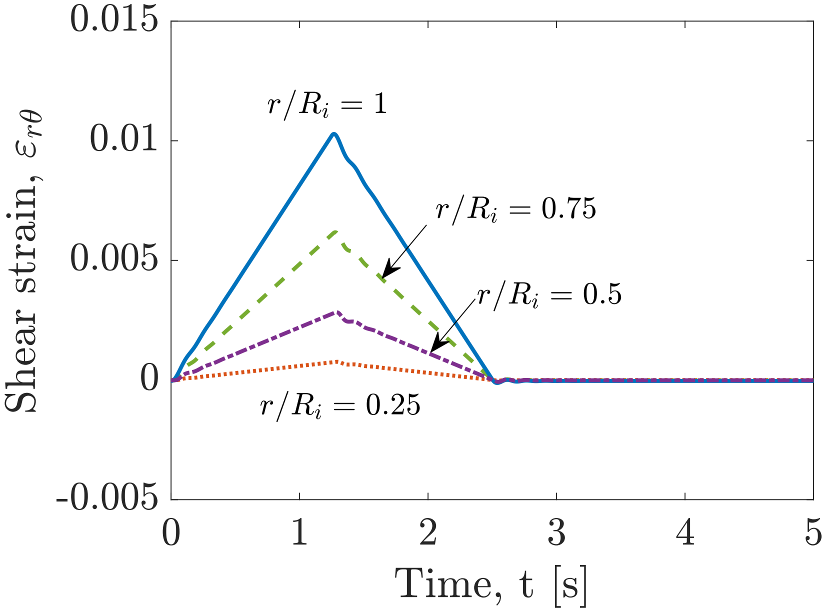

(a)

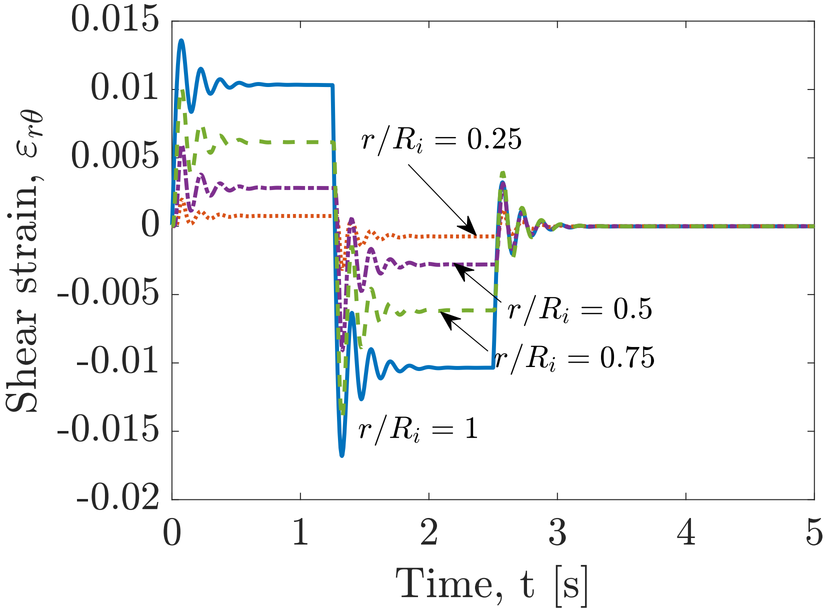

(b)

Figure 5.5: Shear strain at several points within a cylinder as a function of time for acceleration pulses with magnitude $|\ddot{\theta}|_{max} = 10$ rad/s^2 and duration $t_0 = 2.5$ s. Strain decreases with smaller dimensionless radial coordinate, r/R_i. a.) For the triangular acceleration pulse, the time-dependence of the strain within the interior of the cylinder is closely proportional with the rotational acceleration of the shell, with relatively small transient perturbations. b. For the bipolar rectangular pulse, the steady-state magnitudes of the strain depend on the acceleration, but the transient oscillations are larger than for the triangular acceleration pulse.

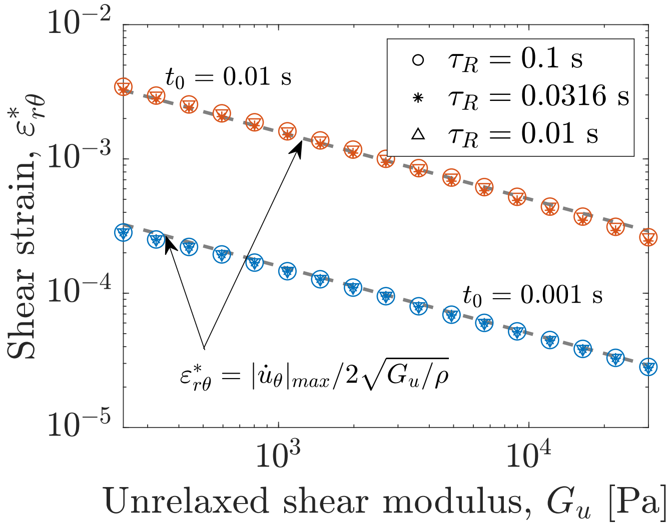

(a)

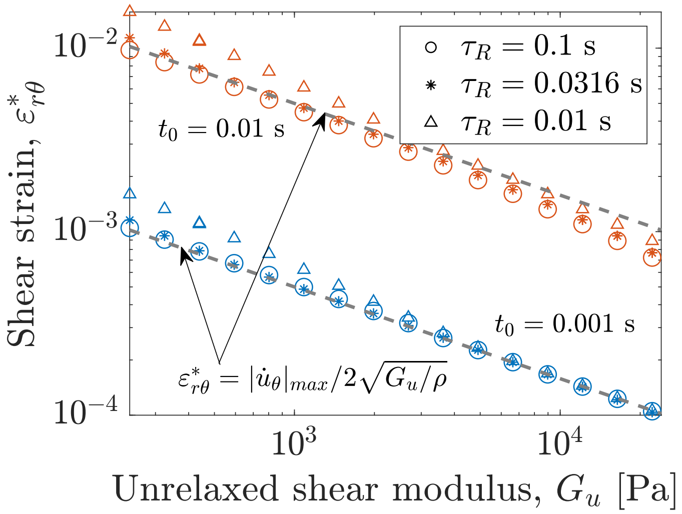

(b)

Figure 5.6: Maximum shear strain at the outer radius of the cylinder during the loading pulse, as a function of unrelaxed shear modulus for cylinders that have different relaxation times ($\tau_R = 0.01$ s indicated with triangles, $\tau_R = 0.0316$ s indicated with asterisks, and $t_d = 0.1$ s indicated with circles). The amplitude of the shear wave generated at the outer radius of the cylinder is approximately $\varepsilon^*_{r\theta} = |\dot{u}_\theta|_{max}/2\sqrt{G_u/\rho}$, where $|\dot{u}_\theta|_{max}$ is the maximum circumferential speed of the points on the outer radius of the cylinder. Pulses of two different durations ($t_0 = 0.001$ s in blue, $t_0 = 0.01$ s in orange) are considered. Cylinder parameters: $G_r/G_u = 0.2$, $R_i = 0.1$ m, $\rho = 1000$ kg/m^3. (a) Sine pulse with magnitude $|\ddot{\theta}|_{max} = 10$ rad/s^2, and $|\dot{u}_\theta|_{max} = 0.000318$ m/s for the $t_0 = 0.001$ s pulse, and 0.00318 m/s for the $t_0 = 0.01$ s pulse. (b) Single rectangular pulse with $|\ddot{\theta}|_{max} = 10$ rad/s^2, and $|\dot{u}_\theta|_{max} = 0.001$ m/s for the $t_0 = 0.001$ s pulse, and 0.01 m/s for the $t_0 = 0.01$ s pulse.

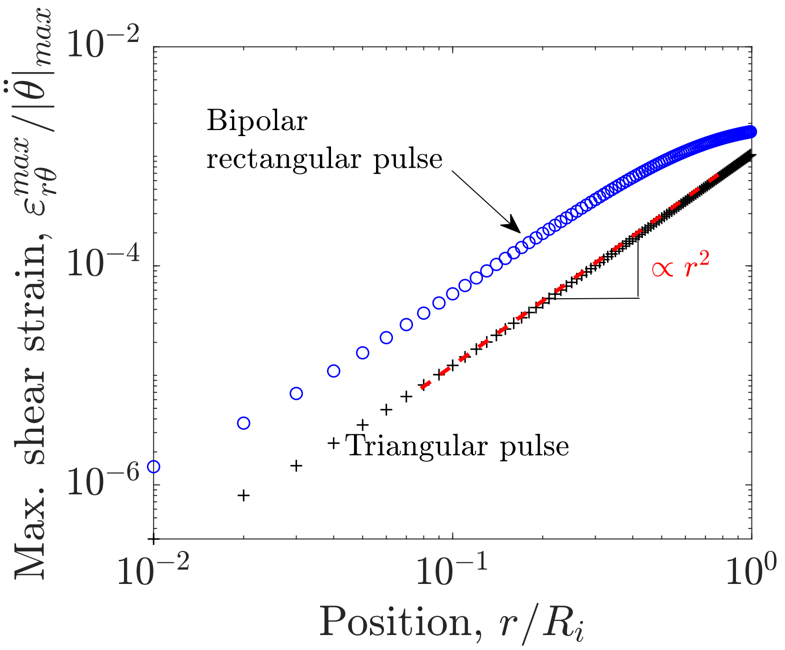

Figure 5.7: The maximum absolute value of the shear strain, normalized with the maximum angular acceleration of the shell, as a function of position within the cylinder for two types of acceleration pulses. The triangular acceleration pulse results in strain maxima that approximate the steady-state value given in Equation 5.7. However, for the bipolar rectangular pulse, the maximum strain value has a relatively large contribution from the transient oscillations, and does not follow the same r^2 scaling as the triangular pulse does.

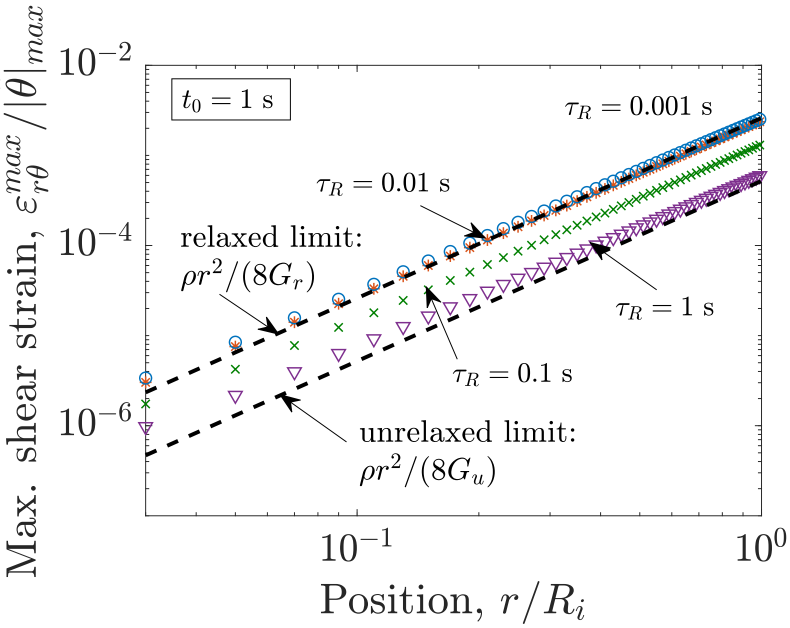

Figure 5.8: Maximum shear strain as a function of position for four cylinders with different relaxation times, for a triangular angular acceleration pulse with a duration of $t_0 = 1$ s. All four cylinders have $G_r = 1.2$ kPa and $G_u = 6$ kPa, and have different relaxation times, $\tau_R = 0.001, 0.01, 0.1, 1.0$ s. As the relaxation time increases, the maximum strain transitions from the relaxed to the unrelaxed limit, both of which are indicated with dashed black lines.

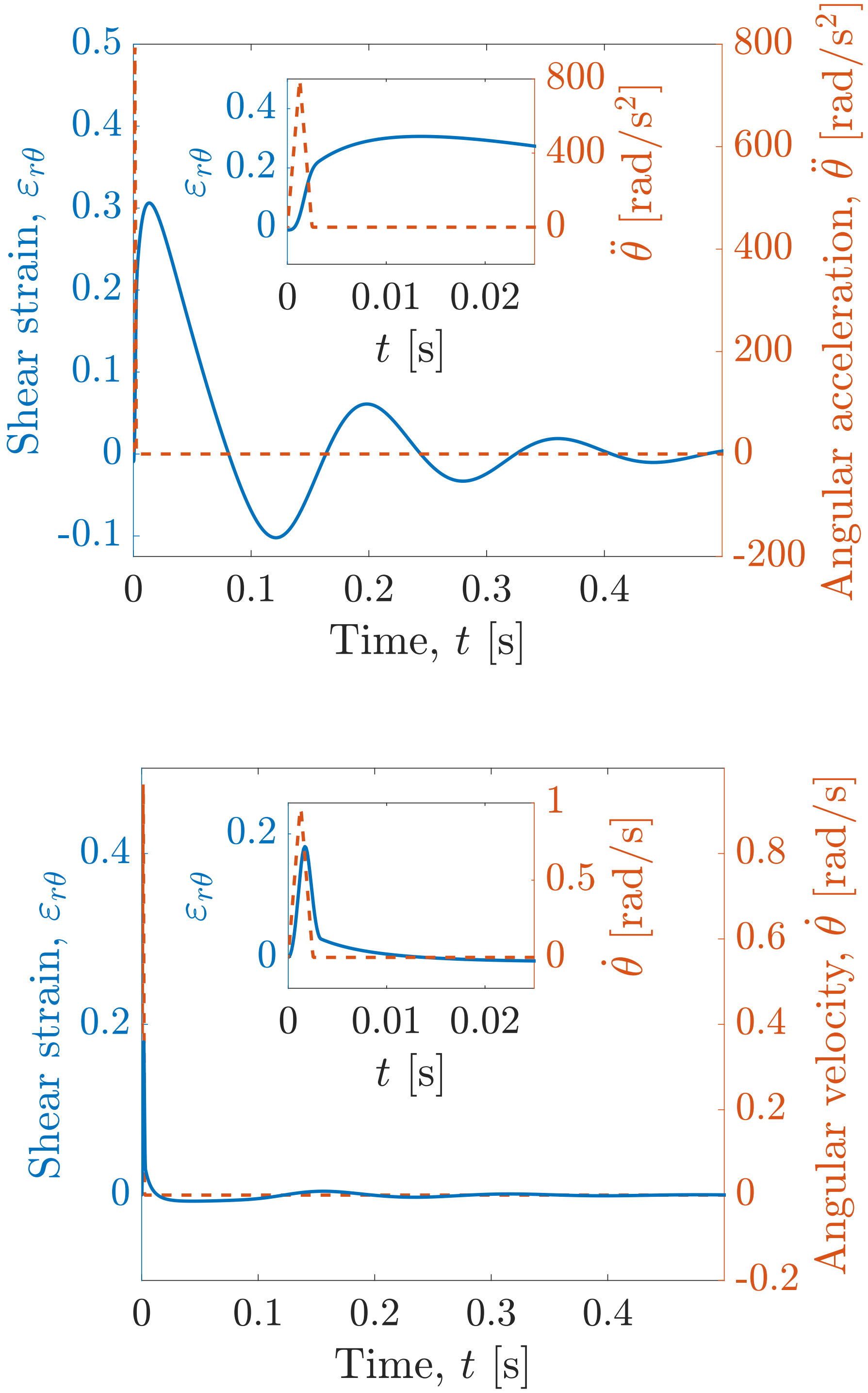

(a)

(b)

Figure 5.9: Shear strain due to a triangular angular acceleration pulse and a triangular angular velocity pulse. (a) Shear strain at the shell as a function of time for a 0.0025 s triangular angular acceleration pulse, which generates an angular velocity history that is like a step function. (b) Shear strain at the shell as a function of time for a 0.0025 s triangular angular velocity pulse, which is like an impulse. A triangular angular velocity pulse is analogous to a bipolar rectangular angular acceleration pulse.

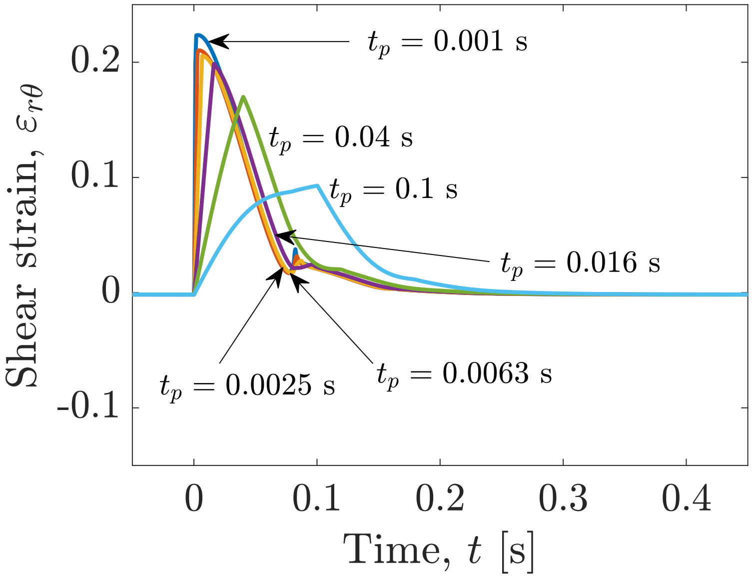

(a)

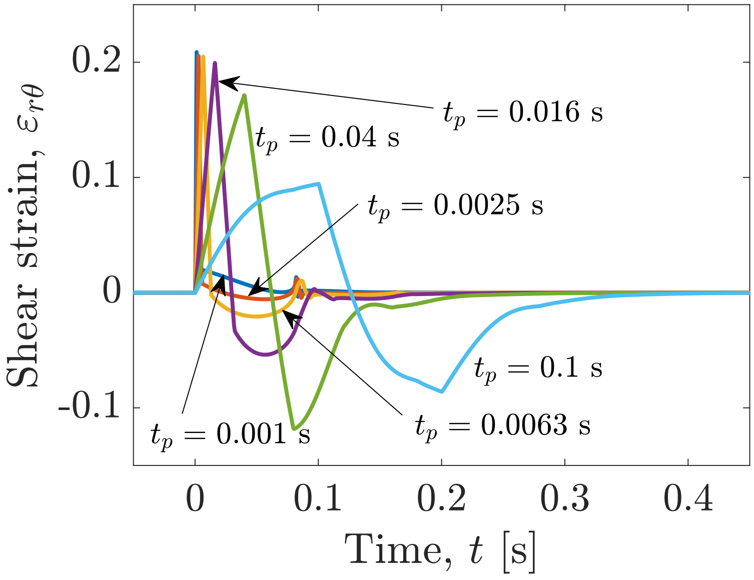

(b)

Figure 5.10: Shear strain as a function of time for six angular acceleration pulses with different durations, t_p. $G_r/G_u = 0.2, G_u = 6$ kPa, $\tau_R = 0.01$ s, $R_i = 0.1$ m, $\rho = 1000$ kg/m^3, $\Delta v = 1$ m/s (tangential). (a) Pulse shape: Single rectangular pulse. The angular acceleration pulse produces a non-zero final angular speed, that persists after the loading pulse is complete. The resulting shear strain response decreases slowly as a result. (b) Pulse shape: bipolar rectangular pulse. The angular acceleration pulse returns the angular speed of the shell back to 0 rad/s at the end of the pulse. The resulting shear strain response decreases rapidly as a result of the rapid decrease in angular velocity needed to bring the shell back to rest.

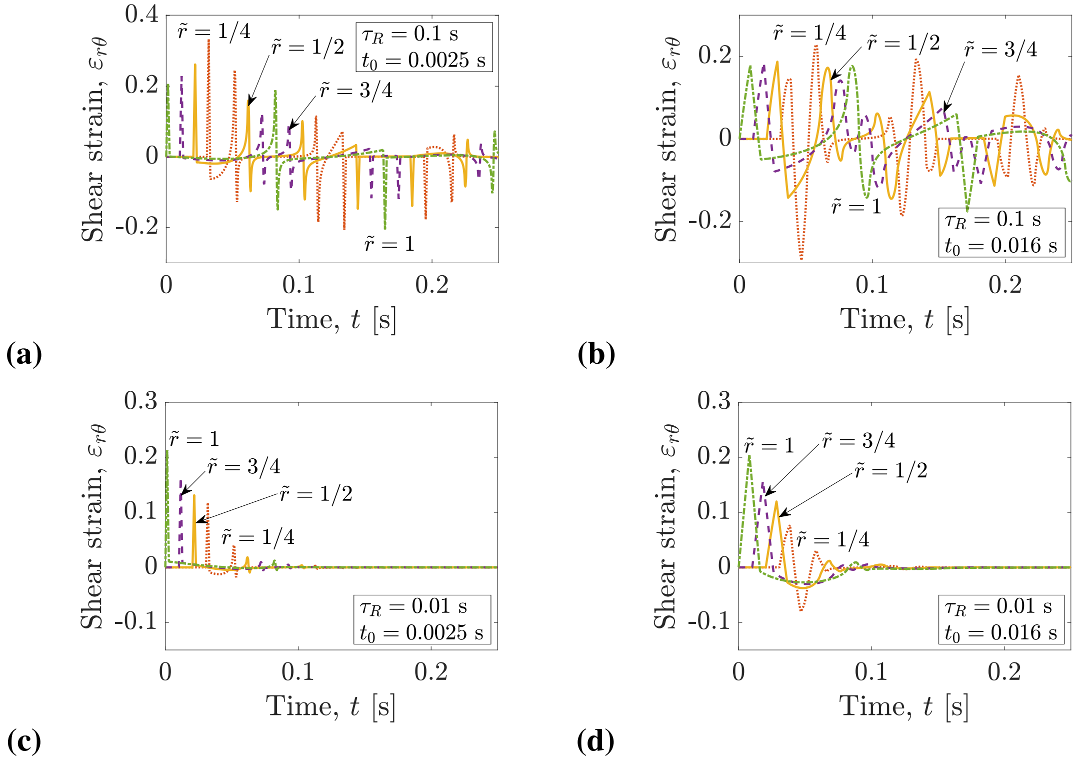

Figure 5.11: Shear strain at four points on the interior of cylinders with two different relaxation times τ_R, as a function of time t. Bipolar rectangular angular acceleration pulses of two different duration were applied. $G_r/G_u = 0.2, G_u = 6$ kPa, $R_i = 0.1$ m, $\rho = 1000$ kg/m^3, $\Delta v_{max} = 1$ m/s. (a), (c): $t_0 = 0.0025$ s. (b), (d): $t_0 = 0.016$ s. (a), (b): $\tau_R = 0.1$ s. (c), (d): $\tau_R = 0.01$ s

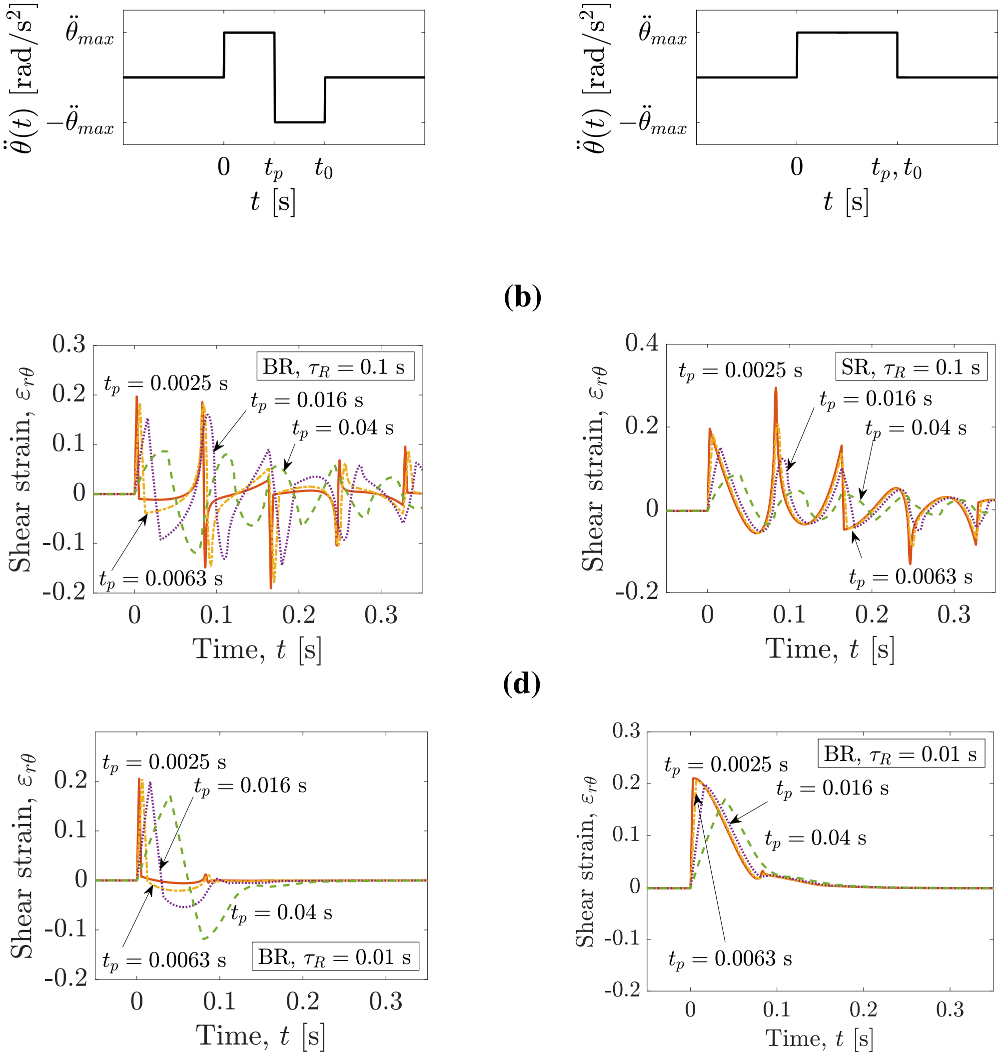

(a) **(b)**

(c) **(d)**

(e) **(f)**

Figure 5.12: Shear strain within cylinders with two different relaxation times τ_R, as a function of time t, for pulses of different durations t_0, and shapes (e.g. bipolar rectangular pulse, single rectangular pulse). $G_r/G_u = 0.2, G_u = 6$ kPa, $R_i = 0.1$ m, $\rho = 1000$ kg/m^3, $\Delta v_{max} = 1$ m/s. (c), (e): (bipolar rectangular) $|\dot{\theta}_f| = 0$. (d), (f): (single rectangular) $|\dot{\theta}_f| = 10$ rad/s. (c), (d): $\tau_R = 0.1$ s. (e), (f): $\tau_R = 0.01$ s

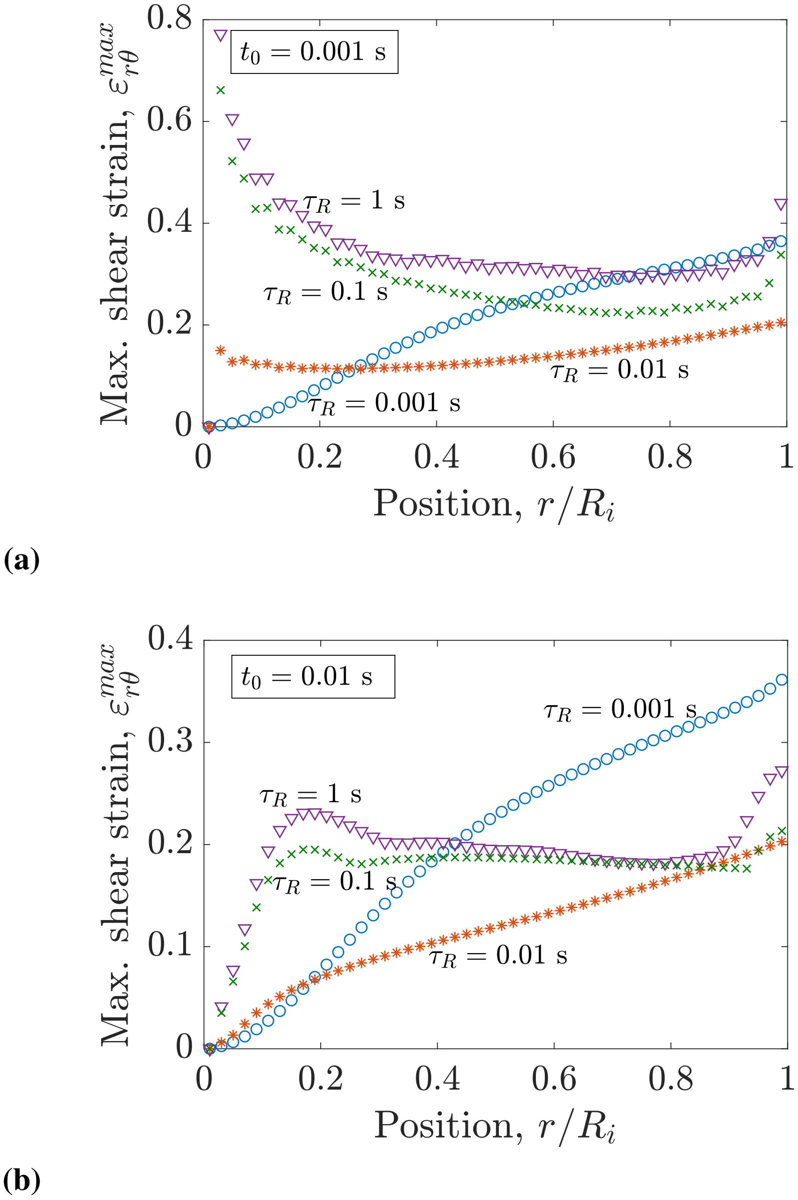

Figure 5.13: Maximum shear strain as a function of position for triangular acceleration pulses on four cylinders with different materials. All four materials have $G_r = 1.2$ kPa and $G_u = 6$ kPa. They have different relaxation times, $\tau_R = 0.001, 0.01, 0.1, 1.0$ s. (a) $t_0 = 0.001$ s. The $\tau_R = 0.1, 1$ s curves are examples of pulse-cylinder combinations for which the maximum strain is attained on the interior because the material is not very dissipative and the pulse duration is short. For $\tau_R = 0.001, 0.01$ s, there is sufficient dissipation. (b) $t_0 = 0.01$ s. For $\tau_R = 0.1$ s the maximum strain is highest on the exterior, but also has a local peak close to the center of the cylinder. The attenuation of the strain pulse as it propagates prevents the maximum shear strain on the interior from exceeding the maximum shear strain at the exterior.

CHAPTER VI

Scaling laws for predicting maximum strain using kinematic quantities

This chapter uses the principles from the previous chapter to compare the responses of different cylinders to pulses of different durations and shapes, in order to identify scaling laws that relate maximum shear strain to kinematic quantities. The maximum shear strain at each location within the cylinder is addressed first. Then, we consider the maximum shear strain across the entire cylinder. Trends in how this whole-cylinder maximum shear strain relates to pulse duration and the cylinder's level of damping are discussed last. Therefore, generalizations about the range of impact durations and material property combinations that each scaling law applies to are included in both the discussion of the local maximum strain and the whole-cylinder maximum strain. This is because the realms of applicability of scaling laws are an essential component of their use. For instance, we should not try to use scaling laws that only apply to short impacts to describe long impacts, and vice versa.

Knowing how strain magnitude scales with different descriptors of the motion of the shell enclosing the cylinder is helpful in identifying which aspects of an impact should be altered to protect this class of delicate objects. This is not altogether different from the work of reconstructing impacts using recordings of skull motion, but this work attempts to systematically probe a wider domain of impact conditions than most reconstruction studies do, and with less reliance on what impacts currently occur than is typical. Instead, this analysis leans toward the consideration of both common collisions and those with unusually short and long durations. Additionally, the use of dimensionless groups in the scaling laws produces conclusions that are independent of particular choices of stiffness parameters for the delicate object, and therefore still of use, even when some of the relevant quantities are known only approximately.

6.1 Identification of scaling laws for maximum shear strain

Three scaling laws that govern the maximum shear strain experienced at each radial position within the cylinder, $\varepsilon_{r\theta}^{max}(r)$, have been identified. Which scaling law applies depends on the pulse duration, the position being considered, and the material properties of the cylinder. For a single cylinder, which has fixed material properties and size, there are critical pulse durations and critical radii that delineate the regimes for the applicability of different scaling laws.

One way to depict these scaling laws is through showing the dependence of maximum shear strain, $\varepsilon_{r\theta}^{max}$ on different parameters. Alternatively, the dimensionless form of this quantity, derived with properties of the cylinder, and the maximum magnitude of the angular acceleration, $|\ddot{\theta}|_{max}$, can be used. One way to non-dimensionalize the maximum shear strain is

$$e^* = \frac{\varepsilon_{r\theta}^{max} G_u}{|\ddot{\theta}|_{max} \rho R_i^2}. \tag{6.1}$$

Figure 6.1 depicts the dependence of this dimensionless maximum shear strain, e^*, at the radial position $\tilde{r} = 1/4$, on dimensionless pulse duration, $\tilde{t}_0$. The dimensionless pulse duration $\tilde{t}_0$ is the same as $\tilde{t}_0$ from the preceding chapters, as is $\tilde{r}$.

Three regions, each associated with one of three categories of scaling laws, are visible in this figure. The three regions in Figure 6.1, and their corresponding dominant scaling laws, are labeled in the following way: (A) $e^* \propto t_0$, (B) $e^* \propto t_0^{-1}$, and (C) $e^* \propto t_0^0$.

This alternative labeling convention is introduced because the applicability of each scaling law depends on position, the amount of damping, and the pulse duration. The "short pulse" and "long pulse" nomenclature of the previous chapter does not account for the position-dependence of scaling law applicability, since it is based on describing the pulse duration with respect to a single characteristic time that applies to the whole of the delicate object. This works well when there is only one degree of freedom, as in the spring-mass oscillator, but the infinite degrees of freedom of the cylindrical continuum problem each have their own characteristic time. Additionally, the framework of Kornhauser and Lawton assumes that the transition out of the short-pulse response is a transition into the long-pulse response. For smooth pulses, the B-type transition from A-type behavior to C-type behavior occurs over a wider range of pulse durations, and has its own scaling law. The critical durations that bound the A-type region and the C-type regions are t_A and t_C, respectively. They are non-dimensionlized in the same manner as other time-based quantities, using the time it takes a shear wave to propagate the distance R_i within the cylinder of interest. Using the "A, B, C" framework with two critical pulse durations, t_A and t_C, builds on the spring-mass oscillator framework while also accurately describing the range of responses seen in the more complicated visco-elastic cylinder model.

Table 6.1 lists different ways of expressing these scaling laws. The scaling expressions in the third column of the table correlate strain with kinematic quantities without involving the pulse duration directly. We note that although Table 6.1 expresses shear strain in terms of angular quantities, like $|\ddot{\theta}|_{max}$, converting between these and the circumferential kinematic quantities, like a_θ^{max}, is achieved by straightforward multiplication or division by the internal radius of the shell, R_i.

In Figure 6.1, the relationship $e^* \propto t_0$ is identified with the letter A, and applies to short pulses, with durations less than t_A. The critical duration t_A depends on the position r/R_i, and it will be discussed in subsection 6.2. The expression for the dependence of maximum strain on acceleration and pulse duration can be re-written as $\varepsilon_{r\theta}^{max} \propto |\dot{\theta}|_{max}$, since the

Table 6.1: Scaling law labels and alternative expressions.

Label	e^* scaling with t_0^x	$\varepsilon_{r\theta}^{max}$ scaling with angular kinematic quantities
A	$e^* \propto t_0^1$	$\varepsilon_{r\theta}^{max} \propto \lvert\dot{\theta}\rvert_{max}$
B	$e^* \propto t_0^{-1}$	$\varepsilon_{r\theta}^{max} \propto \lvert\frac{\partial \ddot{\theta}}{\partial t}\rvert_{max}$
C	$e^* \propto t_0^0$	$\varepsilon_{r\theta}^{max} \propto \lvert\ddot{\theta}\rvert^{max}$

maximum angular speed, $|\dot{\theta}|_{max}$, is proportional to the product of the maximum angular acceleration and the pulse duration. The A-type behavior is analogous to the short-duration response limit in [23].

For intermediate-duration pulses with the sine pulse shape, the relationship $e^* \propto t_0^{-1}$ may appear. Recalling Chapter III, this type of dependence of strain on acceleration magnitude and pulse duration suggests that the magnitude of the maximum strain is proportional to the maximum of the first time derivative of angular acceleration. This type of scaling is associated with a transition from the A-type scaling to the C-type scaling, and does not evolve in all circumstances. The conditions where the B-type transition occurs, and the ones where it does not, are discussed in section 6.1.1.

For pulses with durations longer than the critical pulse duration, t_C, the normalized strain approaches $e^* \propto t_0^0$, alternatively written as $\varepsilon_{r\theta}^{max} \propto |\ddot{\theta}|_{max}$. This type of relationship is identified with the letter C, and corresponds to the long-pulse response in [23]. In this circumstance, the ratio of strain to maximum acceleration magnitude stays roughly the same for pulses of different durations. Depending on the material properties, however, the behavior of pulses longer than t_C may depart from the expected $e^* \propto t_0^0$ relationship if the relaxation time of the medium is of the same order as the pulse duration.

6.1.1 The existence of B-type response to angular acceleration depends on pulse shape

In the previous section, three types of strain-angular acceleration scaling laws were identified for the sinusoidal pulse. However, not all of these responses occur for all cylin-

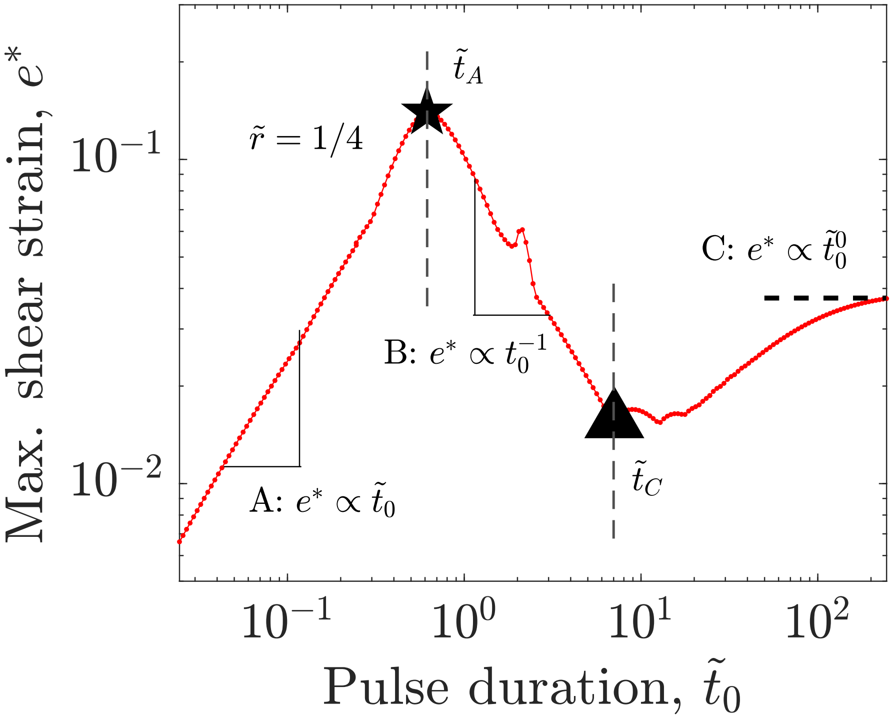

Figure 6.1: Dimensionless maximum shear strain, e^*, is plotted with respect to the dimensionless duration of the angular acceleration pulse that caused it. The maximum shear strain, $\varepsilon_{r\theta}^{max}$, at the position $\tilde{r} = 1/4$ can be made dimensionless with the maximum of the magnitude of the angular acceleration pulse, and the properties of the cylinder, G_u, ρ, and R_i. This dimensionless maximum shear strain, e^*, is a function of pulse duration, t_0, which can also be rendered dimensionless with the same properties of the cylinder that are used to non-dimensionalize the maximum shear strain. The dimensionless pulse duration is $\tilde{t}_0 = t_0\sqrt{G_u/\rho}/R_i$. Three kinematic scaling law relationships that relate the maximum shear strain and the dimensionless pulse duration are visible. These scaling laws are listed in Table 6.1, and described briefly there. The other parameters that describe this cylinder are $G_r/G_u = 0.2$, $\tau_R = 0.1$ s, $R_i = 0.1$ m, $\rho = 1000$ kg/m^3, and $G_u = 6$ kPa.

der materials and pulse shapes. For example, the bipolar rectangular pulse exhibits only the A-type $\varepsilon_{r\theta}^{max} \propto |\ddot{\theta}|_{max} t_0$ and C-type $\varepsilon_{r\theta}^{max} \propto |\ddot{\theta}|_{max}$ responses. Figure 6.2 depicts the scaling laws with respect to angular velocity for four types of pulses: sine, half-sine, bipolar rectangular, and single rectangular. The exact time-dependence of these pulses can be found in Figure 4.2. The pulses with sharp increases in acceleration (the bipolar rectangular pulse and single rectangular pulse) transition directly from the short-pulse response (A) to the long pulse response (C). In contrast, the pulses with smoother acceleration profiles (sine pulse and half-sine pulse) have the intermediate response, (B), where $\varepsilon_{r\theta}^{max} \propto |\dot{\theta}|_{max} t_0^{-2}$. There is also an important difference in the magnitude of the maximum strain between the smooth acceleration pulses and those with sharp changes. The sharply-changing acceleration pulses give rise to much higher values of maximum strain within the C region. In the C region, the maximum shear strain does not follow the $\varepsilon_{r\theta} \propto r^2$ spatial scaling that the smoother pulses have. As discussed in Section 5.3, the sharp acceleration rise is associated with both a transient wave and a quasi-static or steady state strain field. The magnitude of the transient part is larger than the steady state part, so that part dominates the maximum strain for the bipolar rectangular pulse and the single rectangular pulse in the (C) $\varepsilon_{r\theta}^{max} \propto |\ddot{\theta}|_{max}$ regime.

The absence or presence of the B-type transition also depends on relaxation time of the cylinder medium. However, the effect of the magnitude of the relaxation time is difficult to separate from the effect that increased or decreased dissipation has, since dissipation level depends on the relaxation time. In Figures 6.2a and 6.2b, the $r/R_i = 1/4$ curves for the smaller relaxation time $\tilde{\tau}_R = 0.245$ have no B-type transition, and segue directly from A-type $\varepsilon_{r\theta}^{max} \propto |\dot{\theta}|_{max}$ to C-type $\varepsilon_{r\theta}^{max} \propto |\ddot{\theta}|_{max}$, even though the pulses are smooth, and the shear strain approaches the steady-state limit. Further into the interior of the cylinder, at $r/R_i = 1/16$, however, there is a B-type transition, initiating at a smaller $\tilde{t}_A$ value, around 0.13, and ending at a larger $\tilde{t}_C$ value, around 1.3, than for $r/R_i = 1/4$, where $\tilde{t}_A = \tilde{t}_C$, around 0.6. It is possible that the disappearance of the B-type transition for the $r/R_i = 1/4$

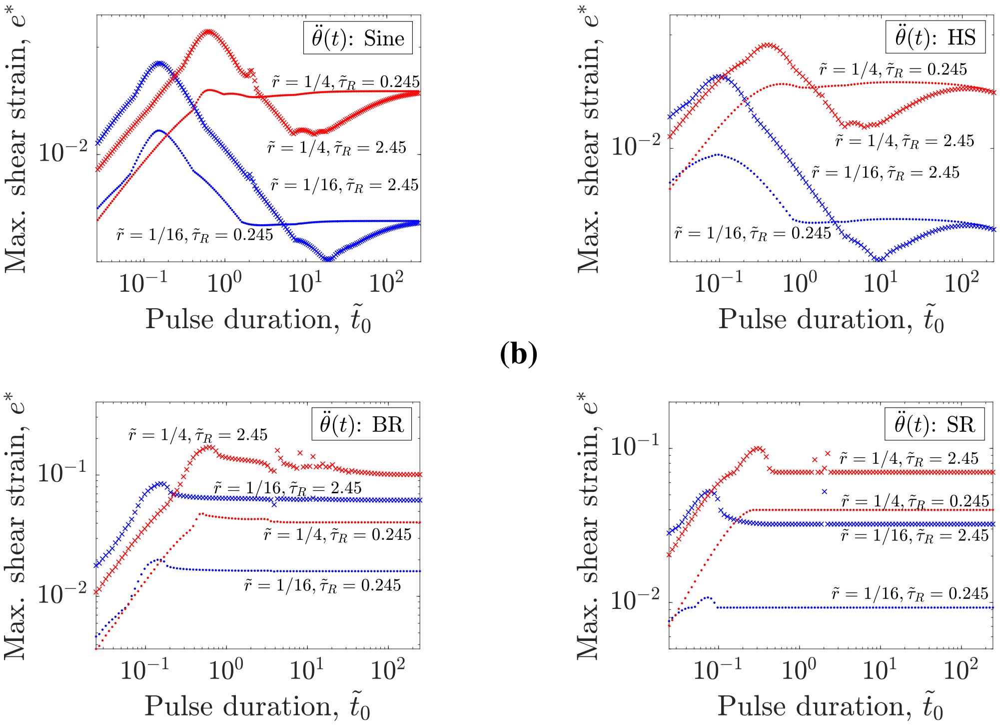

(a) **(b)**

(c) **(d)**

Figure 6.2: A dimensionless maximum strain, e^*, at two positions, $\tilde{r} = 1/4$ and $\tilde{r} = 1/16$, as a function of dimensionless pulse duration, $\tilde{t}_0$ for four types of pulses, Sine, HS, BR, SR. (a) and (b) are associated with smooth pulses, and they have a B-type transition region where the dimensionless maximum shear strain, e^*, is proportional to the maximum magntiude of the time-derivative of angular acceleration, $|\frac{\partial \ddot{\theta}}{\partial t}|_{max}$. However, for (c) and (d), which are associated with sharp angular acceleration increases, the dimensionless maximum shear strain remains at approximately the same levels as at t_A, as $\tilde{t}_0$ increases.

curves in Figures 6.2a and 6.2b is due to the shorter relaxation time causing the material to respond with more compliance. In that case, the response to a pulse with an intermediate duration is already closer to the response for a much longer pulse, because the glass transition behavior occurs over the same range of pulse durations as the transition from the wave-dominated response (A) to the steady-state-dominated (C) response. For example, for a pulse with a dimensionless duration $\tilde{t}_0 > 0.6$, and a cylinder with a dimensionless relaxation time $\tilde{\tau}_R = 0.245$, there is time for creep and stress relaxation to occur before the pulse is complete.

6.1.2 Onset of C-type behavior, at t_C, depends on pulse shape and damping within the cylinder.

The critical pulse duration, t_C, is the minimum duration for $\varepsilon_{r\theta}^{max}/|\ddot{\theta}|_{max} \propto t_0^0$ behavior. t_C strongly depends on whether there is a B-type transition. Since the existence of the B-type transition is dependent on dissipation and pulse shape, t_C depends on those properties, too. Referring back to Figure 6.2, it can be seen that smooth acceleration pulses have $\tilde{t}_C$ at a lower value than sharply increasing acceleration pulses of the same duration. The shorter $\tilde{t}_C$ for the sharply increasing pulse is due to the lack of B-type behavior for these acceleration pulses. The absence of B-type behavior, for sharply increasing pulses, is caused by the relatively high amplitude of the transient wave generated by this type of loading, as discussed in Section 5.3 and Subsection 6.1.1.

6.1.3 Scaling laws in the (A) region

In general, if $\tilde{t}_0 < \tilde{t}_A(r)$, then $\varepsilon_{r\theta}^{max}(r) \propto |\dot{\theta}|_{max}$, regardless of pulse duration. This proportionality and the discussion of the initial magnitude of the strain pulse in Section 5.4.2 motivates defining the dimensionless maximum shear strain as

$$\tilde{\varepsilon}_{r\theta} = \varepsilon_{r\theta} \frac{\sqrt{G_u/\rho}}{|\dot{\theta}|_{max} R_i}. \tag{6.2}$$

Figure 6.3 and Figure 6.4 are plots of the dimensionless maximum shear strain, $\tilde{\varepsilon}_{r\theta}^{max}$, obtained at three points with the cylinder, as a function of dimensionless pulse duration. In all parts of Figure 6.3, which are derived from the sine pulse and the bipolar rectangular pulse, which both leave the angular speed of the shell at rest at the end of the angular acceleration pulse ($|\dot{\theta}_f| = 0$), there is very little departure from the common $\varepsilon \propto |\dot{\theta}|_{max}$ scaling, for the shortest pulses, $\tilde{t}_0 < \tilde{t}_A$. The dependence of maximum shear strain on the maximum angular velocity of the shell, $|\dot{\theta}|_{max}$, is similarly simple in Figures 6.4b and 6.4d. Figures 6.4b and 6.4d are associated with the half sine pulse (b) and single rectangular pulse (d). They are also derived from the loading of a relatively highly-damping cylinder, with the dimensionless relaxation time $\tilde{\tau}_R = 0.245$.

The notable exception to $\varepsilon_{r\theta}(r) \propto |\dot{\theta}|_{max}$, in the A-region, is when the pulse has a net change in angular velocity, and the material has low damping. In that instance, the strain-duration curves in the A-region depart slightly from the $\varepsilon_{r\theta}^{max} \propto |\dot{\theta}|_{max}$ scaling that applies in other circumstances. In Figures 6.4a and 6.4b, where the half sine pulse and single rectangular pulse are considered, and the cylinders have relatively low damping, the dimensionless strain- pulse duration curves have a negative slope. The qualitative consequence of this slight negative slope is that the maximum strain is not strictly proportional with maximum angular velocity magnitude and, instead, is reduced when the maximum angular velocity magnitude is held constant and the pulse duration is extended. Nonetheless, the slope is not so steep that the $\varepsilon_{r\theta}^{max} \propto |\ddot{\theta}|^{max}$ relation would apply, either. A fractional power of duration and either $|\ddot{\theta}|^{max}$ or $|\dot{\theta}|_{max}$ might be a better description of this scaling, and warrants further study.

6.2 Critical duration t_A

The critical duration, t_A, is the maximum pulse duration for which the short-pulse scaling laws $\varepsilon_{r\theta}^{max} \propto |\dot{\theta}|_{max}$ and $\varepsilon_{r\theta}^{max} \propto |\dot{\theta}|_{max} t_0^{-1/2}$ apply. The critical duration, t_A, depends on position, r, and the infinite frequency shear wave speed, $v_u = \sqrt{G_u/\rho}$, but generally

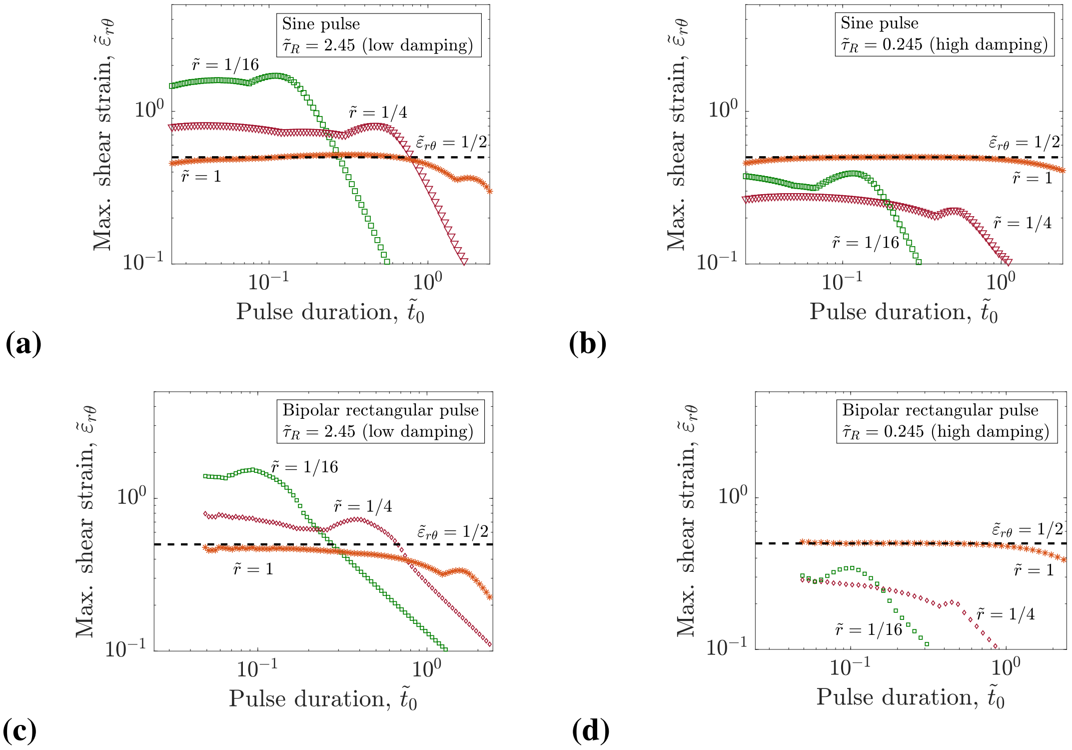

Figure 6.3: Maximum shear strain as a function of pulse duration for the sine pulse and the bipolar rectangular pulse. Two different relaxation times that lead to different amounts of damping are also considered. (a) and (b) are associated with the sine pulse, and (c) and (d) are for a bipolar rectangular pulse. In all four, there is a well-defined horizontal region of each curve, for $\tilde{t}_0 < \tilde{t}_A$, where strain stays within a range of approximately a factor of 2. That is, in these situations, the strain can be said to closely follow the scaling expression $\varepsilon_{r\theta} \propto |\dot{\theta}|_{max}$.

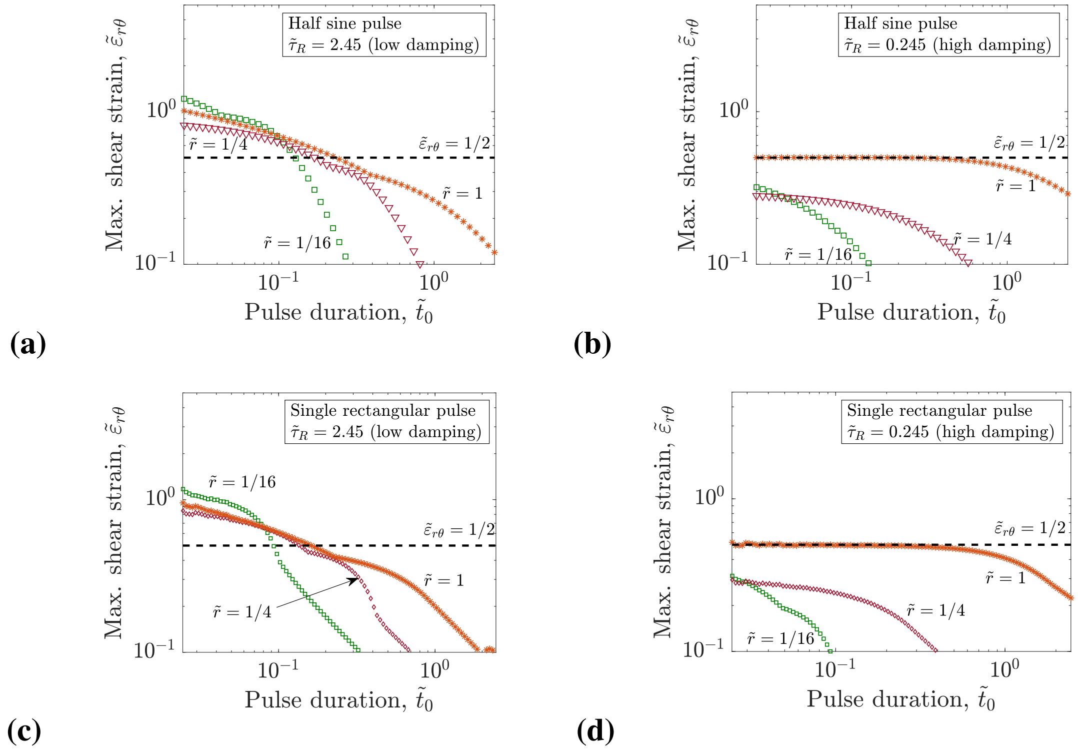

Figure 6.4: Maximum shear strain as a function of pulse duration for the sine pulse and the bipolar rectangular pulse. Two different relaxation times that lead to different amounts of damping are also considered. (a) and (b) are associated with the half sine pulse, and (c) and (d) are for a single rectangular pulse. The pulses applied to cylinders with high damping, (b) and (d), produce shear strain which satisfies the expression $\varepsilon_{r\theta} \propto |\dot{\theta}|_{max}$. This is indicated by the constant values for $\tilde{\varepsilon}_{r\theta}$. When there is low damping, in (a) and (c), the strain that is produced approximately follows the relation $\varepsilon_{r\theta} \propto |\dot{\theta}|_{max} t_0^{-1/2}$.

does not depend on how much of the initial strain pulse is dissipated, or the pulse shape.

The critical pulse duration t_A can be non-dimensionalized in the same way as the pulse duration, t_0, relaxation time, τ_R, are non-dimensionalized:

$$\tilde{t}_A = t_A \sqrt{G_u/\rho}/R_i \tag{6.3}$$

$t_A(\tilde{r})$ is a function of dimensionless position, $\tilde{r} = r/R_i$, but is independent of pulse magnitude, $|\ddot{\theta}|_{max}$ or $|\dot{\theta}|_{max}$. Whether the acceleration increases sharply or smoothly does not affect t_A. However, the critical duration for the sine pulse and the bipolar rectangular pulse is twice the critical duration for the half-sine pulse and the single rectangular pulse. Therefore, it appears that it is the duration of the positive region of the pulse, t_p, that governs the switch from $\varepsilon_{r\theta}^{max} \propto |\dot{\theta}|_{max} R_i$ to other scaling laws, rather than the whole pulse duration t_0. t_{pA} and its dimensionless quantity $\tilde{t}_{pA}$ refer to the critical t_p that designates the end of the $\varepsilon_{r\theta}^{max} \propto |\dot{\theta}|_{max} R_i$ regime. In this analysis which compares only four pulse shapes, t_{pA} appears to be mostly independent of pulse shape. Although t_{pA} depends on the stiffness and density of the material, the dimensionless critical pulse duration, $\tilde{t}_{pA}(\tilde{r})$, is the same for most cylinders, including those with different relaxation times, τ_R, and shear moduli, G_u and G_r.

The dimensionless maximum shear strain results for $\tilde{r} = 1/4$ and $\tilde{r} = 1$ from Figures 6.3 and 6.4 can be regrouped and re-plotted, with pulse duration parameterized with $\tilde{t}_p$, rather than $\tilde{t}_0$. Figure 6.5 contains these plots. It can be seen that, for a given position and dimensionless relaxation time, $\tilde{t}_{pA}$ has approximately the same value, regardless of pulse shape. The similarity of the responses to pulses of different shapes is especially strong for the cylinders with high damping, *e.g.* when $\tilde{\tau}_R = 0.245$, as depicted in Figures 6.5c and 6.5 d.

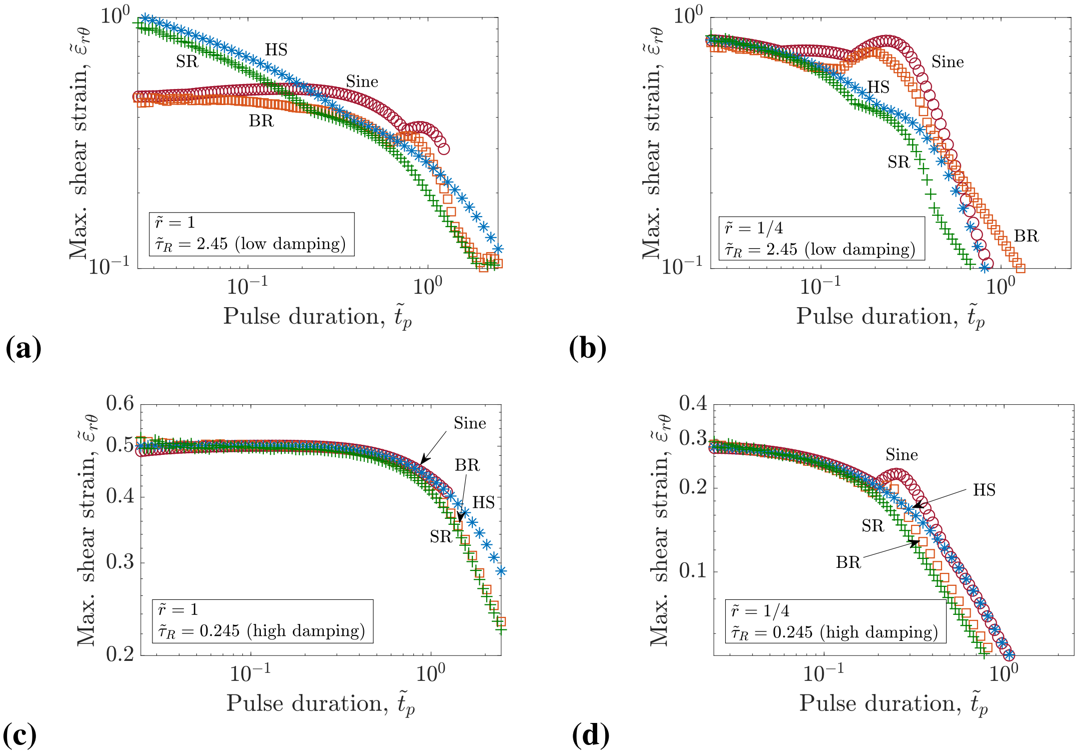

Figure 6.5: Dimensionless maximum shear strain, $\tilde{\varepsilon}_{r\theta}$ as a function of the dimensionless duration of the positive section of the acceleration pulse, $\tilde{t}_p$, at two different positions within the cylinder, $\tilde{r} = 1$ and $\tilde{r} = 1/4$, and two different dimensionless relaxation times, $\tilde{\tau}_R = 2.45$ and $\tilde{\tau}_R = 0.245$. The A-type $\varepsilon_{r\theta}^{max} \propto |\dot{\theta}|_{max}$ regions end at roughly the same positions for all pulse types, especially when there is high damping ($\tilde{\tau}_R = 0.245$). Sine: sine pulse, HS: half sine pulse, BR: bipolar rectangular pulse, SR: single rectangular pulse. (a) and (c) are associated for $\tilde{r} = 1$ and (b) and (d) are for $\tilde{r} = 1/4$.

6.2.1 $\tilde{t}_A$ dependence on $\tilde{r}$

Figure 6.6 shows the normalized maximum shear strain, $\varepsilon_{r\theta}^{max}/(R_i|\ddot{\theta}|_{max})$ at four different locations, $\tilde{r}$, as a function of pulse duration, t_0, for two cylinders with different relaxation times, τ_R. The two cylinders under consideration here have the same radius $R_i = 0.1$ m, unrelaxed shear modulus $G_u = 6$ kPa, modulus ratio $G_r/G_u = 0.2$, and density $\rho = 1000$ kg/m^3. The results in Figure 6.6a are for a cylinder with $\tau_R = 0.1$ s and those in Figure 6.6b are for $\tau_R = 0.01$ s. Carrying out the relevant arithmetic gives the result that the cylinder with $\tau_R = 0.1$ s has dimensionless relaxation time, $\tilde{\tau}_R = 2.45$ and the cylinder with $\tau_R = 0.01$ s has the dimensionless relaxation time $\tilde{\tau}_R = 0.245$. These correspond to relatively low damping and relatively high damping respectively.

Black stars and dashed grey lines indicate where the $\varepsilon_{r\theta}^{max}/|\ddot{\theta}|_{max} \propto t_0$ region ends for each of the different radial positions, $\tilde{r} = 1, 1/4, 1/16,$ and $1/64$. When the damping low, as is the case for the cylinder with $\tau_R = 0.1$ s, then $t_A(\tilde{r}^*$ is also the pulse duration for which the whole-cylinder maximum strain is attained at the radial position $\tilde{r}^*$. For example, letting $\tilde{r}^* = 1/4$, we can see that the pulse duration $t_0 = t_A(1/4)$ the pulse duration for which the spatial maximum of $\varepsilon r\theta^{max}$ is at $\tilde{r} = 1/4$. However, as Figure 6.6b shows, this is not the case for some cylinder media. In Figure 6.6b, which is for a cylinder with $\tau_R = 0.01$ s, the t_A values are the same as in Figure 6.6a, even though the magnitude of the strain is different and the spatial distribution of strain is different, too. If $t_0 = t_A(1/4) = 0.022$ s in this situation, the highest normalized strain throughout the cylinder is around 0.0015, and occurs at the radial position $\tilde{r} = 1$, not $\tilde{r} = 1/4$. The maximum strain for $\tilde{r} = 1/4$ is lower than that, with a value of 0.0007.

6.3 Whole-cylinder strain scaling laws for short pulses

In the previous section, each position within the cylinder was considered separately, and scaling laws for the maximum shear strain experienced by the material at a few different

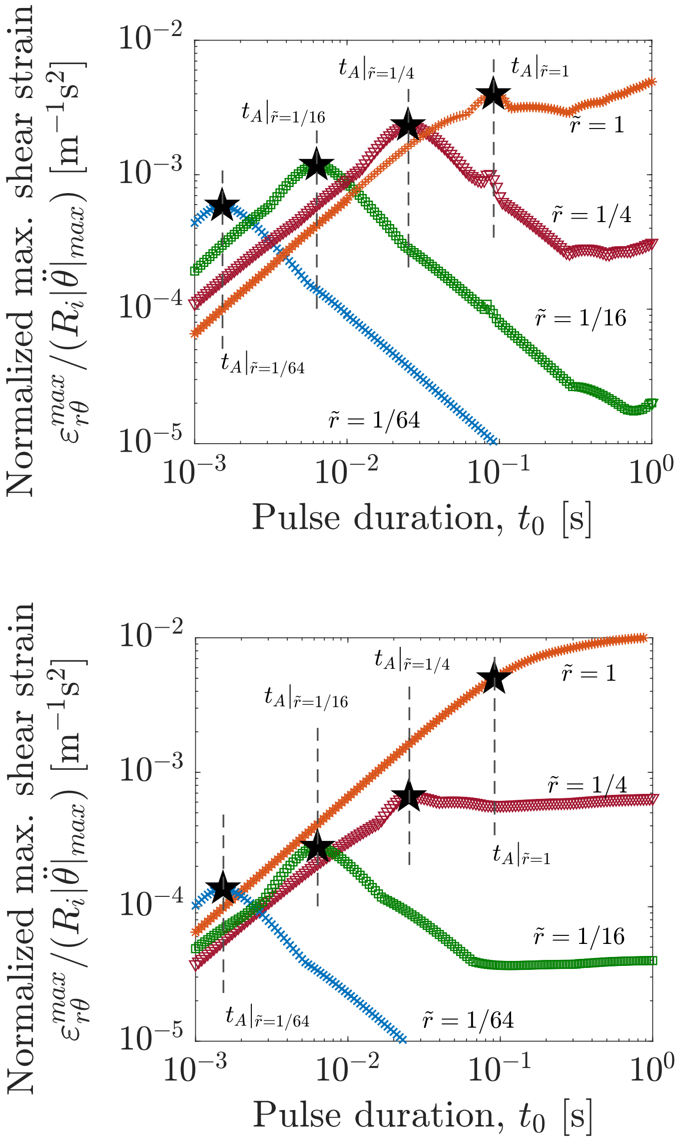

(a)

(b)

Figure 6.6: Maximum strain, normalized by maximum tangential acceleration, at four positions, as a function of pulse duration for a single-period sinusoidal acceleration pulse. The critical durations t_A for the end of the $\varepsilon_{r\theta}^{max}/|\ddot{\theta}|_{max} \propto t_0$ region are indicated with black stars. (a) $\tau_R = 0.1$ s. (b) $\tau_R = 0.01$ s. For all four positions, the t_A values are not affected by the relaxation time. $G_u = 6$ kPa, $\rho = 1000$ kg/m^{-3}, $R_i = 0.1$ m.

points with the cylinder were identified. Then, those results were used to draw conclusions about the response at other points within the cylinder. However, there is interest in identifying the scaling laws for the highest strain attained throughout the cylinder. This spatial maximum of temporal maxima is referred to as the whole-cylinder maximum shear strain, $\varepsilon_{r\theta}^{wcm}$, in this work. The dimensionless form for this quantity is

$$\tilde{\varepsilon}_{r\theta}^{wcm} = \varepsilon_{r\theta}^{wcm} \frac{\sqrt{G_u/\rho}}{|\dot{\theta}|_{max} R_i} \tag{6.4}$$

For long-duration pulses (region C), the whole-cylinder maximum shear strain is the same as the maximum shear strain at the outer radius of the cylinder, $\tilde{r} = 1$. For short pulses, however, the location of the whole-cylinder maximum shear strain varies with the pulse duration and the dimensionless relaxation time of the cylinder. Figures 6.7 and 6.8 depict the relationship between the dimensionless whole-cylinder maximum strain, $\tilde{\varepsilon}_{r\theta}^{wcm}$, and the dimensionless pulse duration, $\tilde{t}_0$, for different pulse shapes and relaxation times. Figure 6.7 gives the scaling for a cylinder with low damping, from having the dimensionless relaxation time $\tilde{\tau}_R = 2.45$. Figure 6.8 is associated with the higher dissipation dimensionless relaxation time, $\tilde{\tau}_R = 0.245$. For the low damping relaxation time, $\tilde{\tau}_R = 2.45$, the dimensionless whole-cylinder maximum shear strain (grey circles) approximately follows the expression

$$\tilde{\varepsilon}_{r\theta}^{wcm} \propto \tilde{t}_0^{-1/2} \tag{6.5}$$

for $\tilde{t}_p < 1$. This type of scaling is indicated with a dashed black line overlaying the data.

In Figures 6.7a and 6.7c, the $\tilde{\varepsilon}_{r\theta}^{wcm} \propto \tilde{t}_0^{-1/2}$ scaling is associated with the migration of the radial position where the whole cylinder maximum shear strain occurs, as the pulses become shorter. For example, the maximum shear strain curves for $\tilde{r} = 1/64$ (blue 'x's), $\tilde{r} = 1/16$ (green squares), and $\tilde{r} = 1/4$ (burgundy triangles) are tangent to the $\tilde{\varepsilon}_{r\theta}^{wcm}$-curve at various dimensionless durations. This means that for the duration where the $\tilde{\varepsilon}_{r\theta}(\tilde{r}^*)$ curve overlaps the $\tilde{\varepsilon}_{r\theta}^{wcm}$ curve, $\tilde{\varepsilon}_{r\theta}(\tilde{r}^*, \tilde{t}_0) = \tilde{\varepsilon}_{r\theta}^{wcm}(\tilde{t}_0)$. The $\tilde{\varepsilon}_{r\theta}^{wcm}$-values between these intersections are associated with $\tilde{\varepsilon}_{r\theta}^{wcm}$ occurring at intervening positions, even though not every $\tilde{\varepsilon}_{r\theta}(\tilde{r}^*)$ curve is plotted.

In Figures 6.7b and 6.7d, as was noted in Section 6.1.3, the short-pulse response to both pulse shapes that have $|\dot{\theta}_f| \neq 0$ (half sine and single rectangular pulses), for cylinders with low damping, does not follow the $\varepsilon \propto |\dot{\theta}|_{max}$ scaling common to other scenarios. This phenomena makes it more difficult to interpret the $\tilde{\varepsilon}_{r\theta}^{wcm}$ curve, especially as it relates to the strain at $\tilde{r} = 1$, which governs $\tilde{\varepsilon}_{r\theta}^{wcm}$ starting at $\tilde{t}_0$ values between 0.1 and 0.2 for both pulse shapes. Although the source of this type of proportionality has not yet been identified here, the same approximate scaling law that applies to the other two pulse shapes, $\tilde{\varepsilon}_{r\theta}^{wcm} \propto \tilde{t}_0^{-1/2}$ seems adequate for these pulses, too.

In Figure 6.8, $\tilde{\varepsilon}_{r\theta}^{wcm} \propto \tilde{t}_0^{-1/2}$ is not sufficient to describe the scaling between $\tilde{\varepsilon}_{r\theta}^{wcm}$ and the pulse duration. For the range of pulse durations considered, the highly damping cylinder properties lead to the $\tilde{\varepsilon}_{r\theta}^{wcm}$ being entirely governed by $\tilde{\varepsilon}_{r\theta}$ at $\tilde{r} = 1$ for the pulses with $|\dot{\theta}_f| \neq 0$. For the sine pulse, the shortest pulse durations have the $\tilde{\varepsilon}_{r\theta}^{wcm} \propto \tilde{t}_0^{-1/2}$ scaling that the less dissipative cylinder from Figure 6.7 has. Future work should consider even shorter pulses, to see if the $\tilde{\varepsilon}_{r\theta}^{wcm} \propto \tilde{t}_0^{-1/2}$ scaling emerges for the other pulse shapes for very small pulse durations, or if the dissipation is sufficient to eliminate it. Recalling Section 5.5.2, the attenuation of the strain pulse as it propagates across the cylinder reduces the maximum shear strain seen at points closer to the center of the cylinder. In a highly damped cylinder, the whole-cylinder maximum shear strain is obtained at the outer radius of the cylinder, $\tilde{r} = 1$, where the shear strain pulse is initiated.

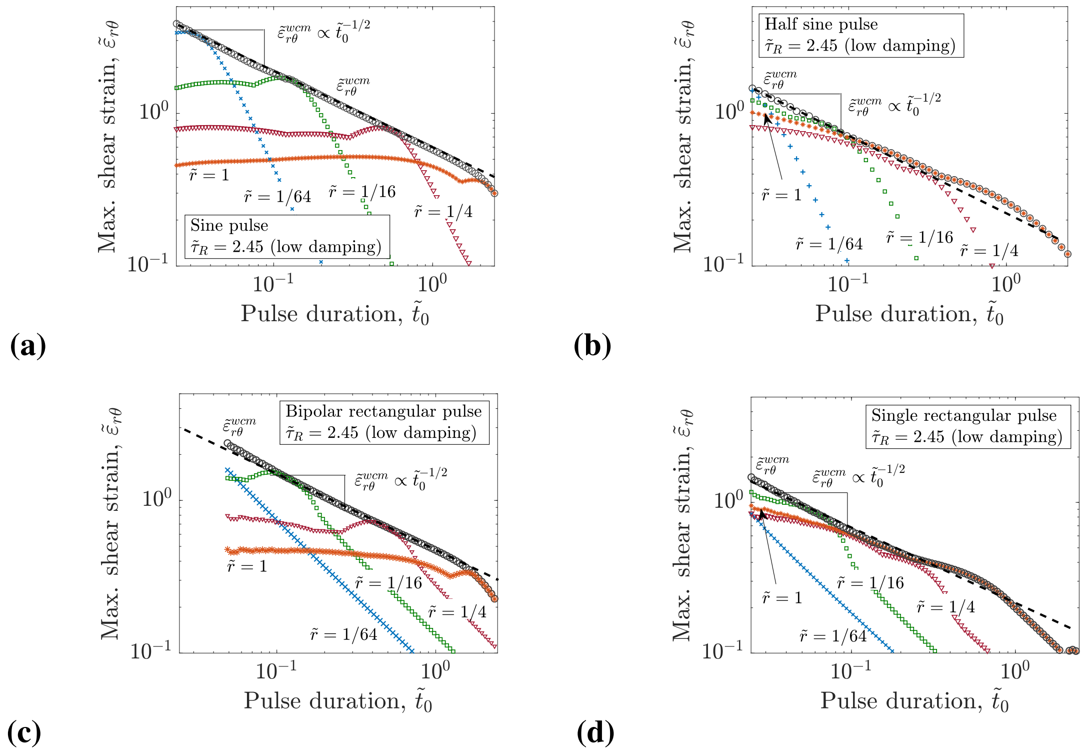

Figure 6.7: Whole-cylinder maximum shear strain as a function of the duration of the duration of the acceleration pulse, $\tilde{t}_0$. The maximum shear strains at four points within the cylinder are also indicated. The dimensionless relaxation time is $\tilde{\tau}_R = 2.45$, which results in relatively low damping. (a) Sine pulse. (b) Half sine pulse. (c) Bipolar rectangular pulse. (d) Single rectangular pulse.

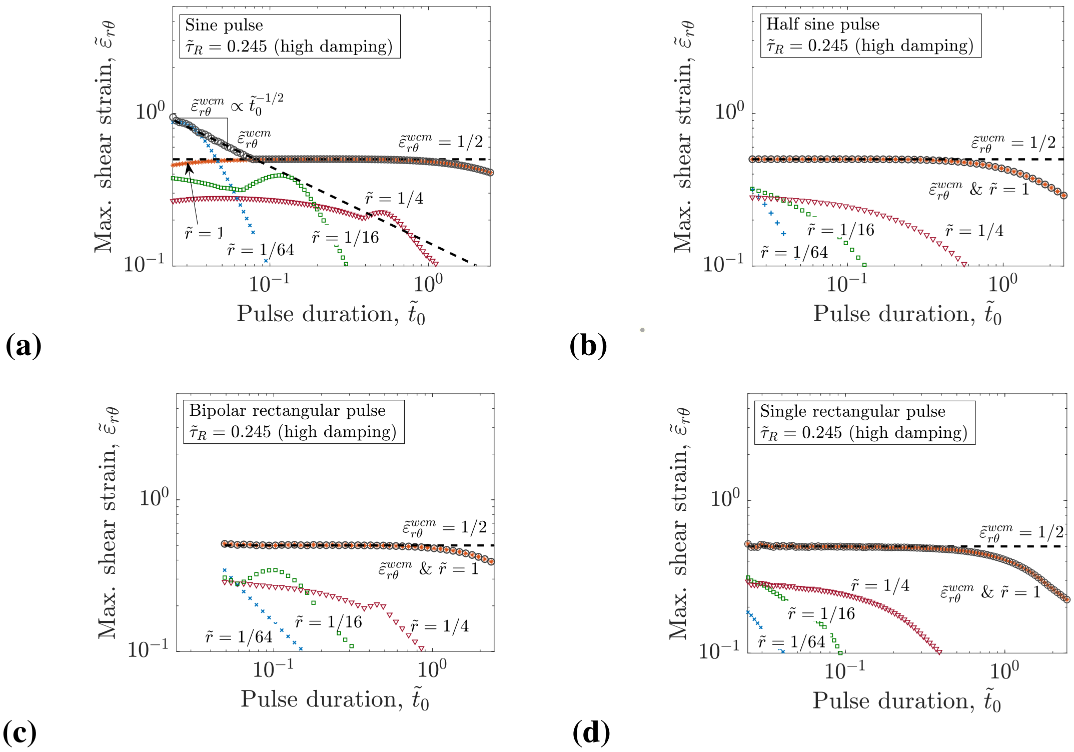

Figure 6.8: Whole-cylinder maximum shear strain as a function of the duration of the angular acceleration pulse, $\tilde{t}_0$. The maximum shear strains at four points within the cylinder are also indicated. The dimensionless relaxation time is $\tilde{\tau}_R = 0.245$, which results in relatively high damping. (a) Sine pulse. (b) Half sine pulse. (c) Bipolar rectangular pulse. (d) Single rectangular pulse.

6.4 Conclusions

6.4.1 Scaling laws relating strain to kinematic variables for cylindrical delicate objects enclosed in rotating shells

For a delicate object with the cylindrical geometry studied in this chapter, the response to angular acceleration pulses of different durations can be categorized into one of three types. There are sub-categories of these three primary response types that emerge when the damping capability of the cylinder medium and the pulse shape are varied, too.

Short pulses give rise to the (A)-type response, which can be described by the scaling law $\varepsilon \propto |\dot{\theta}|_{max}$ or $\varepsilon \propto |\dot{\theta}|_{max} t_0^{-1/2}$, depending on the shape of the angular acceleration pulse and whether the cylinder medium is very dissipative. The $\varepsilon \propto |\dot{\theta}|_{max} t_0^{-1/2}$ scaling law operates only when the angular acceleration pulse causes nonzero final angular speed, $|\dot{\theta}_f| \neq 0$, and the cylinder has relatively low damping. If the pulse does not drive a permanent change in the angular speed, $|\dot{\theta}_f| = 0$, or the cylinder is highly damping, then the $\varepsilon \propto |\dot{\theta}|_{max}$ scaling applies.

Considering only pulses with the same shape, the longest pulse duration for which either the $\varepsilon \propto |\dot{\theta}|_{max}$ or $\varepsilon \propto |\dot{\theta}|_{max} t_0^{-1/2}$ scaling applies is denoted with the symbol t_A. t_A depends on pulse shape, but t_{pA}, which is a similar quantity, and is defined as the critical duration associated only with the positive region of the angular acceleration pulse, is roughly the for all pulse types. t_{pA} also depends on the position, and decreases with the radial coordinate, r. Therefore, the region of the cylinder farthest from the center can respond to an angular acceleration pulse with the A-type response, while the interior region of the cylinder responds to the same pulse with either the B-type response or the C-type response.

The critical duration $t_{pA}(r)$ is important because it delineates the pulse durations which generate the (A)-type response at a point in the cylinder from pulse durations which lead to other behaviors. If the positive region of the angular acceleration pulse due to an impact is longer than the critical duration t_{pA}, then either the angular acceleration, or its time-derivative, is the kinematic quantity which best predicts the extent of deformation with the cylinder at a particular position. In this scenario, additional analysis of the angular acceleration pulse shape and the extent of damping must be considered to distinguish whether the impact is in the B-type region or the C-type region. If the impact has $t_p < t_{pA}$, then the kinematic quantity most likely to predict deformation is the maximum magnitude of the angular velocity, possibly with some additional influence of pulse duration, depending on the pulse shape and amount of damping, as explained previously.

Based on the consistency in the value of $\tilde{t}_{pA}(r)$ across pulse types, it can be concluded that the critical duration at the outer radius of the cylinder, $t_{pA}(\tilde{r} = 1)$, for a given cylinder, is a property of the cylinder alone; it depends only on G_u, ρ, and R_i. Specifically, this dimensionless critical duration $\tilde{t}_{pA}(1)$, is the ratio of the positive region of the pulse, t_0, to the time it would take a shear wave to propagate to the center of the cylinder $R_i/\sqrt{G_u/\rho}$. Therefore, cylinders with larger radii, higher densities, and lower shear moduli will have larger values of $t_{pA}(r = R_i)$ than cylinders with smaller outer radii, lower densities, and higher shear moduli.

The other limit for the response of a rotating cylinder is the long-pulse response, which is labeled with the letter "C". All the combinations of cylinder properties and pulse types considered in this study eventually exhibit $\varepsilon_{r\theta} \propto |\ddot{\theta}|_{max}$ for sufficiently long angular acceleration pulses. However, the spatial distribution of strain in this limit differs between pulses which have a sharp increase in angular acceleration, and those which have a smoothly-varying shape. The smooth pulses result in $\varepsilon_{r\theta} \propto r^2$ scaling in the long-duration limit, whereas those with sharp increases do not.

If the pulse is smooth, there may be an extended transition (B) between the short-pulse response (A) and the long-pulse response (C). In this transition, $\varepsilon_{r\theta} \propto |\ddot{\theta}|_{max}/t_0$, and this region lasts from t_A to t_C. The conditions under which the B-type transition exists are not fully characterized here, but preliminary observations suggest that damping can suppress the existence of the extended transition, and that it generally appears for smooth pulses but does not appear for sharply-increasing ones. When the extended transition does not appear, t_A is necessarily the same as t_C, because the end of the A-type region is the begineeing of the C-type region.

The maximum shear strain attained across the whole cylinder depends on the position-specific maximum shear strains. There are also multiple scaling laws that describe this quantity, and their applicability also depends on the duration of the pulse. The other governing factor is the amount of dissipation and attenuation that shear waves experience within the given cylinder.

For short pulses, if the cylinder is highly dissipating, the maximum shear strain over the whole cylinder occurs at the outer radius of the cylinder, so the trends in the response of the strain at that location are the same as the trends for the whole cylinder maximum shear strain, overall. However, if the cylinder is not very dissipative, then the circular geometry focuses the shear wave, with the strain increasing with decreasing radial coordinate values, until it reaches a critical radius, where the peak in strain occurs. There can be no strain at the exact center of the cylinder, so the peak strain is attained at a small distance from the center, which depends on the spatial width of the pulse. This distance is a result of the pulse duration and the speed with which the shear wave propagates. This produces the scaling law $\varepsilon^{wcm} \propto |\dot{\theta}|_{max} t_0^{-1/2}$. Further analysis of this focusing and amplification of strain at the very middle of the cylinder is likely not relevant to the study of the human head, however, as the human head is not perfectly symmetrical, and this phenomenon is predicated on the radial symmetry of the simplified, cylindrical, geometry considered in this chapter. The $\varepsilon^{wcm} \propto |\dot{\theta}|_{max} t_0^{-1/2}$ scaling that occurs in low damping cylinders, when subjected to pulses with $|\dot{\theta}_f| \neq 0$, is also due to the response of the material at the outer radius of the cylinder, which has this form for the position-dependent maximum strain scaling law, too. More study of the origins of this position-dependent scaling law are warranted, as rotational impacts frequently lead to pulses with $|\dot{\theta}_f| \neq 0$, and the human brain may be under-damped.

The essential components of the observations described above are cataloged in Table 6.2 and Table 6.3.

	$\lvert\dot{\theta}_f\rvert = 0$	$\lvert\dot{\theta}_f\rvert \neq 0$
Smooth	Sine pulse a.) $\tilde{\varepsilon}_{r\theta}^{wcm} \propto \lvert\dot{\theta}\rvert_{max} t_0^{-1/2}$ in (A) b.) $\varepsilon_{r\theta} \propto \lvert\dot{\theta}\rvert_{max}$ in (A) c.) $\varepsilon_{r\theta} \propto \lvert\ddot{\theta}\rvert_{max}/t_0$ in (B) d.) $\varepsilon_{r\theta} \propto r^2$ in (C)	Half sine pulse a.) $\tilde{\varepsilon}_{r\theta}^{wcm} \propto \lvert\dot{\theta}\rvert_{max} t_0^{-1/2}$ in (A) b.) $\varepsilon_{r\theta} \propto \lvert\dot{\theta}\rvert_{max} t_0^{-1/2}$ (approx.) in (A) c.) $\varepsilon_{r\theta} \propto \lvert\ddot{\theta}\rvert_{max}/t_0$ in (B) d.) $\varepsilon_{r\theta} \propto r^2$ in (C)
Sharp	Bipolar rectangular pulse a.) $\tilde{\varepsilon}_{r\theta}^{wcm} \propto \lvert\dot{\theta}\rvert_{max} t_0^{-1/2}$ in (A) b.) $\varepsilon_{r\theta} \propto \lvert\dot{\theta}\rvert_{max}$ in A c.) No (B)-region; $t_A = t_C$ d.) Lacks $\varepsilon_{r\theta} \propto r^2$ scaling in (C)	Single rectangular pulse a.) $\tilde{\varepsilon}_{r\theta}^{wcm} \propto \lvert\dot{\theta}\rvert_{max} t_0^{-1/2}$ in (A) b.) $\varepsilon_{r\theta} \propto \lvert\dot{\theta}\rvert_{max} t_0^{-1/2}$ (approx.) in (A) c.) No (B)-region; $t_A = t_C$ d.) Lacks $\varepsilon_{r\theta} \propto r^2$ scaling in (C)

Table 6.2: Summary of scaling laws for low damping

	$\lvert\dot{\theta}_f\rvert = 0$	$\lvert\dot{\theta}_f\rvert \neq 0$
Smooth	Sine pulse a.) $\tilde{\varepsilon}_{r\theta}^{wcm} \propto \lvert\dot{\theta}\rvert_{max} t_0$ in (A) b.) $\varepsilon_{r\theta} \propto \lvert\dot{\theta}\rvert_{max}$ in (A) c.) $\varepsilon_{r\theta} \propto \lvert\ddot{\theta}\rvert_{max}/t_0$ for small radii, no (B)-region for large radii d.) $\varepsilon_{r\theta} \propto r^2$ in (C)	Half sine pulse a.) $\tilde{\varepsilon}_{r\theta}^{wcm} \propto \lvert\dot{\theta}\rvert_{max} t_0$ in (A) b.) $\varepsilon_{r\theta} \propto \lvert\dot{\theta}\rvert_{max}$ in (A) c.) $\varepsilon_{r\theta} \propto \lvert\ddot{\theta}\rvert_{max}/t_0$ for small radii, no (B)-region for large radii d.) $\varepsilon_{r\theta} \propto r^2$ in (C)
Sharp	Bipolar rectangular pulse a.) $\tilde{\varepsilon}_{r\theta}^{wcm} \propto \lvert\dot{\theta}\rvert_{max} t_0$ in (A) b.) $\varepsilon_{r\theta} \propto \lvert\dot{\theta}\rvert_{max}$ in (A) c.) No (B)-region; $t_A = t_C$ d.) Lacks $\varepsilon_{r\theta} \propto r^2$ scaling in (C)	Single rectangular pulse a.) $\tilde{\varepsilon}_{r\theta}^{wcm} \propto \lvert\dot{\theta}\rvert_{max} t_0$ in (A) b.)$\varepsilon_{r\theta} \propto \lvert\dot{\theta}\rvert_{max}$ in (A) c.) No (B)-region; $t_A = t_C$ d.) Lacks $\varepsilon_{r\theta} \propto r^2$ scaling in (C)

Table 6.3: Summary of scaling laws for high damping

6.4.2 Fundamental principles for developing brain injury criteria

Brain injury is likely caused by exceeding a tissue-level strain tolerance, so the scaling laws between kinematic quantities and the resulting strain presented here can inform the creation of head injury criteria. Using these scaling laws, the amount of kinematic loading that would bring about enough deformation to cause injury can be calculated. For example, if it is known that exceeding a maximum principle strain, ε^{inj}, anywhere within the brain will cause damage, and the dimensionless relaxation time of the brain, the dimensionless pulse duration, and the pulse shape are known, the amount of angular velocity that will lead to injury can be calculated as:

$$|\dot{\theta}|^{inj} = \varepsilon^{inj} \frac{\sqrt{G_u/\rho}}{R_i \tilde{\varepsilon}_{r\theta}^{wcm}(\tilde{t}_0, \tilde{\tau}_R)} \tag{6.6}$$

where the value of $\tilde{\varepsilon}_{r\theta}^{wcm}(\tilde{t}_0, \tilde{\tau}_R)$ is a function of the pulse shape. Using the results in the previous section, the value of $\tilde{\varepsilon}_{r\theta}^{wcm}$ can be ascertained by determining whether the class of impacts has $|\dot{\theta}_f| = 0$. For instance, if the dimensionless relaxation time is between 0.1 and 1, the angular acceleration pulse shape is a sine, and the dimensionless relaxation time is around 0.245, the $\tilde{\varepsilon}_{r\theta}^{wcm}$-value is constant, at a value of 0.5. Therefore, for this whole class of impacts, a simple angular velocity threshold is expected to be enough to predict whether damage will occur. However, if the dimensionless relaxation time of the brain is a factor of ten larger, $\tilde{\tau}_R = 2.45$, the $\tilde{\varepsilon}_{r\theta}^{wcm}$-value is not a constant quantity. Instead, it varies inversely with the square root of the pulse duration. The fractional power of pulse duration in the scaling law relating $\tilde{\varepsilon}_{r\theta}^{wcm}$ to kinematic variables $|\dot{\theta}|_{max}$ and $|\ddot{\theta}|_{max}$ means that neither of these alone is sufficient to predict the $\varepsilon_{r\theta}^{wcm}$. Therefore, it will likewise be impossible to devise an injury criterion that depends on only $|\dot{\theta}|_{max}$ or $|\ddot{\theta}|_{max}$, without also including t_0. Therefore, determining the degree of dissipation performed by the brain material is essential to evaluating both the spatial distribution of strain, and the duration-dependence of proposed injury criteria.

Since the human brain has a relatively small shear modulus, understanding t_{pA}, and the concept of a critical duration more generally, may be useful for understanding why some brain injury criteria are useful in some circumstances and not others. Using approximate properties for the human brain, $G_u = 6$ kPa, $\rho = 1000$ kg/m^3, and R_i, an approximate critical pulse duration for the position $\tilde{r} = 1/4$ can be calculated as $t_{pA}^{brain}(\tilde{r} = 1/4)$ = 8 ms. For the same estimated brain parameters, the critical pulse duration for the exterior of the brain is 41 ms. Therefore, the time-scales of most head injuries could overlap with the time-scale for which the brain switches between strain being proportional with angular velocity or angular velocity divided by a fractional power of pulse duration, and strain being proportional with even higher derivatives of rotation angle, $\theta(t)$. Choosing more compliant properties for the brain will increase estimates of the critical pulse durations. Using $G_u = 2$ kPa produces the result that most head impacts are described by the short-pulse response asymptote, since $t_{pA}^{brain}(\tilde{r} = 1/4)$ would be estimated at around 14 ms.

This brief analysis can be used to put experimental data involving the relative safety of voluntary laboratory head rotations into perspective. Recent work by Hernandez and Camarillo [14] demonstrated that head rotations conducted in laboratory conditions that resulted in relatively high angular velocities were not dangerous, even though they exceeded angular velocity injury thresholds derived from experimental observations from sports collisions, such as BrIC [36]. The key difference between the laboratory impacts and the sports impacts was their durations. In the lab, the head rotations lasted around 40 ms, but the sports impacts were much more rapid. It may be possible that the critical pulse duration of the human brain is less than 40 ms and longer than the duration of the sports collisions used to generate BrIC. If that is the case, then the laboratory impacts were sufficiently long that their severity was not governed by angular velocity. Instead, they may have been in the B-type region or C-type region, where severity is governed by higher derivatives of rotation angle, like angular acceleration.

In conclusion, the scaling laws for a geometrically simple, linear visco-elastic, homogeneous, delicate cylindrical object subject to the rotation of its shell can be used to estimate rotational injury criteria for the brain, if tissue-level strain-based injury criteria are introduced. Even in the absence of reliable tissue-level damage criteria, the scaling laws provided here, when put in terms of approximate brain parameters, can point toward which types of kinematic quantities govern the extent of deformation. This is enough to begin the process of optimizing helmets to diminish the magnitude of these harmful kinematic quantities.

CHAPTER VII

Conclusion

7.1 Contributions

The first subject area developed in this thesis was the design and optimization of a visco-elastic cushion. Then, a simplified model of the human head was used to determine the primary impact characteristics that lead to the highest shear strain and pressure during linear and rotational impacts. The simplified head model used here is composed of a rigid outer shell, that resembles the skull, and a compliant cylinder, which represents the brain. The exterior of the cylinder is attached to the interior surface of the rigid shell. Therefore, when the exterior shell accelerated, the material at the outer radius of the cylinder moves in the same way. The prescribed unidirectional linear acceleration and angular acceleration of the rigid shell is made to take on a few different functional forms in order to determine which aspects of the linear and angular acceleration are most important for predicting the magnitude of the strain within the brain-like cylinder. Using the scaling laws that relate strain to kinematic quantities, it can be seen that the cushion developed in Chapter II is suitable for reducing the strain experienced by the brain during rotational and linear head impacts.

7.1.1 Visco-elastic cushion design and optimization [Chapter II]

- Significant reduction in the velocity change of the delicate object during an impact requires high levels of energy dissipation, which can be achieved with realistic visco-elastic materials modeled with a fractional derivative visco-elastic model.
- Efficient energy dissipation with visco-elastic materials requires that the time-dependence of the impact be known, and the selection of the relation time of the cushion material be matched to the frequency content of the impact.
- In situations where the acceleration of the delicate object must be addressed, using a visco-elastic cushion can reduce the minimum cushion thickness needed to meet the design requirements, with respect to the thickness needed if an elastic material was to be used instead.

7.1.2 Response of compliant visco-elastic cylinders to kinematic loading by linear acceleration pulses [Chapter III]

- When a linear acceleration kinematic load is applied to a cylinder of nearly incompressible material, the pressure is proportional with acceleration.
- Linear acceleration at the levels associated with brain injury in falls and sports collisions generates relatively modest amounts of shear strain. This result is not dependent on the exact constitutive properties assumed for the brain, provided they are within a reasonable range. This is consistent with theories suggesting that linear acceleration does not contribute to brain injuries caused by excessive brain strain.

  What little shear strain is generated by linear acceleration pulses in brain-injury-relevant conditions is proportional with the maximum of the time-derivative of acceleration.

7.1.3 Response of compliant visco-elastic cylinders to kinematic loading by angular acceleration pulses [Chapters IV-VI]

- When the duration of a rotational load is long, a steady-state strain response develops. Transient modes, in addition to this steady state response, are excited by sharp increases in angular acceleration.

- The magnitude of the shear strain wave for short pulses depends on the maximum value of the circumferential speed that the points on the cylinder's outer radius reach. This circumferential speed is proportional with the angular speed of the shell. The strain magnitude of the wave, initially, is one-half the ratio of the circumferential speed of the points on the outer radius of the cylinder to the shear wave speed of the cylinder medium. This fundamental relationship suggests that the angular speed of the skull better suited to estimating the extent of deformation within the brain than the angular acceleration is. This is because there is a fundamental theoretical connection between angular velocity and strain, for short pulses, where no such link exists for the angular acceleration and strain, within this regime.

  The relaxation time of the cylinder medium governs the attenuation of strain pulses as they propagate. The relaxation time, and the ratio of the relaxed shear modulus to the unrelaxed shear modulus, together determine the range of frequencies for which the visco-elastic cylinder medium provides more or less damping. The overlap between the frequency content of the strain pulse and the frequency range that the medium damps drives the extent to which a pulse dissipates.

- A critical value for the duration of the positive region of angular acceleration pulses is denoted with the symbol t_{pA}. Angular acceleration pulses with a positive section that is shorter than this critical value bring about a shear strain response usually characterized by proportionality with the maximum magnitude of the angular velocity of the shell, or characterized by a strain-dependence that is between strict proportionality with angular velocity of the shell and proportionality with the maximum magnitude of the angular acceleration of the shell, in other circumstances. This is a crucial point, and opens up the possibility that brain injury criteria may need to incorporate impact duration into the severity metric directly, since neither angular velocity nor angular acceleration are sufficient on their own to predict deformation levels. (Criteria for differentiating between these two types of pulses are provided in Section 6.1.3.)

t_{pA} is a monotonically decreasing function of the radial coordinate, r, and depends on the unrelaxed shear modulus, density, and radius of the cylinder. Therefor, more compliant objects, like the human brain which has a very low shear modulus, have relatively high values for t_{pA}.

Estimates of $t_{pA}(r)$ for the human brain can be made with approximate values for the shear modulus of the brain and its size. The estimates provided in section 6.4.1 range from 8 ms for interior of the brain, to 41 ms for the exterior, using an approximate unrelaxed shear modulus of 6 kPa and an approximate radius of 10 cm. The stiffness of the brain may be even lower than 6 kPa, which would correlate to even larger t_{pA} values. Most head impacts in football and other contact sports occur over 7 to 15 ms [7], [17], so these estimates suggest that the angular velocity plays a significant role in determining the extent of deformation in the brain during most sport-related collisions.

An extended transition between the short-pulse category of response and the long-pulse category of response occurs for some locations within cylinders subject to pulses which have only smooth variations in their angular acceleration time-dependence shapes. For angular acceleration pulses with durations that fall within this transition region, the shear strain at the points which have the extended transition is proportional with the maximum magnitude of the first time-derivative of angular acceleration.

- The maximum strain throughout a rotating cylinder, called the “whole cylinder maximum” shear strain, can be calculated using the values of the maximum shear strains obtained at every location within the cylinder.

  For pulses shorter than t_A, the whole-cylinder maximum strain will scale with the maximum magnitude of the angular velocity of the shell, if the cylinder is made of a very dissipative medium. If the medium produces very little damping, the whole-cylinder maximum shear strain varies with the quotient of the angular velocity of the cylinder’s shell, and the square root of the duration of the angular acceleration pulse ($\varepsilon_{r\theta}^{wcm} \propto |\dot{\theta}|_{max} {t_0}^{-1/2}$). If the cylinder is moderately damping, very short acceleration pulses have the scaling law $\varepsilon_{r\theta}^{wcm} \propto |\dot{\theta}|_{max} {t_0}^{-1/2}$, and pulses only slightly shorter than t_A have the $\varepsilon_{r\theta}^{wcm} \propto |\dot{\theta}|_{max}$ scaling law.

  For long pulses, the whole cylinder maximum shear strain is the maximum shear strain obtained at the outer radius of the cylinder.

- Efforts to simulate the brain using finite element models should take into account the very fine mesh needed to resolve features of the time-dependent shear strain field that are due to rapid loading, since the speed that strain waves travel at is quite slow, due to the low shear modulus of the brain. Mesh refinement studies that are conducted with the very lowest shear modulus that will be considered, and the most rapidly varying loading signal, are conservative.

In the preceding chapters, a design for a visco-elastic cushion is proposed and the dynamic deformation of an idealized model of the human brain was studied. The analysis of the idealized brain model suggests that the extent of deformation within the brain is primarily governed by the maximum of the magnitude of the angular velocity of the skull, and sometimes the duration of the impact to a lesser degree. This simplification of the dynamic response of the brain applied to the impacts which produce rotation of the skull and last 1 to 40 ms. This correlation of strain with angular velocity, and the coupling between angular motion and linear motion during some head collisions, makes the closed-head brain injury problem a suitable scenario for intervention with the cushion design presented in Chapter II.

7.2 Future Work

7.2.1 Modeling deformation of the brain with a visco-elastic cylinder

In Chapter VI, an alternative scaling law for the strain generated during short impacts was uncovered. Whereas most pulses that bring the shell back to rest after they are complete, and cylinders with high damping, had responses which obeyed the scaling law $\varepsilon_{r\theta} \propto |\dot{\theta}|_{max}$, some situations led to the alternative form $\varepsilon_{r\theta} \propto |\dot{\theta}|_{max} t_0^{-1/2}$. This alternative form applied only to non-dissipative cylinders with shells that were rotated by angular acceleration pulses with final angular speeds larger than 0 rad/s. Future work should consider possible explanations for this departure from the usual scaling behavior. One possible explanation for this phenomenon is a moderate contribution from the mode at the natural frequency of the cylinder. Whereas highly dissipative cylinder materials would damp out this oscillation rapidly, so that it makes a negligible contribution to the shear strain, a weakly dissipating material would not. If it is not damped, then the strain due to this mode could be a significant addition to the strain from the propagating shear strain wave. The contribution of this mode may also be small for the acceleration pulses which have $|\dot{\theta}_f| = 0$, since their spectra are distributed toward higher frequencies than those of the pulses which produce a sustained change in angular velocity. Since the natural frequency of the cylinder is relatively low, the half sine and single rectangular pulse spectra excite that mode more than the sine and bipolar rectangular pulse spectra do.

The scaling laws developed for strain in linear and rotational impacts can also serve as reference for determining the effects of increasing the complexity of the constitutive laws used in other finite element models of the brain. Since the use of more elaborate constitutive models require more computational resources, their use should be considered in the context of what greater accuracy they permit. Similarly, being able to quantify the increase in accuracy from using different constitutive laws for different regions of the brain, relative to assuming homogeneity, will enable researchers to direct their attention toward the properties and parameters that improve accuracy the most. For example, dividing the cylinder into an external annulus and an internal cylinder, each with different material properties, could be used to develop a preliminary understanding of the affect of interior regions of the brain being either more rigid or more compliant than exterior regions.

7.2.2 Validating the performance of visco-elastic cushions for protecting the human brain during impact

The next step in implementing the cushion in Chapter II is a series of parametric studies involving the simultaneous simulation of the strain that evolves in the delicate object and the deformation of the cushion during impacts with both linear and angular motion. Completing this work requires expressing the fractional derivative visco-elastic material definition in a finite element package [1], and addressing the numerical challenges associated with dynamic two-dimensional contact involving the rigid surface of the shell and the compliant visco-elastic cushion. This is an ongoing project, and interpreting the results of these simulations is grounded in the fundamental mechanics of both the cushion and the compliant delicate objects described in this thesis.

BIBLIOGRAPHY

BIBLIOGRAPHY

[1] G. Alotta, O. Barrera, A. Cock, and M.D. Paola. The finite element implementation of 3D fractional viscoelastic constitutive models. 146:28–41, 2018.

[2] M.F. Ashby and D. Cebon. Materials selection in mechanical design. *Le Journal de Physique IV*, 3(C7):C7–1, 1993.

[3] T.M. Atanackovic and D.T. Spasic. On viscoelastic compliant contact-impact models. 71:134–138, 2004.

[4] P. Bayly. Brain motion under impact. *Physics*, 11:32, 2018.

[5] P.V. Bayly, P.G. Massouros, E. Christoforou, A. Sabet, and G.M. Genin. Magnetic resonance measurement of transient shear wave propagation in a viscoelastic gel cylinder. *Journal of the Mechanics and Physics of Solids*, 56(5):2036–2049, 2008.

[6] L.E. Bilston. Brain tissue mechanical properties. pages 69–89. Springer, 2011.

[7] Steven P Broglio, Brock Schnebel, Jacob J Sosnoff, Sunghoon Shin, Xingdong Feng, Xuming He, and Jerrad Zimmerman. The biomechanical properties of concussions in high school football. *Medicine and science in sports and exercise*, 42(11):2064, 2010.

[8] J.M. Carcionne. *Wave fields in real media: Wave propagation in anisotropic, anelastic, porous and electromagnetic media*. Elsevier, 3 edition, 2015.

[9] Lee F Gabler, Jeff R Crandall, and Matthew B Panzer. Development of a second-order system for rapid estimation of maximum brain strain. *Annals of biomedical engineering*, 47(9):1971–1981, 2019.

[10] L.F. Gabler, J.R. Crandall, and M.B. Panzer. Assessment of kinematic brain injury metrics for predicting strain responses in diverse automatic impact conditions. 44:3705–3718, 2016.

[11] L.F. Gabler, H. Joodaki, J.R. Crandall, and M.B. Panzer. Development of a single-degree-of-freedom mechanical model for predicting strain-based brain injury responses. *Journal of biomechanical engineering*, 140(3), 2018.

[12] J Sebastian Giudice, Wei Zeng, Taotao Wu, Ahmed Alshareef, Daniel F Shedd, and Matthew B Panzer. An analytical review of the numerical methods used for finite element modeling of traumatic brain injury. *Annals of biomedical engineering*, 47(9):1855–1872, 2019.

[13] D. Goodwin and D. Young. *Protective Packaging for Distribution: Design and Development*. DEStech Publications, Inc., 2010.

[14] Fidel Hernandez and David B Camarillo. Voluntary head rotational velocity and implications for brain injury risk metrics. *Journal of neurotrauma*, 36(7):1125–1135, 2019.

[15] J. Hetherington and P. Smith. *Blast and ballistic loading of structure*. Taylor and Francis Group, 1 edition, 1994.

[16] A.H.S Holbourn. Mechanics of head injuries. 242:438–441, 1943.

[17] T.B. Hoshizaki, A. Post, M. Kendall, J. Cournoyer, P. Rousseau, M. Gilchrist, S. Brien, M. Cusimano, and S. Marshall. The development of a threshold curve for the understanding of concussion in sport. 19:196–206, 2016.

[18] W. Johnson and A.G. Mamalis. Crashworthiness of vehicles. Technical report, 1978.

[19] Hideyuki Kimpara and Masami Iwamoto. Mild traumatic brain injury predictors based on angular accelerations during impacts. *Annals of biomedical engineering*, 40(1):114–126, 2012.

[20] S. Kleiven and W.N. Hardy. Correlation of an fe model of the human head with local brain motion-consequences for injury prediction. Technical report, SAE Technical Paper, 2002.

[21] Svein Kleiven. Evaluation of head injury criteria using a finite element model validated against experiments on localized brain motion, intracerebral acceleration, and intracranial pressure. *International Journal of Crashworthiness*, 11(1):65–79, 2006.

[22] Svein Kleiven. Predictors for traumatic brain injuries evaluated through accident reconstructions. Technical report, SAE Technical Paper, 2007.

[23] M. Kornhauser and R.W. Lawton. Impact tolerance of mammals. 7:386–394, 1961.

[24] Kaveh Laksari, Lyndia C Wu, Mehmet Kurt, Calvin Kuo, and David C Camarillo. Resonance of human brain under head acceleration. *Journal of The Royal Society Interface*, 12(108):20150331, 2015.

[25] S.S. Margulies and L.E. Thibault. An analytical model of traumatic diffuse brain injury. 1989.

[26] S.S Margulies and L.E. Thibault. A proposed tolerance criterion for diffuse axonal injury in man. *Journal of biomechanics*, 25(8):917–923, 1992.

[27] P.G. Massouros, P.V. Bayly, and G.M. Genin. Strain localization in an oscillating maxwell viscoelastic cylinder. *International journal of solids and structures*, 51(2):305–313, 2014.

[28] David F Meaney and Douglas H Smith. Biomechanics of concussion. *Clinics in sports medicine*, 30(1):19–31, 2011.

[29] B. Morrison, H.L. Cater, C. C-B. Wang, F.C. Thomas, C.T. Hung, G.A. Ateshian, and L.A. Sundstrom. A tissue level tolerance criterion for living brain developed with an in vitro model of traumatic mechanical loading *Stapp Car Crash.* 47:385, 2003.

[30] A.K. Ommaya and A.E. Hirsch. Tolerances for cerebral concussion from head impact and whiplash in primates. *Journal of biomechanics*, 4(1):13–21, 1971.

[31] Ayub K Ommaya, Lawrence Thibault, and Faris A Bandak. Mechanisms of impact head injury. *International Journal of Impact Engineering*, 15(4):535–560, 1994.

[32] Andrew Post and T Blaine Hoshizaki. Rotational acceleration, brain tissue strain, and the relationship to concussion. *Journal of biomechanical engineering*, 137(3), 2015.

[33] Michael T Prange and Susan S Margulies. Regional, directional, and age-dependent properties of the brain undergoing large deformation. *J. Biomech. Eng.*, 124(2):244–252, 2002.

[34] T. Pritz. Analysis of four-parameter fractional derivative model of real solid materials. 195:103–115, 1996.

[35] T. Rahimzadeh, E.M. Arruda, and M.D. Thouless. Design of armor for protection against blast and impact. 85:98–111, 2015.

[36] Erik G Takhounts, Matthew J Craig, Kevin Moorhouse, Joe McFadden, and Vikas Hasija. Development of brain injury criteria (bric). Technical report, SAE Technical Paper, 2013.

[37] Erik G Takhounts, Jeff R Crandall, and Kurosh Darvish. On the importance of nonlinearity of brain tissue under large deformations. Technical report, SAE Technical Paper, 2003.

[38] FJ Unterharnscheidt. Translational versus rotational acceleration-animal experiments with measured input. Technical report, SAE Technical Paper, 1971.

[39] J. Versace. A review of the severity index. Technical report, SAE Technical Paper, 1971.

[40] F. Wang, Y. Han, B. Wang, Q. Peng, X. Huang, K. Miller, and A. Wittek. Prediction of brain deformations and risk of traumatic brain injury due to closed-head impact: quantitative analysis of the effects of boundary conditions and brain tissue constitutive model. 17:1165–85, 2018.

[41] A.S Wineman and K. R. Rajagopal. *Mechanical response of polymers: an introduction*. Cambridge university press, 2000.

[42] Rika M Wright and KT Ramesh. An axonal strain injury criterion for traumatic brain injury. *Biomechanics and modeling in mechanobiology*, 11(1-2):245–260, 2012.

[43] King H Yang, Jingwen Hu, Nicholas A White, Albert I King, Clifford C Chou, and Priya Prasad. Development of numerical models for injury biomechanics research: a review of 50 years of publications in the stapp car crash conference. Technical report, SAE Technical Paper, 2006.

[44] Wei Zhao, Bryan Choate, and Songbai Ji. Material properties of the brain in injury-relevant conditions–experiments and computational modeling. *Journal of the mechanical behavior of biomedical materials*, 80:222–234, 2018.

[45] Z. Zhao, X. Li, S. Kleiven, C.S. Shah, and W.N. Hardy. A reanalysis of experimental brain strain data: implication for finite element head model validation. 62:293–318, 2018.